Simulation of Magnetic and Electronic Properties of Nanostructures

Zur Erlangung des akademischen Grades eines

DOKTORS DER NATURWISSENSCHAFTEN

von der Fakultät für Physik des
Karlsruher Instituts für Technologie (KIT)

genehmigte

DISSERTATION

von

Dipl.-Phys. Igor Beljakov
aus Charkow

Tag der mündlichen Prüfung: 09.01.2015
Referent: Prof. Dr. Wolfgang Wenzel
Korreferent: Prof. Dr. Gerd Schön

Contents

Publication List

[1] Beljakov, Igor; Meded, Velimir; Symalla, Franz; Fink, Karin; Shallcross, Sam; Wenzel, Wolfgang. "Magnetic Anisotropy of Graphene Quantum Dots Decorated with a Ruthenium Adatom"; *Beilstein J. Nanotechnol.*, 2013, **4**, 441–445

[2] Gutrath, Benjamin S.; Oppel, Iris M.; Presly, Oliver; Beljakov, Igor; Meded, Velimir; Wenzel, Wolfgang; Simon, Ulrich. "[Au14(PPh3)8(NO3)4]: An Example of a New Class of Au(NO3)-Ligated Superatom Complexes"; *Angew. Chem. Int. Ed.*, 2013, **52**, 12, 3529–3532

[3] Beljakov, Igor; Meded, Velimir; Symalla, Franz; Fink, Karin; Shallcross, Sam; Ruben, Mario; Wenzel, Wolfgang. "Spin-Crossover and Massive Anisotropy Switching of 5d Transition Metal Atoms on Graphene Nanoflakes"; *Nano Lett.*, 2014, **14**, 6, 3364–3368.

[4] Symalla, Franz; Meded, Velimir; Beljakov, Igor; Fink, Karin; Shallcross, Sam; Wenzel, Wolfgang. "Band Gap Engineering with a Twist: Formation of Intercalant Super-lattices in Twisted Graphene Bilayers"; submitted to *Phys. Rev. Lett.*

[5] Gutrath, Benjamin S.; Schiefer, Frank; Englert, Ulli; Şerb, Mihaela-Diana; Bettray, Wolfgang; Beljakov, Igor; Speiser, Berndand; Meded, Velimir; Wenzel, Wolfgang; Simon, Ulrich. "Crystal Structure and Electronic Properties of [Au8(PPh3)8](NO3)2"; preprint.

1 Overview and Outline

Miniaturization of information storage devices has been an ongoing technological development and challenge during the past half-century. Only during the last 10 years the memory storage density of the SD-cards increased by three orders of magnitude. To keep up with this trend, sustainable technological advances are needed, to ultimately allow storage of a single bit of information on a single molecule or on a single atom.

The discovery of molecular complexes demonstrating magnetic anisotropy [6] opened opportunities for research in this direction. A number of single-molecule magnets (*SMM*), typically containing multiple magnetic atoms, were reported [7–13]. In the last five years there have also been an increasing number of reports on SMMs containing only one magnetic atom, so called single-ion magnets (*SIM*) [14–20]. The researchers in this field struggle with the short lifetime of the magnetization state, which currently reaches only few seconds at temperatures above 3K [6]. One possible solution to this problem are magnetic centers with a high magnetic anisotropy, i.e. atoms with high spin-orbit coupling. While most of the SMMs and SIMs utilize 3d transition metals (*TM*s) and rare earths, 4d and 5d transition metals are rarely reported in SMM. To the best of our knowledge, no SIMs were reported with 5d transition metals so far, which is caused by difficulties to synthesize the 4d and 5d compounds [21] or quenching of the magnetic moment of 5d TMs by the ligand field [22].

Another approach to single molecule information storage are molecular switches which utilize the spin-crossover effect (SCO), i.e. change of the spin multiplicity by external means. As the effect is magneto-mechanical, the two distinct spin states of *SCO molecules* are strongly decoupled, and therefore much more stable than the states of SMMs. The major limitation of the application of SCO molecules as molecular storage devices is the state read-out, which requires low temperature methods.

In the work presented in this thesis I combine the advantages of the SIMs and the SCO molecules, in order to circumvent their limitations, by introducing a SCO molecule with a single 5d TM magnetic center and a graphene nanoflake as the ligand. There is a large number of publications describing graphene as an appropriate substrate for transition metals [23–31], on which they exhibit a large magnetic anisotropy [23, 24, 27, 29] and even a structural bistability [31].

In this thesis I apply density functional (DFT) methods [32] to show that 5d TMs not only exhibit bistability and spin crossover on the graphene flakes, but also a huge magnetic anisotropy, which changes the preferred magnetic direction upon the spin crossover, allowing an easy read-out of the magnetic state. Finally, I show that the switching can be controlled by an external electric field. Combination of these data suggests that the graphene nanoflakes, which have already been synthesized [33], decorated by transition metals may be the first viable option for single atom magnetic storage at room temperature.

Overall, I investigate three topics in this thesis, related to the electronic and magnetic structure of nanoscale systems: the first is the investigation of the graphene/transition metal single molecule switches, which constitutes the main line of research in this thesis.

In the second topic I apply DFT methods to characterize ultrasmall gold nanoparticles (*usAuNP*). Ultrasmall gold nanoparticles have a significant application potential in a number of areas: in medicine [34], biomedical imaging [35–38], catalysis [39–43], cancer therapy and diagnosis [36, 44, 45], sensors [46], and photonic devices [47]. High stability of usAuNP makes them particularly attractive for technological purposes. However not every ultrasmall AuNP exhibits a high stability. There are a number of concepts, in part in agreement with experiment, which predict the number of gold atoms that results in extraordinary stable usAuNP. These models are based on concepts of nanocrystal [48, 49] and superatom complexes [50, 51]. However, as many factors, including ligand composition, are relevant to the stability of the gold nanoclusters, synthesis of novel clusters and their characterization remains a very active field [34, 39, 43, 52, 53]. It is particularly interesting when novel clusters are found to defy previous established rules.

In this thesis I investigate a recently synthesized $[Au_{14}(PPh_3)_8](NO_3)_4$ nanoparticle, which does not fulfill any of the stability criteria, while it is observed to be experimentally stable at ambient conditions [2]. This structure does fulfill the superatom criterion, which postulates that four of the 14 gold atoms must be counted to the electron-withdrawing ligands, if the HOMO and LUMO have a two-dimensional shape. We utilize DFT to calculate the frontier orbitals and other properties of the cluster to show that it can be decomposed into subsystems which make the superatom model applicable and explain its stability.

Since in a number of applications the relevant optical properties of gold nanoparticles depend on the HOMO-LUMO gap, its prediction plays an important role in the development of novel stable gold nanoparticles and clusters. Applying DFT methods on a series of usAuNPs we calculate their band gaps, and compare them with the experimental results in order to elucidate trends in the HOMO-LUMO gap as a function of particle size.

The third part of this thesis is dedicated to method development to solve the Boltzmann transport equation for electron transport in mesoscopic two-dimensional nanodevices, utilizing the ensemble Monte Carlo technique [54]. Computer simulations are widely used as an aid to characterize the properties of electronic circuits, e.g. with the software package SPICE [55]. All of the essential electronic parameters of the relevant electronic components are stored in so-called compact models and used to simulate the behavior of a complete circuit or device. The component-specific compact models are usually parametrized from the experiment. However, for novel components, such as graphene-based transistors on various substrates, microscopic models, which can predict the IV and VC characteristics would be of great use. These models could reduce the development effort for many experimental academic groups as the task to produce a sufficiently large number of samples to satisfactory parameterize the corresponding compact models based only on the experimental data remains a formidable challenge.

Electronic transport in bulk materials can be described using the semiclassical Boltzmann transport equation, *BTE* [56]. To solve the underlying equations we choose the ensemble Monte Carlo technique [54], because it allows for simple implementation of the scattering mechanisms and provides an easy connection with the underlying physics, which is practical at the development stage. The novelty of our approach is the flexibility and an extended applicability of the method. We have implemented our code in the framework of ELMER software package [57], which allows us to utilize its control file principle, giving a possibility to change the material properties and the device shape without a massive implementation effort in the underlying code.

Thesis Outline

The thesis is structured as follows, taking the three topics into account.

Graphene-based Single Molecule Magnetic Switches

Chapter 2: Introduction into single molecule magnets (*SMM*s) and spin crossover (*SCO*) molecules, material properties of graphene, a literature overview of graphene as a substrate for transition metal atoms, and an introduction of triangular graphene nanoflakes.

Chapter 3: Density functional theory.

Chapter 4: Magnetic properties of pure flakes; binding energies and magnetic anisotropy of ruthenium on graphene nanoflakes for different flakes edges, sizes and adsorption sites.

Chapter 5: Binding energies and magnetic anisotropy of 5d transition metal adatoms on armchair graphene nanoflakes for different flake sizes and adsorption sites. Report of the structural bistability, spin-crossover effect, magnetic anisotropy switching, and the influence of external electric field on this structures. Proof of the results against intrinsic computational details.

Ultrasmall Gold Nanoparticles

Chapter 6: Density functional analysis of ultrasmall gold nanoparticles.

Electronic Transport in Nanodevices

Chapter 7: Introduction in the Boltzmann transport equation and the Ensemble Monte Carlo technique. Detailed description of the principles of our simulation of the electronic transport in nanostructures. Comparison of simulated properties with previously reported values.

Summary and Outlook

Chapter 8: Summary and Outlook

2 Graphene Nanoflakes as Alternative Ligands for Atomic Memory Device

2.1 Single Molecule and Single Ion Magnets

One approach to build a single-molecule device capable to store one bit of information are single molecule magnets (*SMM*s). They are metal-organic compounds containing a transition metal or rare earth core, surrounded by an organic ligand hull. An SMM can be magnetized in an external magnetic field and it will keep the magnetization for at least several hours at sufficiently low temperatures [58]. A wide range of SMMs was found since the first report in 1993 [6]. While most SMMs discovered to date contain more than one magnetic atom in the core, recently SMMs were reported which contain only one magnetic center [20]. A bit of information can be stored in an SMM similarly to the conventional magnetic storage devices: as a magnetization direction (i.e. spin up or spin down) along a magnetization axis. The information read-out in an SMM is accomplished by standard magneto-optical reading techniques [59].

In SMMs with multiple magnetic cores, the two magnetic states with the opposite magnetization result from the ferromagnetic coupling between the magnetic moments of the single atoms, which can be described in the first order by the Heisenberg model:

$$E_H = \sum_{i,j} -I m_i m_j \tag{2.1}$$

Here I is the interaction prefactor, positive (negative) for ferromagnetic (antiferromagnetic) coupling, and m_i is the projection of the spin magnetic moment of the atom i on the preferred magnetization axis. In the ferromagnetic case the energy is minimized when the magnetic moments of all atoms are aligned in one direction. The state where one or more spins are aligned against the majority is therefore higher in energy and has a reduced lifetime. Since temperature-induced spin-flips are unlikely to occur simultaneously on multiple atoms, the probability for a system to flip the total magnetization is sufficiently low for high I. In order to prevent a collective rotation of the magnetization axis and, therefore, the spontaneous switching, a functional SMM requires high magnetic anisotropy, i.e. a strong preference of one magnetization direction. The ligand field and/or the constellation the neighboring atoms perturbs certain atomic orbitals of the magnetic atom, which leads to quenching of the orbital magnetic moment in the direction perpendicular to these orbitals. The spin-orbit coupling aligns the otherwise isotropic spin moment to the spatial direction along which the orbital magnetic moment is maximum, resulting in a magnetic anisotropy. High magnetic anisotropy leads to higher barriers between the two magnetic ground states, and therefore to longer magnetic relaxation times.

In a mononuclear SMM, also referred to as a monometallic SMM or as a single ion magnet

(*SIM*), the splitting of the energy levels for different spin states is induced purely by the ligand field. The major problem of SIMs is the quantum-mechanical mixing of different magnetic states [60]. It was shown [20] that under certain symmetry conditions the two ground states with the opposite magnetic moments do not mix, but the lifetimes of these states still reduce the applicability of SIMs to cryogenic temperatures [20].

2.2 Spin-Crossover Molecules

Another approach to use a single magnetic atom as a single bit storage are spin-crossover (SCO) molecules. The spin-crossover effect takes place when the spin multiplicity of a molecule changes under external influence. SCO was initially investigated as a bulk effect, where e.g. pressure and/or temperature addresses the magnetic state. Recently, SCO effects were also reported for single molecules [61], in which the magnetic state can be addressed by e.g. external electric field or laser pulses [62].

The molecular magnetic state changes between the low-spin (LS) state, i.e. low number or zero unpaired electrons, and the high-spin (HS) state, i.e. at least two more unpaired electrons than in the LS state. Therefore, the length of the magnetic moment can be utilized to store one bit of information. The advantage of this storage method is that the direction of the magnetic moment does not play a role, in contrast to the SMM. A single magnetic center is therefore enough to set up a functional SCO molecule. Apart from this, the SCO effect is a magneto-mechanical effect, i.e. the distance between the ligand and the magnetic center changes upon the transition. Such structural change mechanically decouples the two states, making them thermally stable, a great technical advantage over the SMMs and SIMs.

A major drawback of SCO molecular switches is the read-out procedure, since the LS and HS state are difficult to distinguish experimentally. Utilizing the mechanical character of the effect requires a high spacial resolution: a typical change in the interatomic distance is only about 0.3 Å [63]. Conductance measurements can also distinguish the states, but again only at low temperatures [61].

2.3 Combining a Single Ion Magnet with a Spin-Crossover Molecule

Even through the mechanism of information storage is quite different, SIMs and SCO molecules share a number of common advantages and limitations. They are chemically synthesized [64, 65], which allows in principle large scale production with perfect reproducibility; they have a high molecular symmetry, allowing the analysis and tuning of their properties. Unfortunately, they are restricted to 3d transition metals (TMs) and rare earths, as the magnetic moment of larger 4d and 5d TMs is known to be quenched by the ligand field [22].

Major differences between SIMs and SCO molecules lie in the stability of the states, and the feasibility of the magnetic state read-out. While the states of a single ion magnet can be read-out

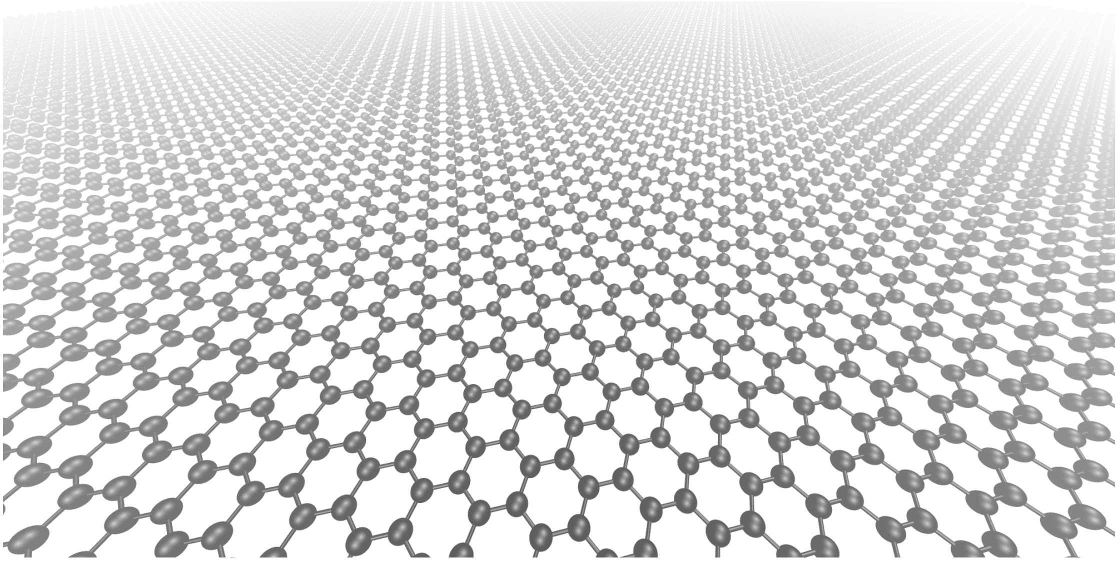

Figure 2.1: *Atomic structure of graphene. Carbon atoms are arranged in a honeycomb lattice.*

relatively easily, they are highly instable at higher temperatures. The states of SCO molecules, on the other hand, are thermally stable, but their read-out is only feasible at low temperatures.

To circumvent these limitations, we suggest that a single ion magnet, which would also switch its magnetization direction upon spin crossover, could combine the stability of SCO molecules with a read-out feasibility of SIMs. To avoid any further misunderstanding, we point out that by the magnetization direction switching we do not mean the flip from spin "up" to spin "down", but rather a rotation of the preferable magnetic axis by a certain easy measurable angle.

An important property of such kind of spin crossover single ion magnet would be a high magnetic anisotropy energy, *MAE*, which stabilizes the preferred magnetization axis against thermal fluctuations. While MAE is generally defined as the energy dependence of the magnetic moment as a function of its direction, here we use the term for the energy difference between the most and the least energetically preferable magnetization direction. Apart from the ligand field, the strength of the single atom magnetic anisotropy depends on its spin-orbit coupling, which grows with the atomic number, making 4d and 5d transition metals good candidates to start the investigation. Since the conventional organic ligands quench the magnetic moment of 4d and 5d TM atoms [22], finding an alternative, less interacting ligand was crucial for the project at hand. Here we focus on graphene and its spatially limited derivatives.

2.4 Graphene: a True Two-Dimensional Material

Graphene is a single-atom thick material comprised of carbon atoms, which are arranged in a honeycomb lattice (see Figure 2.1). Each carbon atom is connected to three other carbon atoms with σ-bonds formed of sp^2-hybridized atomic orbitals, with the fourth valence electron contributing to the delocalized π-cloud, making it possible for considerable electric current to flow in such a system. Basically, well-known graphite, which is used in pencils, is a vast bulk of graphene sheets stacked upon each other in alternating ABAB sequence and held together by van der Waals forces.

Due to its two-dimensional structure, a number of physical properties of graphene are superior compared to conventional materials, in particular high intrinsic carrier mobility, thermal conductivity and mechanical stability [66]. Combined with a light transmittance of 97.5% in the infrared to visible range [67], graphene seems to be *the* candidate for transparent electronic circuits, such as touch screens used nowadays in almost every portable electronic device.

We will first introduce a classification of carbon-based structures. Since the terminology of graphene-based materials is not unique, I will use the terms as they are suggested in the editorial letter of the journal *Carbon* in October 2013 [68]. The natural three-dimensional arrangements of pure carbon are diamond and graphite. The first is perfectly insulating because each of the sp^3 hybridized carbon atoms is connected to four other carbon atoms, leaving no free electrons available for electric current. The latter, the graphite, consists of carbon sheets, in which sp^2 hybridized carbon atoms are connected via σ-bonds in xy-plane, having three nearest neighbors each. The sheets are held together in z-direction by van der Waals forces. Graphite is more common in nature as it is the energetically most preferable arrangement of carbon. Special, but not fully exclusive to carbon is that it also exists as a stable two-dimensional solid. According to the editorial letter mentioned above, each carbon sheet in the graphite structure, can be called *graphene layer*, a term used since the 1980s. If we dissolve the van der Waals interaction holding graphite together and isolate the topmost graphene layer, it would be called just *graphene*, or *suspended graphene*. Since nowadays people use the term *graphene* also for few-atoms thick carbon layers (actually *multilayer graphene*), a more precise term for one-atom thick sp^2 carbon planes would be *single-layer graphene*. Further in this thesis, "graphene" is used for "single-layer graphene", as suggested in [68]. Single-layer graphene, restricted in one direction, is called *graphene (nano-) ribbon*. The prefix *nano* is used for graphene ribbons which have the width of less than 100 nm. A graphene (nano-)ribbon can also be rolled into a tube, and constitute a *carbon nanotube* (CNT). Carbon nanotubes can be *single-layer* or *multi-layer*, but they exceed the scope of this thesis. An island of graphene is called *graphene sheet*. It can be called *graphene nanosheet*, if its radius is smaller than 100 nm, or *graphene quantum dot*, if it is smaller than 10 nm. In this thesis we will use the term *single-layer graphene nanoflake*, *graphene nanoflake*, or just *flake*, by analogy with the term *graphite nanoflakes* suggested for multilayer-graphene islands less than 100 nm.

2.4.1 Atomic Structure

The graphene crystal lattice is spanned by two unit vectors: $\frac{a}{2}\binom{\sqrt{3}}{1}$ and $\frac{a}{2}\binom{\sqrt{3}}{-1}$ with the lattice constant $a = 2.46\,\text{Å}$. The elemental cell contains two atoms, which sit at positions $\binom{0}{0}$ and $a\binom{1/\sqrt{3}}{0}$. The nearest neighbor distance is therefore $\frac{a}{\sqrt{3}} = 1.42\,\text{Å}$. Carbon atoms in graphene are sp^2-hybridized. The three sp^2 orbitals lie in plane and form an angle of 120^o, while the $2p_z$ orbital is perpendicular to that plane. The overlapping sp^2 orbitals of the neighboring atoms form bonding σ-bonds, while the $2p_z$ orbitals build a π-bond, which has weaker binding energy than the σ-bonds. The π-bonds form energy bands, which can be described using for example the tight-binding model.

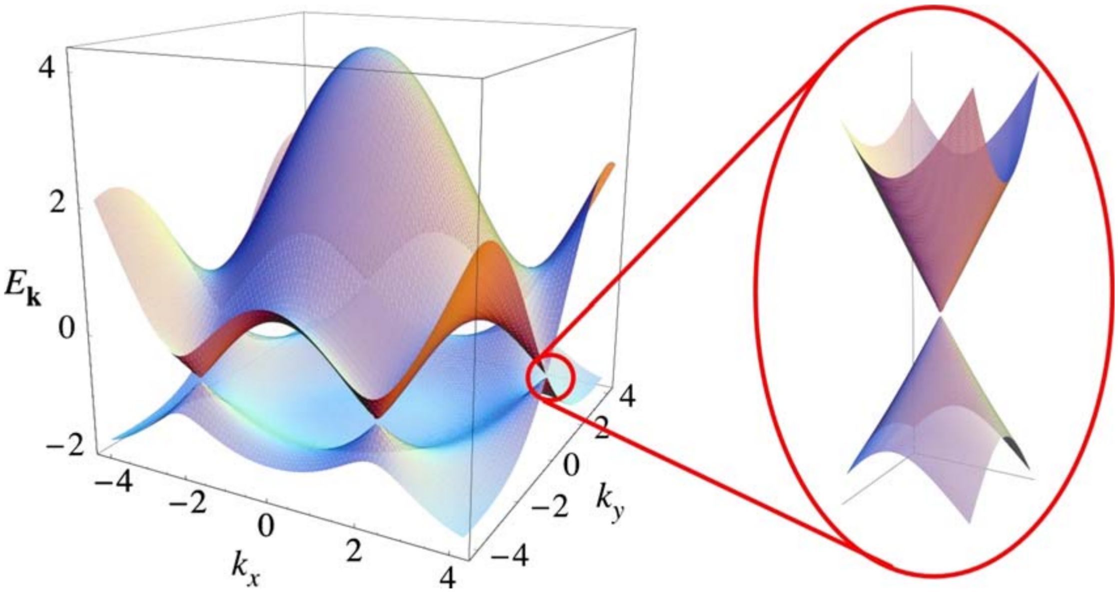

Figure 2.2: *Band structure of graphene. The conduction band (upper surface) and the valence band (lower surface) meet at six K-points arranged hexagonally. The dispersion relation is linear in proximity of the K-points (inset). Taken from [69].*

2.4.2 Electronic Properties

Graphene belongs to the so-called semi-metals: although it has no electronic band gap, the density of states at the Fermi level is zero. The bottom of the conduction band is not at the Γ-point, as in most semiconductors, but at the K-points (see Figure 2.2). There are six K-points in the first Brillouin zone, which, due to the hexagonal symmetry, can be subdivided into two groups, K and K'. The dispersion relation at the K-points is linear, which is quite unique for graphene. The Hamiltonians H_0^K and $H_0^{K'}$ for the electrons in the vicinity of K and K' respectively can be described by the following equations:

$$\begin{aligned} H_0^K &= v_F\, \boldsymbol{\sigma} \cdot \mathbf{p} \\ H_0^{K'} &= v_F\, \boldsymbol{\sigma}' \cdot \mathbf{p} \end{aligned} \tag{2.2}$$

where $\mathbf{p}$ is the two-dimensional momentum vector, $\boldsymbol{\sigma}$ and $\boldsymbol{\sigma}'$ equal to (σ_x, σ_y) and $(-\sigma_x, \sigma_y)$ respectively, with the Pauli matrices σ_x and σ_y, and v_F is the prefactor called Fermi velocity. The equation for H_0^K is the Dirac-Weyl equation, which is a special case of the Dirac equation for massless particles and therefore usually used to describe e.g. neutrinos. The energy eigenvalues of the resulting matrices are

$$E = \pm \hbar v_F |\mathbf{k}| \tag{2.3}$$

with the wavenumber $\mathbf{k} = \frac{\mathbf{p}}{\hbar}$ and the Planck's constant $\hbar$ The positive and negative energies are the solutions for electrons and holes respectively. The i-th component of the electron group velocity is defined as

$$(\mathbf{v_g})_i = \frac{\partial E(\mathbf{k})}{\hbar \partial k_i} \tag{2.4}$$

which is equal to v_F in the vicinity of the Fermi level, allowing the electrons to move with the constant group velocity of $v_F \approx c/300$. This is one of the reasons for the high mobility and thermal conductivity of graphene. Another consequence of the linear dispersion is a strong response of carrier density to applied gate voltage. These properties theoretically allow graphene-based electronic devices to work at THz frequencies and make it a very attractive material candidate for the communication and computing devices. Since graphene is a quite stable membrane with a free electron gas, it can easily be used for further functionalizations.

2.5 Graphene as a Substrate

The idea of using graphene as an adsorbent for magnetic atoms was motivated by works of Xiao et al. in which they showed theoretically, that Co [23] and Fe, Ni, Ru, Rh, Pd [24] dimers on benzene exhibit high magnetic anisotropy, and expect similar behavior on graphene substrate. Since then a lot of research was done on transition metal (*TM*) atoms on graphene. For example, Mao et al. used density functional theory to calculate adsorption of Mn, Fe and Co on graphene. They demonstrated modification of graphene electronic structure by the adatoms [25]. It was shown that the hollow site (over the middle of a carbon hexagon in honeycomb lattice) is the most stable position for these three elements. Cao et al. presented a theoretical work on Fe, Co, Ni and Cu atoms and dimers on graphene and showed that an effective modulation of graphene properties can be achieved by transition metal adsorption [26]. Sargolzaei theoretically investigated the binding energies and the magnetic anisotropy of 3d transition metal (from Sc to Ni) adatoms on graphene and benzene [27]. Zolyomi et al. provided a broad theoretical study of adsorption energies of 4d and 5d series transition metals on graphene [28], showing that "the elements with low or near-half occupation of the d-shell bind strongest" to graphene. Zhang et al. predicted tunable magnetic anisotropy of 5d transition metal adatoms on graphene, which varies in the range of several meVs [29]. Blonski et al. theoretically investigated platinum single atoms and dimers on graphene deposited on Ni(111) surface, showing an anisotropy of the dimers [30].

Alongside with reports of strong magnetic anisotropy and good adsorption properties, the crucial point which makes graphene an outstanding candidate for a single molecule SCO magnet is the spin-crossover of Co atoms on graphene reported in a theoretical work by Virgus et al. [31]. It indicates a possibility of a similar behavior for 4d and 5d transition metals.

Positioning a large number of magnetic adatoms on graphene sheet in order to build a molecular storage device potentially can lead to a number of unwanted effects. First, shared substrate and regular distribution can modify the electronic state of the adatoms and lead to coupling between their magnetic moments destroying the stored information. Second, the magneto-mechanical character of SCO may exhibit less stable states and lead to moving of the adatoms along the surface and finally to their clustering. Third, the adatoms show a strong affinity toward graphene defects, as was shown both experimentally and theoretically by Cretu et al. [70], which can lead to both modification of the electronic properties and clustering of the adatoms. At the same time, graphene edge is an inevitable part of a real graphene sheet and, considering the edge as an ultimate defect, can also attract the adatoms.

To avoid these complications, we consider utilizing graphene nanoflakes rather than infinite

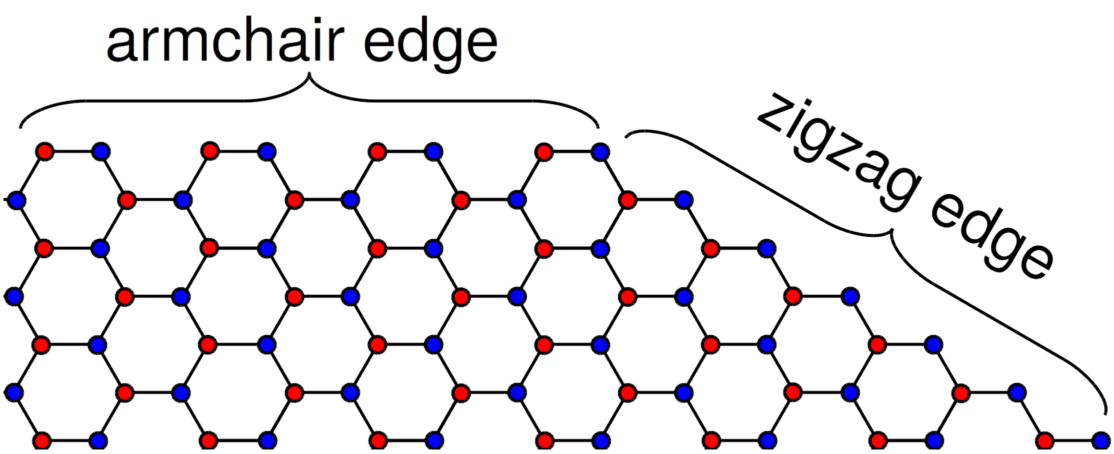

Figure 2.3: *The structure of two regular types of graphene edge. Red and blue dots represent carbon atoms in two sublattices. In the case of armchair edge carbon atoms of both sublattices are present at the very edge. In the zigzag case carbon atoms of only one sublattice are terminating the sheet, which leads to a breaking of the sublattice symmetry.*

graphene. As reported by Treier et al. [33] graphene flakes of controllable size can be produced in large amounts using bottom up techniques. Usage of nanoflakes can 1) decouple the magnetic centers, 2) prevent the clustering and 3) introduce the "defect" per construction, forbidding further modification of the electronic state of the adatoms. Since the aim of this work is a novel kind of SCO *molecules*, the fact that graphene nanoflakes constructed of less than hundred carbon atoms are basically large conjugated molecules and can act like a ligand hull makes them much more attractive candidates than infinite graphene.

2.6 Triangular Graphene Nanoflakes

Considering that the majority of studies on magnetic properties of TM adsorbed onto graphene neglect the edge, a study of TMs on graphene nanoflakes is even more promising, as it provides an opportunity to investigate the influence of graphene edge on properties of the adatoms. There are two regular edge types graphene lattice can have: *armchair* and *zigzag* (see Figure 2.3). The simplest geometrical shape maintaining one edge type on all sides of a graphene flake is the triangular shape. Graphene nanoflakes of this shape are used throughout the study. We vary the flake size as the parameter that effectively tunes the dimensionality of the system from zero (benzene) to two dimensions (graphene) [3].

The structures of the flakes investigated in this work are shown in Figure 2.4. They are labeled by the number of carbon atoms: the flakes with armchair edges are C18 (triphenylene), C36 (tribenzo[fgh,pqr,za$_1$b$_1$]trinaphthylene) and C90, and the flakes with zigzag edges are C33 and C97. The labels are not to be confused with the chemical structure formula, since the flakes also contain hydrogen to saturate the carbon atoms at the edges. The complete chemical formulas are: $C_{18}H_{12}$, $C_{36}H_{18}$, $C_{90}H_{30}$, $C_{97}H_{27}$, and $C_{33}H_{15}$. Following this nomenclature, benzene and an infinite graphene sheet are labeled with C6 and C∞ respectively.

The following magnetic atoms are investigated in this work: Ru, as a representative example

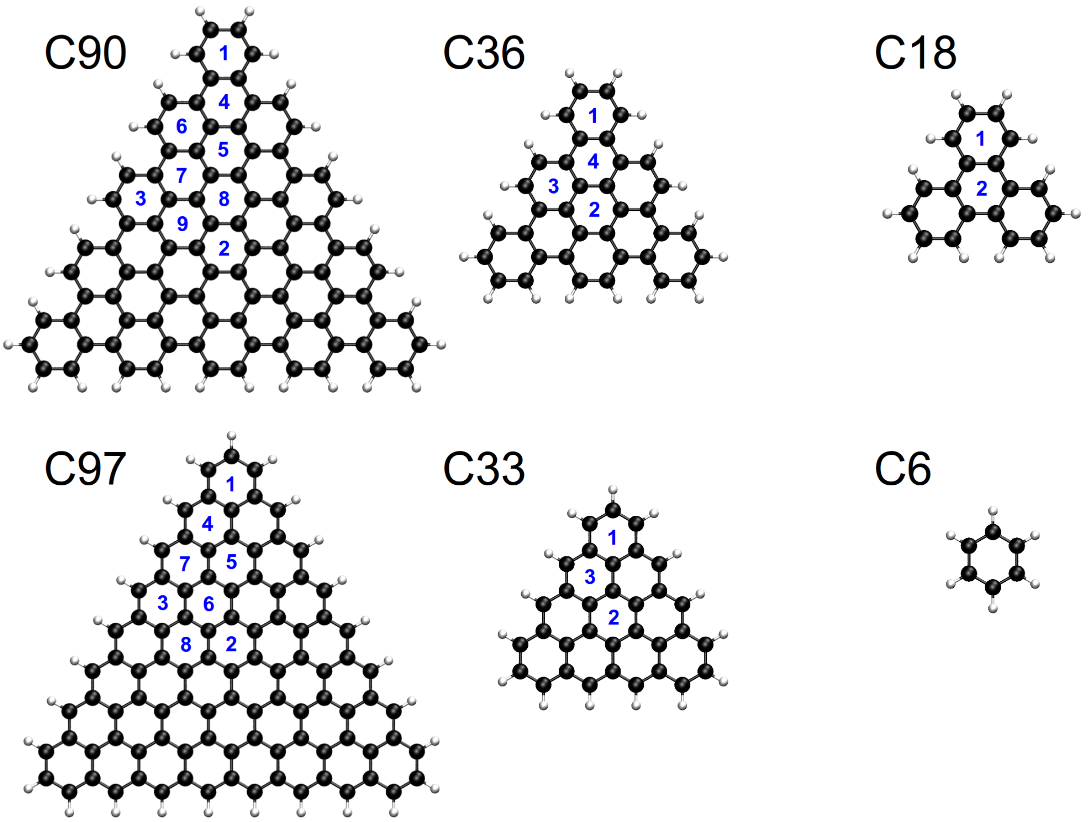

Figure 2.4: *The atomic structures of the investigated graphene nanoflakes and the benzene molecule. The labels accord to the number of carbon atoms (black spheres). The edges of the flakes are saturated with hydrogen (white spheres). The flakes C18, C36 and C90 have armchair edges. C33 and C97 have zigzag edges. Adsorption sites with distinctive symmetry are labeled with blue numbers, using the following scheme: Apex site is always 1; Center site, or the site closest to the center (in the case of C97) is always 2; Edge site (the site closest to the middle of the edge for C33 and C97) is always 3; the rest is numbered in ascending order starting from the apex of the triangle.*

of 4d TMs, and the elements of the 5d TM row from Hf to Ir. According to [28] the preferred position for Ru, as well as for all 5d TMs from Hf to Os is the hollow site, i.e. over the center of a carbon hexagon, compared to the top site, i.e. over a carbon atom, and to the bridge site, i.e. over the middle of a carbon-carbon bond. For Ir the bridge site was found to be equally favorable as the hollow site [28]. The hollow site was used as an adsorption site throughout the study.

Since the finite size of the flakes breaks the symmetry between the possible adsorption sites, compared to graphene, all sites with different symmetries were investigated, as indicated in Figure 2.4. The sites of higher symmetry are at the apex of the triangle, labeled as 1 in Figure 2.4, in the center, labeled as 2 in Figure 2.4 (on C97 flake there are three sites around the flake center, so that the symmetry is lower compared to C90), and in the middle of an edge, labeled as 3 in Figure 2.4. We call them **Apex**, **Center**, and **Edge** respectively. All other sites are labeled according to the Figure 2.4.

3 Density Functional Theory

The density functional theory (DFT) is a method for determining the ground state of a many-body system, more specifically of solids, molecules, and even atoms. As the name suggests, the concept of a functional of spatially distributed electron density is used throughout the theory. Since its inception in 1964, DFT has been very popular in solid state physics; and after improvements of treatment of exchange and correlation (see below) in the 1990s, it got established even in quantum chemistry and chemical physics. For the development of DFT Walter Kohn, although physicist by education, was awarded a Nobel Prize in chemistry in 1998.

Before DFT was invented, the de facto calculation method for the electronic structure in quantum chemistry was Hartree-Fock (HF) [71]. Within HF the many-body, multi-electron Schrödinger equation is approximated to a set of single-electron wave functions moving in a self-consistent mean field created by all other electrons in the system. Thus, the stationary N-electron wave function depends on $3N$ variables (the spatial coordinates for each of the constituting electrons), which rendered it computationally expensive with increasing number of electrons in the system.

The main advantage of DFT over HF is that it describes the electronic system in form of an electron density functional, significantly reducing the number of variables regardless the size of the system. The most important principle of the density functional theory is Hohenberg-Kohn Theorems, which are described below.

3.1 Hohenberg-Kohn-Theorem

The Hohenberg-Kohn theorem, published in 1964, is an, expressed more generally, exact theory for a system of interacting electrons (here Born-Oppenheimer approximation is assumed to be applicable for the system at hand), where the Hamiltonian can be written as

$$\hat{H} = -\frac{\hbar^2}{2m_e}\sum_i \nabla_i^2 + \sum_i V_{ext}(\mathbf{r}_i) + \frac{1}{2}\sum_{i\neq j}\frac{e^2}{|\mathbf{r}_i - \mathbf{r}_j|} \tag{3.1}$$

with reduced Planck's constant $\hbar$, electron mass m_e, external potential $V_{ext}(\mathbf{r}_i)$, electron charge e, and electron position $\mathbf{r}$.

P. Hohenberg and W. Kohn formulated two theorems. The first Hohenberg-Kohn theorem can very intuitively be described by a schematic in Figure 3.1. It says: For any system of interacting electrons in an external potential $V_{ext}(\mathbf{r})$, the potential $V_{ext}(\mathbf{r})$ is determined uniquely, except for a constant, by the ground state electron density $n_0(\mathbf{r})$ [32].

$$\begin{tikzcd}
V_{\text{ext}}(\mathbf{r}) \arrow[d, Rightarrow] & n_0(\mathbf{r}) \arrow[l, Rightarrow, "\text{HK}"'] \arrow[r, Leftrightarrow, "\text{KS}"] & n_0(\mathbf{r}) \arrow[r, Rightarrow, "\text{HK}_0"] & V_{\text{KS}}(\mathbf{r}) \arrow[d, Rightarrow] \\
\Psi_i(\{\mathbf{r}\}) \arrow[r, Rightarrow] & \Psi_0(\{\mathbf{r}\}) \arrow[u, Rightarrow] & \psi_{i=1,N_e}(\mathbf{r}) \arrow[u, Rightarrow] & \psi_i(\mathbf{r}) \arrow[l, Rightarrow]
\end{tikzcd}$$

Figure 3.1: *A schematic of the Konh-Sham approach [32].*

As a consequence, all states, which are determined by the Hamiltonian, that varies only by the external potential, are completely determined by the ground state density $n_0(\mathbf{r})$. Therefore, also the total energy $E_{tot}[n]$ of the system is also a functional of $n_0(\mathbf{r})$, as well as its parts: the kinetic energy $T[n]$ and the potential energy $E_{ext}[n] + E_{Ne}[n] + E_{ee}[n]$, with the potential energy E_{ext} and E_{Ne} of electrons in the external potential V_{ext} and in the potential of the nuclei V_{Ne}, and the electron-electron interaction energy E_{ee}. Since the potential of the nuclei V_{Ne} and an external potential V_{ext} behave in very similar fashion, they both can be represented by V_{Ne} (now it can be read as [N]uclei and [e]xternal). The total energy can therefore be written as:

$$\begin{aligned} E_{tot}[n] &= E_{ext}[n] + E_{Ne}[n] + E_{ee}[n] + T[n] = \\ &= \int n(\mathbf{r})V_{Ne}(\mathbf{r}) + E_{ee}[n] + T[n] \\ &= \int n(\mathbf{r})V_{Ne}(\mathbf{r}) + F_{HK}[n] \end{aligned} \tag{3.2}$$

with Hohenberg-Kohn functional $F_{HK}[n] = E_{ee}[n] + T[n]$, explicit form of which is completely unknown, except for the classical part of the electron-electron interaction energy $J[n]$

$$E_{ee} = \frac{1}{2}\int\int \frac{n(\mathbf{r_1})n(\mathbf{r_2})}{r_{12}} d\mathbf{r_1} d\mathbf{r_2} + E_{ncl} = J[n] + E_{ncl}[n] \tag{3.3}$$

with non-classical contribution $E_{ncl}[n]$ responsible for electron exchange and correlation energy. Hohenberg-Kohn functional in its commonly used form is:

$$F_{HK} = J[n] + E_{ncl}[n] + T[n] \tag{3.4}$$

The second Hohenberg-Kohn theorem says that $E_{tot}[n]$ delivers the lowest energy E_0 if and only if the density n is the true ground state density n_0.

$$E_0 \leq E_{tot}[n] = E_{Ne}[n] + F_{HK}[n] \tag{3.5}$$

Since the proof of Hohenberg-Kohn theorem is not relevant for the topic of this thesis, and it can easily be found in any book on DFT, e.g. [72], it will not be presented here. While Hohenberg and Kohn proved that the properties of the whole system depend only on the ground state density through a universal functional $F_{HK}[n]$, their theorem provides no hints on how the functional could look like, leaving it an interesting theoretical finding with initially little practical use. The way how to determine the ground state density came a year later by W. Kohn and L. J. Sham [73].

3.2 Kohn-Sham Approach

The Kohn-Sham approach simplifies the solution of the Schrödinger equation assuming that the ground state density of a many body system n can emerge from an auxiliary system of non-interacting particles. With $\varphi_i(\mathbf{r}, \sigma)$ being single-particle wave functions of the non-interacting particles with spin σ, the density is calculated as

$$n(\mathbf{r}) = \sum_i^N \sum_\sigma |\varphi_i(\mathbf{r}, \sigma)|^2 \tag{3.6}$$

Independent particles moving in an auxiliary potential V_{aux} follow the Schrödinger equation

$$[-\frac{\hbar}{2m}\nabla^2 + V_{aux}(\mathbf{r})]\varphi_i(\mathbf{r}, \sigma) = \varepsilon_i \varphi_i(\mathbf{r}, \sigma) \tag{3.7}$$

and have the total energy

$$E_S[n] = T_S[n] + \int V_{aux}(\mathbf{r})n(\mathbf{r})d\mathbf{r} \tag{3.8}$$

with the kinetic energy of non-interacting particles

$$T_S[n] = -\frac{\hbar}{2m}\sum_i^N < \varphi_i|\nabla^2|\varphi_i >= -\frac{\hbar}{2m}\sum_i^N \sum_\sigma \int \varphi_i(\mathbf{r}, \sigma)\nabla^2\varphi_i(\mathbf{r}, \sigma)d\mathbf{r} \tag{3.9}$$

where the subscript S stands for "single-particle". A direct formulation of T_S in terms of n is not known, but the expression $T[n]$ is still correct, since, according to the Hohenberg-Kohn theorem, the ground state of the system, including the ground state wave functions, is a functional of n: $\varphi_i = \varphi_i[n]$. According to the second Hohenberg-Kohn theorem, this functional $E_{tot}[n]$ has to be minimized in order to find the ground state density n_0. Solving the Euler-Lagrange equations with a boundary condition $N = \int n(\mathbf{r})d(\mathbf{r})$ and the Lagrange multiplier λ, one obtains

$$0 = \frac{\delta}{\delta n(\mathbf{r})}\left[E_S[n] - \lambda\left(\int n(\mathbf{r})d\mathbf{r} - N\right)\right] = \frac{\delta T_S[n]}{\delta n(\mathbf{r})} + V_{aux}(\mathbf{r}) - \lambda \tag{3.10}$$

Keeping this equation for an auxiliary system in mind, we focus our attention to the system of interacting particles.

Kohn and Sham reformulated the Eq. 3.4, splitting the kinetic term $T[n]$ in two parts. First part is the classical kinetic energy $T_S[n]$ (see Eq.3.9) of a system of independent particles with the density n. An expression for the second part $T_C[n] = T[n] - T_S[n]$ ('c' for 'correlation') is unknown, so Kohn and Sham combined it with also unknown $E_{ncl}[n]$ to a so-called exchange-correlation potential $E_{XC}[n]$, which is therefore

$$E_{XC}[n] \equiv (T[n] - T_S[n]) + (E_{ee}[n] - J[n]) \tag{3.11}$$

.

Using this reformulation, the number of unknown terms in Eq.3.2 is reduced to E_{XC}:

$$\begin{aligned} E_{tot}[n] &= T_S[n] + E_{Ne}[n] + J[n] + E_{XC}[n] \\ &= -\frac{1}{2}\sum_i^N \int < \varphi_i(\mathbf{r_1})|\nabla^2|\varphi_i(\mathbf{r_1}) > d\mathbf{r_1} \\ &- \int V_{Ne}(\mathbf{r})n(\mathbf{r_1})d\mathbf{r_1} \\ &+ \frac{1}{2}\int\int n(\mathbf{r_1})\frac{1}{r_{12}}n(\mathbf{r_2})d\mathbf{r_1}d\mathbf{r_2} \\ &+ E_{XC}[n] \end{aligned} \tag{3.12}$$

Minimizing this energy, again using Euler-Lagrange equations, one gets

$$\begin{aligned} 0 &= \frac{\delta}{\delta n(\mathbf{r})}\left[E_{tot}[n] - \lambda\left(\int n(\mathbf{r})d\mathbf{r} - N\right)\right] \\ &= \frac{\delta T_S[n]}{\delta n(\mathbf{r})} + \frac{\delta E_{Ne}[n]}{\delta n(\mathbf{r})} + \frac{\delta J[n]}{\delta n(\mathbf{r})} + \frac{\delta E_{XC}[n]}{\delta n(\mathbf{r})} - \lambda \\ &= \frac{\delta T_S[n]}{\delta n(\mathbf{r})} + V_{Ne}(\mathbf{r}) + \int \frac{1}{|\mathbf{r}-\mathbf{r_2}|}n(\mathbf{r_2})d\mathbf{r_2} + \frac{\delta E_{XC}[n]}{\delta n(\mathbf{r})} - \lambda \end{aligned} \tag{3.13}$$

If now we compare this equation with Eq.3.10, it can be seen, that one can define

$$V_{aux}(\mathbf{r}) = V_{Ne}(\mathbf{r}) + \int \frac{1}{|\mathbf{r}-\mathbf{r_2}|}n(\mathbf{r_2})d\mathbf{r_2} + \frac{\delta E_{XC}[n]}{\delta n(\mathbf{r})}, \tag{3.14}$$

and then the auxiliary system of non-interacting particles can deliver the same ground state density, as the original interacting system, as presented in Figure 3.1. The single-particle equation to solve is

$$\begin{aligned} \varepsilon_i\varphi_i(\mathbf{r},\sigma) &= [-\frac{\hbar}{2m}\nabla^2 + V_{aux}(\mathbf{r})]\varphi_i(\mathbf{r},\sigma) \\ &= [-\frac{\hbar}{2m}\nabla^2 + V_{Ne}(\mathbf{r}) + \int \frac{1}{|\mathbf{r}-\mathbf{r_2}|}n(\mathbf{r_2})d\mathbf{r_2} + \frac{\delta E_{XC}[n]}{\delta n(\mathbf{r})}]\varphi_i(\mathbf{r},\sigma) \\ &= [-\frac{\hbar}{2m}\nabla^2 + V_{Ne}(\mathbf{r}) + \int \frac{1}{|\mathbf{r}-\mathbf{r_2}|}n(\mathbf{r_2})d\mathbf{r_2} + V_{XC}(\mathbf{r})]\varphi_i(\mathbf{r},\sigma) \end{aligned} \tag{3.15}$$

In the last line we replaced $\frac{\delta E_{XC}[n]}{\delta n(\mathbf{r})}$ with $V_{XC}(\mathbf{r}) = \frac{d(n(\mathbf{r})\epsilon_{XC}(n(\mathbf{r}))}{dn}$, under assumption that

$$E_{XC}[n] = \int n(\mathbf{r})\epsilon_{XC}(n(\mathbf{r}))d\mathbf{r} \tag{3.16}$$

where $\epsilon_{XC}(n)$ is the "exchange and correlation energy per electron of a uniform electron gas density n"[73]. It can be shown [74] that this assumption 3.16 is valid for sufficiently slowly varying $n(\mathbf{r})$.

Now, since $V_{aux}(\mathbf{r})$ in Kohn-Sham equations 3.15 depends on the density, these equations have to be solved self-consistently, in combination with Eq.3.6. As being computationally quite demanding and non-trivial to optimize, this step is usually done by a DFT-software package.

3.3 Density Functionals

Generally speaking, the exact expression for E_{XC} is unknown, and in last 30 years a plethora of different numerical, approximative formulations have been suggested [75–78]. The above mentioned form $E_{XC}[n] = \int n(\mathbf{r})\epsilon_{XC}(n(\mathbf{r}))d\mathbf{r}$ is one possible (approximative) formulation, called local density approximation (LDA), because here ϵ_{XC} depends only on the density at the position $\mathbf{r}$, or *locally*. Results, delivered by LDA were astonishing good for many systems in solid state physics, especially considering the fact that it was already mentioined by Kohn and Sham [73], but they themselves were rather reserved regarding its possible usefulness. In an extension of LDA, called local spin-density approximation (LSDA), the energy density ϵ depends on $n_\uparrow$ and $n_\downarrow$, separate electron densities for spin-up and spin-down electrons [73, 79].

Generally considered as more precise form for E_{XC} is delivered by the Generalized Gradient Approximation (GGA) for E_{XC}, commonly used nowadays. Here, except for the spin density $n_{\uparrow,\downarrow}$, ϵ also depends on its gradient:

$$E_{XC}^{GGA} = \int n(\mathbf{r})\epsilon(n_\uparrow(\mathbf{r}), n_\downarrow(\mathbf{r}), \nabla_\mathbf{r} n_\uparrow(\mathbf{r}), \nabla_\mathbf{r} n_\downarrow(\mathbf{r})) \tag{3.17}$$

The next advanced widely used density functional type is a hybrid functional (without abbreviation). It uses another term in the E_{XC} – the Hartree-Fock exact exchange function E_X^{HF}:

$$E_X^{HF} = -\frac{1}{2}\sum_{i,j}\int\int \varphi_i^*(\mathbf{r_1})\varphi_j^*(\mathbf{r_1})\frac{1}{r_{12}}\varphi_i(\mathbf{r_2})\varphi_j(\mathbf{r_2})d\mathbf{r_1}d\mathbf{r_2} \tag{3.18}$$

The hybrid functional is a linear combination of E_X^{HF} and any other known density functional, e.g. E_{XC}^{GGA}, weighted with coefficients α, which are usually fitted to experimental data, or theoretically obtained using more sophtisticated methods. A simple example would be:

$$E_{XC}^{Hybrid} = \alpha E_X^{HF} + (1-\alpha)E_{XC}^{GGA} \tag{3.19}$$

There are also more sophisticated hybrid functionals, for example the widely used B3-LYP (Becke, three-parameter, Lee-Yang-Parr) functional:

$$E_{XC}^{B3-LYP} = E_X^{LSDA} + \alpha_0(E_X^{HF} - E_X^{LDA}) + \alpha_x(E_X^{GGA} - E_X^{LDA}) + E_C^{LDA} + \alpha_c(E_C^{GGA} - E_C^{LDA}) \tag{3.20}$$

Where the GGA exchange E_X^{GGA} and correlation E_C^{GGA} functionals were developed by, respectively, Becke [76], and Lee, Yand and Parr [80], and the LDA correlation functional E_C^{LDA} was developed by Vosko, Wilk and Nusair [81]. The LDA exchange here is the Slater exchange functional[76] (in atomic units):

$$E_X^{LSDA}[n] = -\frac{3}{2}\left(\frac{3}{4\pi}\right)^{1/3}\sum_\sigma\int n(\mathbf{r},\sigma)^{4/3}d\mathbf{r} \tag{3.21}$$

3.4 Two-Component Density Functional Theory

In order to calculate the magnetic anisotropy, magnetization direction $\vec{M}$ of the system has to be defined. It can be calculated from the magnetization density $\vec{m}(\mathbf{r})$, which is a three-dimensional vector field (note that both $\vec{X}$ and $\mathbf{X}$ are indicators that X is a vector), and is defined in terms of two-component wave functions

$$\varphi_i(\mathbf{r}) = \begin{pmatrix} \varphi_i^{\uparrow}(\mathbf{r}) \\ \varphi_i^{\downarrow}(\mathbf{r}) \end{pmatrix} \tag{3.22}$$

where $\varphi_i^{\uparrow}(\mathbf{r})$ and $\varphi_i^{\downarrow}(\mathbf{r})$ are complex spin up and spin down components of the wave function $\varphi_i(\mathbf{r})$. Using the Pauli matrices

$$\sigma_x = \begin{pmatrix} 0 & 1 \\ 1 & 0 \end{pmatrix}; \quad \sigma_y = \begin{pmatrix} 0 & -i \\ i & 0 \end{pmatrix}; \quad \sigma_z = \begin{pmatrix} 1 & 0 \\ 0 & -1 \end{pmatrix} \tag{3.23}$$

the vector field $\vec{m}(\mathbf{r})$ is defined as

$$\vec{m}(\mathbf{r}) = \sum_i \varphi_i(\mathbf{r})^{\dagger} \vec{\sigma} \varphi_i(\mathbf{r}) \tag{3.24}$$

The magnetization direction $\mathbf{M}$ of the whole system is obviously

$$\vec{M} = \int \vec{m}(\mathbf{r}) d\mathbf{r} \tag{3.25}$$

The density $n(\mathbf{r})$ of the system in this terms is defined the same way as before (see Eq. 3.6) with a note, that $\varphi_i(r)$ is now a two-dimensional vector with two complex components:

$$n(\mathbf{r}) = \sum_i^N |\varphi_i(\mathbf{r})|^2 = \sum_i^N \varphi_i^{\dagger}(\mathbf{r}) \varphi_i(\mathbf{r}) \tag{3.26}$$

Now, we go back to the Kohn-Sham approach, and see that the only spin-dependent component in the total energy (Eq. 3.12)

$$E_{tot}[n] = T_S[n] + E_{Ne}[n] + J[n] + E_{XC}[n], \tag{3.27}$$

is $E_{XC}[n]$, which is now a functional of two spin densities, while for the other components the two spin-densities are decoupled. The two spin-densities can be replaced my the total spin density n and the magnetization density $\vec{m}$, so that $E_{XC} = E_{XC}[n, m]$.

The two-component Kohn-Sham equations get the following shape:

$$\varepsilon_i \varphi_i(\mathbf{r}) = [-\frac{\hbar}{2m}\nabla^2 + V_{Ne}(\mathbf{r}) + \int \frac{1}{|\mathbf{r} - \mathbf{r_2}|} n(\mathbf{r_2}) d\mathbf{r_2} + V_{XC}(\mathbf{r}) + b_{XC}(\mathbf{r})] \varphi_i(\mathbf{r}, \sigma) \tag{3.28}$$

with the two-component wave function $\varphi_i(\mathbf{r})$, and an additional functional derivative

$$b_{XC}(\mathbf{r}) = -\frac{\delta E_{XC}[n, m]}{\delta \vec{m}(\mathbf{r})} \tag{3.29}$$

Same as for one-component Kohn-Sham equations, with the choice of a proper functional $E_{XC}[n, m]$, the equation system can be solved self-consistently, which was done in the scope of my work by the quantum-mechanical software TURBOMOLE [82].

In TURBOMOLE the wave function $\varphi_i(\mathbf{r})$ is represented by a basis set of Slater-type orbitals. Large basis sets give a better approximation to the real wave functions. Small basis sets allow smaller calculation times, and can be used for preliminary results or for initial calculations, bringing the density faster to the desired shape before using the large basis sets. To start self-consistent calculations, an initial guess is needed. Usually a Hückel guess [85] is used, an approximation based on tight-binding model.

3.5 Determining the Magnetic Anisotropy

The preliminary two-component calculations on the underlying system showed, that the convergence to the state of the true magnetic direction was too CPU-time intensive, as we were observing very small variations of the energy with the changing magnetic direction within few degrees. Additionally, to determine the magnetic anisotropy energy, one has to determine the energy of the system state with magnetic moment pointing in a reference direction, which can be chosen arbitrary (usually this is one of the symmetry axes of the system). Running DFT calculation with the initial magnetization in a reference direction (which is not necessarily representing the minimum energy of the system), can often lead to the relaxation of the system in another magnetization direction, giving a wrong reference energy.

As a solution to both problems, the following technique was applied. First, a usual one-component calculation was carried out. When it was well converged, the wave functions were projected on a two-component wave function with the same density n. A two-component calculation requires an initial guess for the magnetization direction. To calculate the magnetic anisotropy, two reference magnetization directions are chosen as an initial guess for two calculations on a system with the same density n. The relaxation to a different magnetic state was prevented without modifying the DFT code, by increasing the damping coefficient.

Now we consider which directions can be taken as reference. On a graphene layer, a magnetic adatom with a magnetic anisotropy can have a magnetic moment pointing either perpendicular to the carbon plane (the *out-of-plane* magnetization), or parallel to the carbon plane (the *in-plane* magnetization). In the latter case, all *in-plane* magnetization directions are equivalent, as long as the substrate is infinite, due to its symmetry (or rather three directions are degenerate as the graphene sheet still has a locally non-uniform structure, i.e. the atomic structure, unlike an ideal 2D sheet). The magnetic anisotropy energy E_{MAE} could be defined as

$$E_{MAE} = E_{out-of-plane} - E_{in-plane} \tag{3.30}$$

In the case of a finite graphene flake with an adatom above one carbon ring, the in-plane symmetry is much stronger broken by the edges and the three-fold symmetry is lifted. Among all possible magnetization directions, there has to be, usually only one, preferred in-plane direction and, of course, one least favorable in-plane direction. If we call the corresponding energies $E_{in-plane,min}$ and $E_{in-plane,max}$, we can define a second anisotropy energy, so-called *in-plane anisotropy energy* E_{IP} which would be valid only for non-infinite substrate:

$$E_{IP} = E_{in-plane,max} - E_{in-plane,min} \tag{3.31}$$

In order to avoid any misunderstandings, we call the anisotropy energy defined in the previous paragraph the *in- vs. out-of-plane anisotropy energy* E_{IOP} and define it as

$$E_{IOP} = E_{out-of-plane} - E_{in-plane,min} \tag{3.32}$$

3.6 Grimme Dispersive Correction

3.6.1 DFT-D

The local density functionals, like GGA and LDA, are unable to take into account the long-range interactions, such as van der Waals (dispersive, *vdW*) interaction. To include the *vdW* interaction, Stefan Grimme, convinced [86] that rigorous non-empirical approaches would necessarily end up in very complex and numerically intensive methods, introduced in 2004 an empirical dispersive (DFT-D) correction to the energies calculated directly with DFT or HF:

$$E_{DFT-D} = E_{DFT} + E_{disp} \tag{3.33}$$

The correction E_{disp} is calculated as follows [86]:

$$E_{disp} = -s_6 \sum_{i=1}^{N_{at}-1} \sum_{j=i+1}^{N_{at}} \frac{C_6^{ij}}{R_{ij}^6} f_{dmp}(R_{ij}) \tag{3.34}$$

with the number of atoms in the system N_{at}, the dispersion coefficient C_6^{ij} for atom pair *ij*, the inter-atomic distance R_{ij}, the global scaling factor s_6 and the damping function $f_{dmp}(R_{ij})$ to avoid near-singularities at small distances. f_{dmp} is defined as:

$$f_{dmp}(R_{ij}) = \frac{1}{1 + e^{-\beta(R_{ij}/R_{0,ij}-1)}} \tag{3.35}$$

where $R_{0,ij}$ is sum of the *vdW* radii of both atoms within the pair and the prefactor $\beta = 23.0$ is determined from the requirement $f_{dmp}(R_{ij} = 1.2R_{0,ij}) = 0.99$, as proposed in [87]. The *vdW* radii are derived from the theoretical calculations by multiplying the radius of the 0.1 au isosurface of the electron density of the atoms, calculated by using the restricted open-shell Hartree-Fock (ROHF) with TZV basis set, with an empirical factor $l_r = 1.22$.

The dispersion coefficients C_6^{ij} are calculated from the atomic C_6 as follows:

$$C_6^{ij} = 2\frac{C_6^i C_6^j}{C_6^i + C_6^j} \tag{3.36}$$

The C_6 coefficients are taken from [87], but are averaged over the hybridization states (in [87] different C_6 coefficients are introduced, e.g. for carbon in sp^3, sp^2 and sp hybridization states) to improve the generality of the correction.

The global scaling factor s_6 depends on the used exchange-correlation functional, and is determined in [86] using a "fit-set" of molecules.

3.6.2 DFT-D2

Two years later Grimme published an improved version of the DFT-D, called DFT-D2 [88]. It still utilizes Equation 3.34, but certain parameter modifications were included to improve the computed energies and inter-atomic distances, and expand the applicability of the correction to a larger part of the periodic table of elements.

The factor l_r used for the determination of the *vdW* radii is set to l_r =1.10. The prefactor β used in the damping function (see Equation 3.35) is reduced to β =20. A major change is the determination of the dispersion coefficients C_6^{ij}, which is calculated as

$$C_6^{ij} = \sqrt{C_6^i C_6^j} \tag{3.37}$$

in DFT-D2, which required refitting of the scaling factors s_6.

The atomic C_6 coefficients are also redefined in DFT-D2 [88] as

$$C_6^i = 0.05 N I_p^i \alpha^i \tag{3.38}$$

with the atomic ionization potential I_p and the static dipole polarizability α, calculated using the DFT with PBE0 hybrid exchange-correlation functional. Depending on the row of the periodic table, the number N acquires the values 2, 10, 18, 36, and 54 for atoms from rows 1-5.

4 Ruthenium as a Magnetic Center on Graphene Nanoflake-Based Single Ion Magnets

In order to construct a functional single molecule switch, as it was introduced in Chapter 2, we consider graphene nanoflakes as ligands for a single transition metal (TM) atom as magnetic center. There is a number of studies on TM atoms adsorbed on graphene-based structures [23–31] reporting good adsorption properties and large magnetic anisotropies [23, 24, 27, 29], which could be utilized e.g. to build a single ion magnet (SIM). In our study we consider using 4d TMs as magnetic centers, because the spin-orbit coupling of 4d TMs is expected to be high enough to provide a significant anisotropy. Among the 4d TMs ruthenium (Ru) was chosen for a case study, as this element is isoelectronic to iron, which is one of the most widely used elements in single molecule magnets [89–93] and spin-crossover molecules [22, 61, 94–97].

Considering that the edge of graphene is also an inevitable part of experiments, here we investigate the influence of the graphene edge on the adsorption and magnetic properties of Ru on triangular graphene nanoflakes, which is in clear contrast to the previous studies that present, to the best of our knowledge, either infinite graphene sheet or a single benzene ring as adsorbent. For Ru on different adsorption positions (*sites*) on the zigzag flakes C33 and C97 and the armchair flakes C36 and C90 (introduced in Figure 2.4) we calculate the binding energy E_b, the magnetic moment m and the magnetic anisotropy energies E_{IP} and E_{IOP}.

4.1 Magnetic Properties of Pure Graphene Nanoflakes

We start with an investigation of influence of both edge types on the electronic and magnetic properties of non-decorated (pure) triangular graphene nanoflakes. It is known [98] that triangular zigzag nanoflakes are magnetic. This can, further, lead to instability of the system in the given shape. To investigate this question, DFT calculations were done on pure armchair-edged and zigzag-edged graphene flakes C90 and C97. Their calculated spin densities are shown in Figure 4.1.

The zigzag flake shows a strong magnetic moment of $7\,\mu_\mathrm{B}$, where μ_B is Bohr magneton ($1\,\mu_\mathrm{B}$ is the magnetic moment of one unpaired electron). The state of the flake is ferrimagnetic: the total magnetic moment of C atoms is $12.6\,\mu_\mathrm{B}$ in one sublattice and $-5.6\,\mu_\mathrm{B}$ in the other sublattice, summing up to $7.0\,\mu_\mathrm{B}$. Additional calculations on the zigzag flake [1] show that if the zigzag flake is forced to a state with magnetic moment of $1\,\mu_\mathrm{B}$, the total energy is 1.237 eV higher, indicating the strong stability of the $7\,\mu_\mathrm{B}$ state.

---

[1] Calculation details: BP86 [76, 77, 81, 99, 100] exchange-correlation functional and the dhf-TZVP-2c two-component basis set

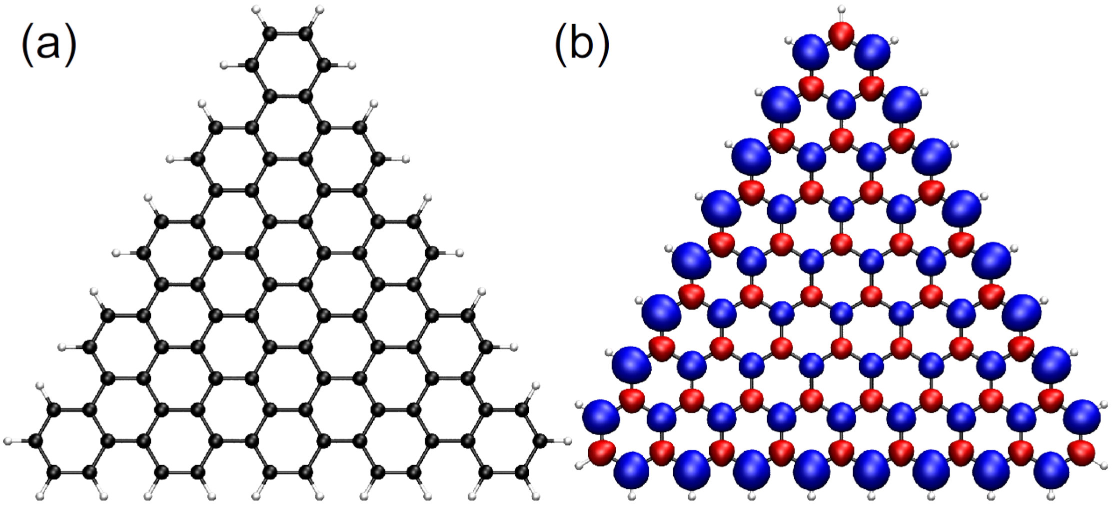

Figure 4.1: *The structure and the spin density of triangular nanoflakes C90 with armchair (a) and C97 with zigzag (b) edge type. The carbon atoms and the hydrogen atoms are represented by black and white spheres respectively. The spin density is the local charge density difference between spin-up and spin-down charge densities. It is shown as an isosurface at the value of* $0.003\,\mathrm{e/a_0}^3$ *(blue) and* $-0.003\,\mathrm{e/a_0}^3$ *(red) with electron charge* $e = 1.602 \times 10^{-19}\,\mathrm{C}$ *and the Bohr radius* $a_0 = 5.292 \times 10^{-11}\,\mathrm{m}$. *The zigzag flake shows a clear intrinsic magnetic moment, with a magnetization asymmetry between the two graphene sublattices and magnetization being strongest at the edge. The armchair flake shows no intrinsic magnetic moment.*

Two-component calculations are also performed in order to check the magnetic anisotropy and a possible non-collinearity of the magnetic moments of single carbon atoms. They show that all atomic magnetic moments in the system are aligned along the same axis and that there is no difference in the energy if this axis is rotated by 90 degrees (from out-of-plane to in-plane direction with respect to the flake plane).

The high magnetic moment of triangular zigzag flakes can be explained by considering the symmetry of this flake. Since the honeycomb structure of graphene has two sublattices, for atoms at the positions (0;0) and ($\frac{1}{\sqrt{3}}$;0) in the elemental cell respectively, a broken symmetry between them leads to magnetic moment, according to the theorem of magnetism in a bipartite lattice at half filling by Lieb [101]. The magnetic moment of $7\,\mu_\mathrm{B}$ exactly equals the difference of atom numbers between the two sublattices. The carbon atoms at the very edge belong to the same sublattice and have the same magnetization direction (blue spin density in Figure 4.1b), while the other sublattice is in minority and has the opposite magnetization (red spin density in Figure 4.1b). In the case of armchair triangular flake, the symmetry between the sublattices is preserved, leading to zero magnetic moment.

4.2 Binding Energies

To characterize the adsorption properties of single ruthenium adatom on graphene nanoflakes, the binding energies were calculated at symmetry non-equivalent sites (carbon rings), as introduced in Figure 2.4. The flake is considered lying in the x-y-plane. Further we call the z-coordinate of the adatom the *adatom-flake distance*, or the *elevation*. The binding energy E_b is defined here as the total energy difference between the adatom at 99 Å elevation above the flake and the adatom at the most stable elevation over the current site:

$$E_b = E_{tot}(99\text{Å}) - \min(E_{tot}(z)) \tag{4.1}$$

In the case of binding, E_b is, therefore, positive. The binding energies of Ru on different sites of the zigzag flakes C33 and C97 and the armchair flakes C36 and C90 are shown in Figure 4.2. For the DFT calculations we used the BP86 exchange-correlation functional with dhf-TZVP-2c basis set. In accordance with previous reports [70, 102, 103], the edge sites are the most preferable for the adatom regardless the edge type. **Apex** was found to be the most preferable adsorption site for the Ru adatom.

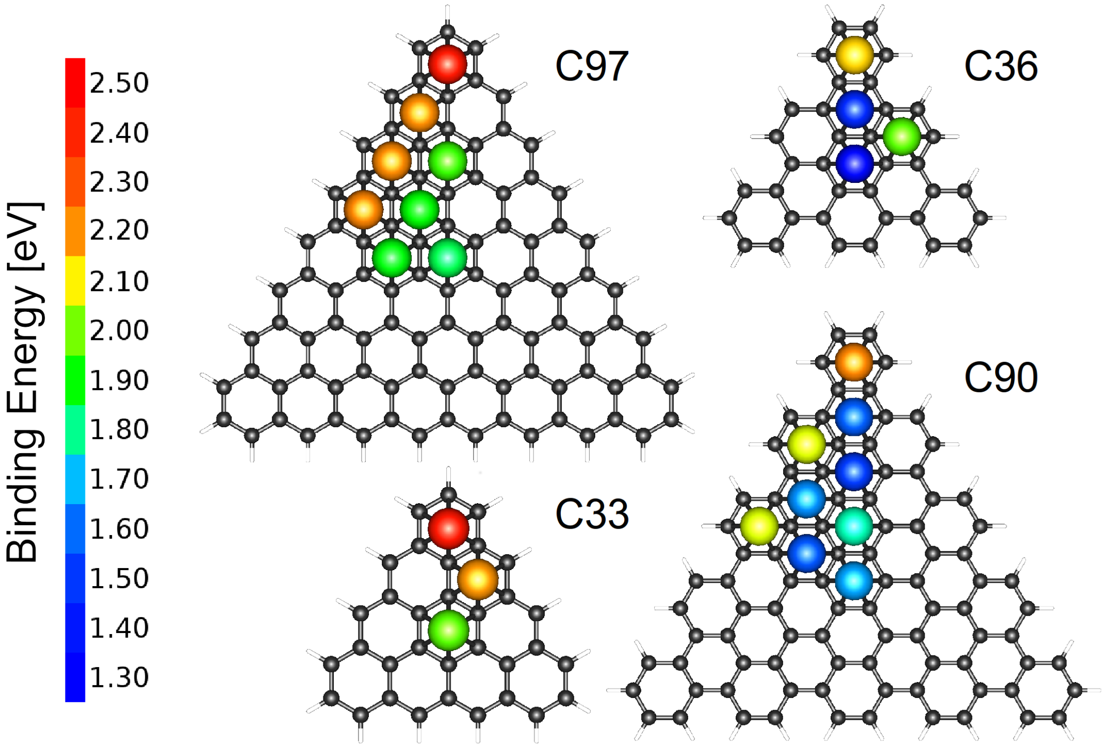

Figure 4.2: *Binding energy E_b of a single Ru atom on graphene nanoflakes with zigzag (C33 and C97) and armchair (C36 and C90) edge as a function of the adsorption site. The apex site is the most binding for all flakes regardless the size and the edge type. The binding energies vary between* 1.3 eV *and* 2.5 eV.

On the zigzag flakes E_b is higher than on the armchair flakes. A clear trend is visible on zigzag flakes that the further from the edge the adsorption site is, the lower the binding energy is. This trend is less clear on the armchair flakes. For example, the site **5** on C90 (see Figure 2.4 for the site labeling) provides a weaker binding, than the **Center**, while **5** is closer to the edge. At the same time, the strongest binding among the off-edge sites on C90 is calculated on the site **8**, which is not close to the edge.

For the zigzag flakes, E_b at the edge is independent of the flake size, while at the **Center** E_b goes deeper on the bigger flake as this site is farther from the edge there. On the armchair flakes the E_b is stronger on the bigger flakes regardless the position. This finding indicates that the binding mechanism at the edge of a zigzag flake is more localized around the adatom. The interaction of the adsorbate with the armchair flake has a stronger long-range character, which leads to the binding energy fluctuations from site to site among the off-edge sites, and to the size dependence of E_b even on the edge sites.

In order to investigate the presence of the spin-crossover behavior, as reported by Virgus et al. [31] for Co on benzene ring and graphene, we calculate the total energy for the C36 flake with Ru atom as a function of the adatom-flake distance. The resulting energy profiles for four adsorption sites are shown in Figure 4.3. A second energetic minimum at $\approx$2.8 Å distance is clearly seen for Ru on the **Center** site and the site **4**. To investigate the potential of such bistability for a single molecule magnetic switch, in the next section we focus on the magnetic properties of Ru adsorbed on the graphene flakes. We first focus on the Ru state in the global energetic minimum.

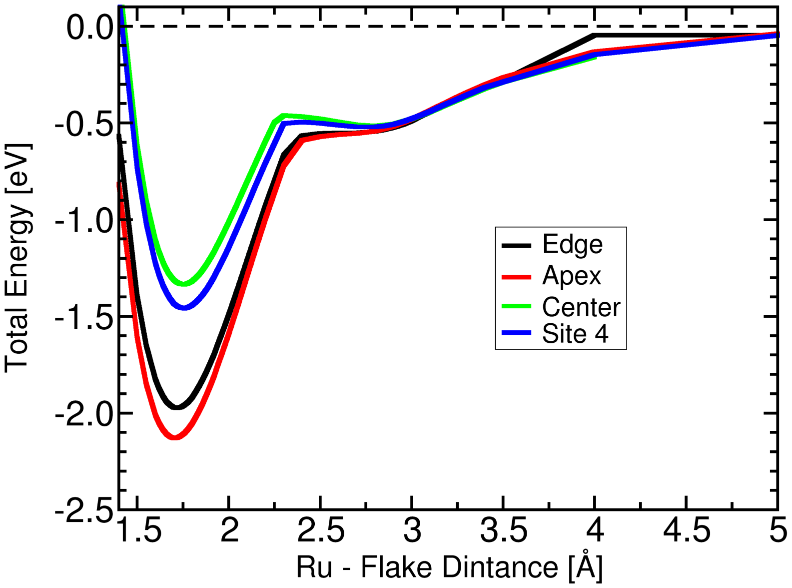

Figure 4.3: *The total energy (relative to the free state) of the C36 nanoflake with Ru adatom as function of the vertical distance between the Ru atom and the flake plane. The energy profiles are calculated for Ru adsorbed on four symmetry inequivalent sites. The DFT calculation is done using the BP86 GGA exchange-correlation functional with def2-SVP basis set and the DFT-D2 dispersion correction. Two metastable positions are clearly distinguishable at the sites **4** and **Center**.*

4.3 Magnetic Properties of Ru Atom on Graphene Nanoflakes

Upon adsorption on the graphene flake the electronic state of Ru atom changes from the atomic state $4d^7$ $5s^1$ with four unpaired electrons to the adsorbed state $4d^8$ $5s^0$ with two unpaired electrons. The electronic state of Ru at the metastable distance above the flake was found to be $4d^7$ $5s^1$, i.e. equivalent to the atomic state. This confirms the spin-crossover nature of the bistability which was reported in the previous section. In the global energetic minimum the magnetic moment localized at Ru is reduced due to the hybridization of the half-filled d-character molecular orbitals of Ru with the flake molecular orbitals, accompanied by an oxidation of Ru by the flake.

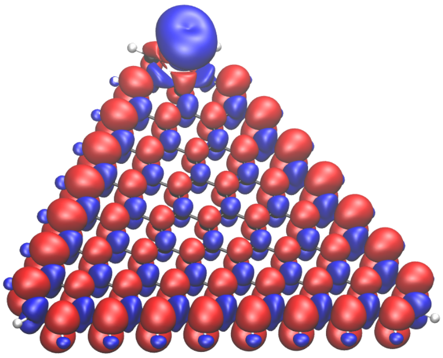

Figure 4.4: *Spin density of the zigzag graphene flake C97 decorated with a Ru adatom on* ***Apex*** *site. The magnetization direction of Ru is opposite to the overall magnetization of the flake, indicating antiferromagnetic coupling between the flake and the adatom.*

4.3.1 Magnetization Relative to the Flake

To characterize the interaction between the flake and the adatom, we first investigate the relative magnetization of the adatom with respect to the flake. The calculated spin-density of Ru on C97 flake is shown in Figure 4.4. The ferrimagnetic alignment of the magnetic momenta of graphene sublattices we found for a pure flake (Figure 4.1) is also clearly visible in presence of the adatom. The Ru atom aligns its magnetic moment against the flake majority spin, therefore reducing the total magnetic moment of the compound from $7\,\mu_B$ to $5\,\mu_B$, contributing $-2\,\mu_B$. A similar behavior is observed for C33 zigzag flake. Its intrinsic magnetic moment of $3\,\mu_B$ is partly compensated by Ru resulting in the total magnetic moment of $1\,\mu_B$.

As an additional test of such antiparallel alignment of the magnetic moment of ruthenium with respect to the flake magnetic moment, we force C33 with Ru into a ferromagnetic state where the magnetic moments of the flake and of Ru are oriented in the same direction (i.e. total magnetic moment of $5\,\mu_B$) (see Figure 4.5). This is done by rearranging the Kohn-Sham orbitals in such a way that all half-filled molecular orbitals located at Ru are moved from the minority to the majority channel, using an internal "flip" tool provided in the TURBOMOLE package [82]. This state is subsequently self-consistently relaxed without allowing the system to switch the total magnetic moment, and its energy is compared with the antiferromagnetic configuration. The ferromagnetic state shows $0.56\,\mathrm{eV}$ higher total energy, confirming the stability of the antiferromagnetic state. The calculations show that the preferred antiferromagnetic coupling between Ru atom and the flake is not dependent on the adsorption site.

The antiferromagnetic coupling of Ru magnetic moment and the intrinsic magnetic moment of the flake results in an additional diminishing of the Ru magnetic moment. The calculated magnetic moments for Ru on armchair flakes vary between 1.7 and $1.8\,\mu_B$, while on the zigzag

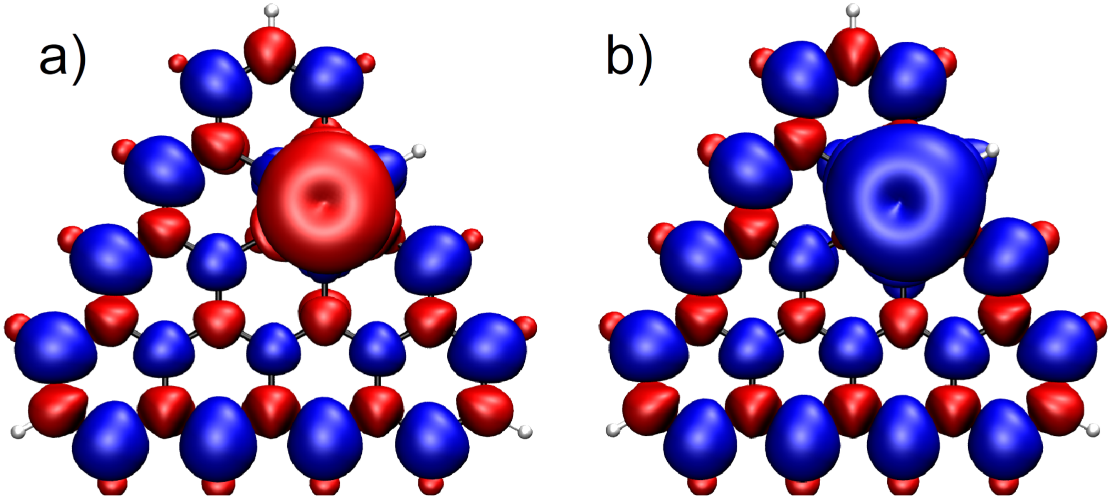

Figure 4.5: *Antiferromagnetism vs. ferromagnetism: the spin density of the C33 flake with Ru adsorbed on the* **Edge** *site. (a) The total magnetic moment is* $1\,\mu_\mathrm{B}$*. (b) The total magnetic moment is* $5\,\mu_\mathrm{B}$*. In (a) the magnetic moment produced by two unpaired electrons of Ru is aligned antiparallel to the magnetic moment of the flake (intrinsic magnetic moment is* $3\,\mu_\mathrm{B}$*), while in (b) they are parallelly aligned. The state (a) is more stable than (b) by* $0.56\,\mathrm{eV}$.

flakes it reaches values of only 0.8 - $1.4\,\mu_\mathrm{B}$ with the highest values calculated at the **Center** sites of C33 and C97. It might be also the reason for a stronger binding of Ru to the zigzag flake.

4.3.2 Magnetic Anisotropy

The in- vs. out-of-plane anisotropy energy E_{IOP}, as defined in Equation 3.32, is shown in Figure 4.6. Its value varies between 1.1 meV on **Edge** and 2.2 meV on **Center** on C97 and between 1.1 meV (**Edge**) and 1.7 meV (**Center**) on C33. E_{IOP} is positive on all sites, meaning that the preferred magnetization direction is in-plane. The preferred in-plane directions are shown in Figure 4.7 together with the corresponding in-plane magnetic anisotropy energy E_{IP}. The red arrows in Figure 4.7 point along the preferred magnetization axis, and their length is proportional to the magnetic moment of the Ru atom. Due to higher flake magnetization at the edge (see Figure 4.1) of zigzag nanoflakes, the magnetic moment of Ru is stronger reduced at the edges, which explains lower E_{IOP} there. The reason for higher E_{IP} at the edge is lowering of the symmetry, which induces pinning of the magnetization axis. The local symmetry at the central sites is higher, which leads to less pronounced pinning of the preferred magnetization direction. The maximum value of E_{IP} is 0.16 meV on **Edge** of C97.

In contrast to the strongly magnetic zigzag flakes, on the armchair flakes the only source of magnetism is the adatom itself (see Figure 4.8). Its magnetic moment is only slightly reduced by electron transfer between the Ru and the flake. This results in higher E_{IOP} values, which vary between 2.0 and 3.4 eV for C90 and between 1.9 and 3.5 eV for C36 (Figure 4.6). Opposite to the zigzag flake, the highest E_{IOP} values are not on the **Center**, but on the corresponding **Apex**. The in-plane pinning of the magnetization E_{IP}, though, is weaker than for the zigzag flake, reaching maximum values of 0.06 meV on C90 and 0.08 meV on C36 (Figure 4.7). The

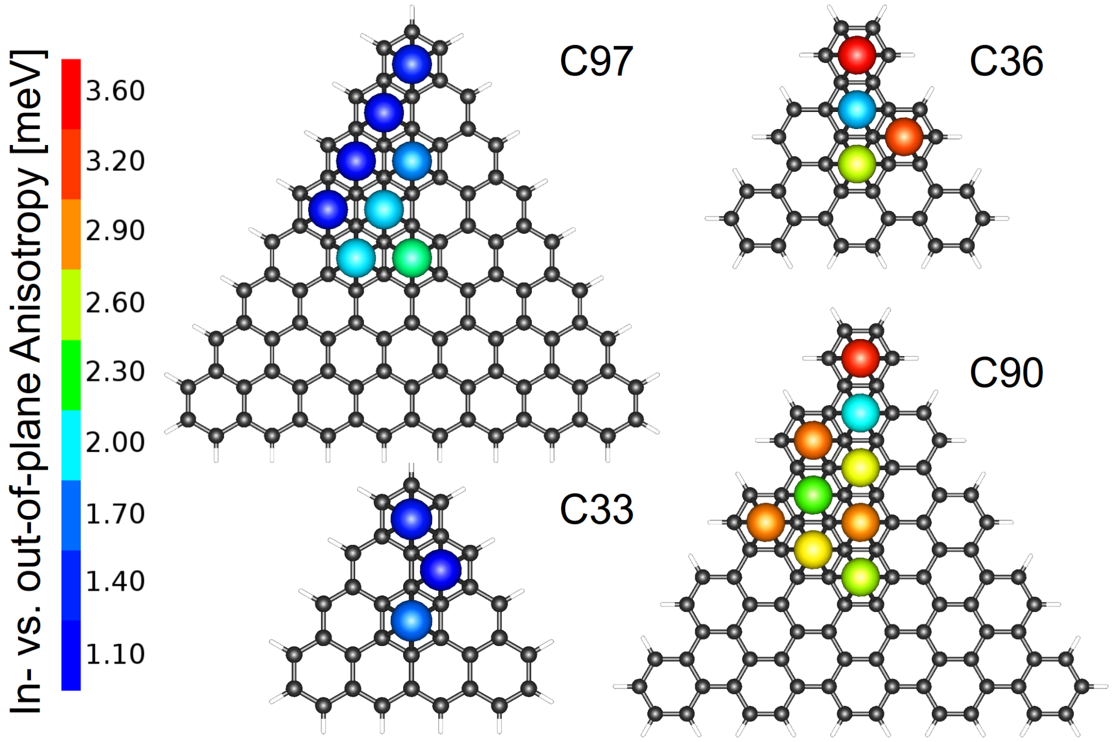

Figure 4.6: *In- vs. out-of-plane magnetic anisotropy energy E_{IOP} for a single Ru atom adsorbed to graphene nanoflakes C33, C36, C90 and C97 as a function of the adsorption site. E_{IOP} is positive(negative) when the preferred magnetization direction is in-plane (out-of-plane).*

highest values are determined on the edge sites as result of broken symmetry. On C36 the highest E_{IP} value is achieved at the site **4**.

Our general observation is that the E_{IP} is an order of magnitude smaller than E_{IOP}. We also note that the calculated preferred directions at the sites with the lowest E_{IP} values are less reliable, being very small numbers, which can be biased by numerical errors in the calculations. Otherwise, the preferred magnetization direction is perpendicular to the edge of the flake.

4.4 Discussion and Conclusions

For the study of Ru on the graphene nanoflakes following assumptions are made. First, after an initial geometry optimization of the pure flake no geometry optimizations are done after putting the adatom on it, assuming that the flake is fixed by a substrate. The second assumption is that the elevation of the adatom above the flake plane is constant for all sites. The optimal values determined by calculating of the total energies while varying the elevation of Ru above the flake, are 1.72 Å for C97, 1.71 Å for C33, 1.73 Å for C90 and 1.70 Å on C36. These assumptions allow us to reduce the computational effort while estimating the magnetic and energetic properties of Ru on graphene nanoflakes.

Our study allows us to well describe the magnetic interaction between Ru and the flake along with an estimate for the magnetic anisotropy energy in such compounds. We found that the magnetic moment of $4\,\mu_B$ of atomic Ru is reduced to $2\,\mu_B$ upon the adsorption. The interplay

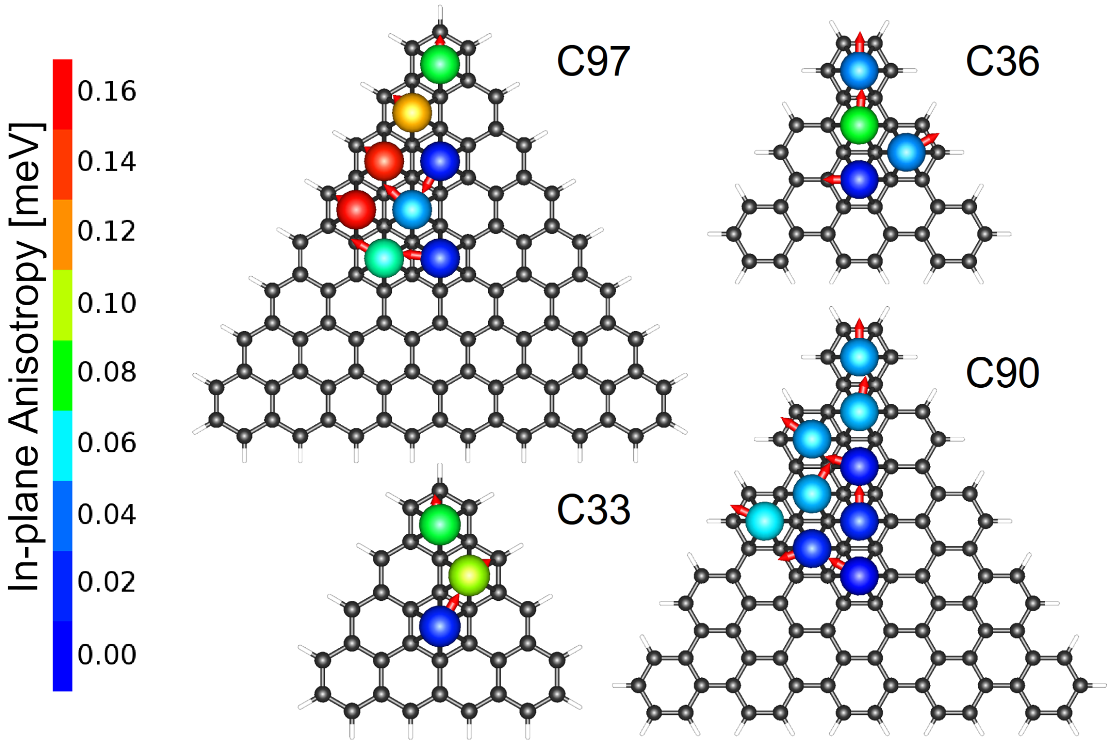

Figure 4.7: *In-plane magnetic anisotropy energy E_{IP} for a single Ru atom adsorbed to graphene nanoflakes C33, C36, C90 and C97 as a function of the adsorption site. E_{IP} is always positive. The preferred in-plane direction is indicated by red arrows. The arrow length is proportional to the magnetic moment of the Ru adatom.*

between the two electronic states results in structural bistability with two adsorption distances of 1.8 Å and 2.8 Å for Ru adsorbed on the off-edge sites of the C36 flake.

The values of the magnetic anisotropy energy for Ru on graphene nanoflakes are relatively small compared to room temperature. While the in- vs. out-of-plane anisotropy energy of 3.4 meV corresponds to the thermal energy of T =37 K ($E_{\text{thermal}} = k_B T$ with the Boltzmann constant k_B), and can be measured at cryogenic conditions, the in-plane pinning of the magnetic axis of 0.06 meV corresponds to 0.7 K, which is still achievable, but requires considerable experimental effort, and restricts the application of such structures to basic research.

In order to achieve higher anisotropy values, we focus our study on 5d transition metals, because of their higher spin orbit coupling providing potentially higher magnetic anisotropies. Our aim in the following chapter is to focus first on the interaction between a magnetic adatom and a nonmagnetic flake, leaving the investigation of a more complex interaction between the magnetic flake and a magnetic adatom for future research. Apart from that, an experimental evidence of triangular zigzag nanoflakes have not been reported yet to the best of our knowledge, while there is an experimental report on synthesis of triangular armchair nanoflakes [33].

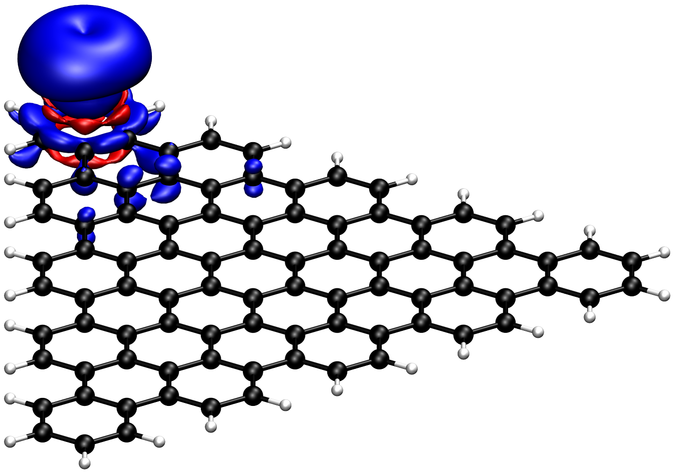

Figure 4.8: *Spin density of a single Ru adatom at the apex site of the graphene nanoflake C90 with armchair edge type. The presented shapes are the isosurfaces at 0.001* $\mathrm{e}/\mathrm{a}_0^3$ *(blue) and -0.001* $\mathrm{e}/\mathrm{a}_0^3$ *(red).*

5 5d Transition Metals on Graphene Nanoflakes: an Alternative Single Molecule Magnetic Switch

As we pointed out in Chapter 2, combining properties of single ion magnets (*SIM*) and spin-crossover (*SCO*) molecules may result in a single molecule magnetic switch (*SMMS*) with at least two states, which are potentially stable at high temperatures and can provide an easy information read out. As a potential candidate for SMMS we introduced graphene nanoflakes with a single transition metal (*TM*) atom adsorbed on top. Adsorbed atom (adatom) plays a role of a magnetic center, while the nanoflake acts as a ligand hull.

In Chapter 4 we showed that usage of ruthenium atoms as magnetic centers leads to a technologically insufficient anisotropy for room temperature devices due to the too low spin-orbit coupling. To achieve higher spin-orbit coupling, here we investigate 5d transition metal atoms as magnetic centers. As a representative example of the 5d TM, we choose osmium, which is isoelectronic to ruthenium and iron. We perform most of the calculations and method optimizations using osmium, before extending the calculations to the rest of 5d TM series.

This chapter is structured as follows: In Section 5.1 we calculate the binding energies of Os on graphene nanoflakes. In Section 5.2 we investigate the magnetic anisotropy of all 5d transition metals on graphene nanoflakes. Section 5.3 shows that the energy profile of Os upon annealing to the flake exhibits a double well. We explain this structural bistability by calculating the distance-dependent occupation of molecular orbitals close to HOMO, their atomic contributions, and hybridization (Section 5.3.1). In 5.3.2 we show how the bistability depends on the choice of the flake size and the adsorption site. In 5.3.3 we demonstrate a way to control the bistability by means of external electric field, before in 5.3.4 the rest of 5d TM series is found to show similar SCO behaviour. Finally, in the Section 5.4 we test the robustness of our findings against details of computational methods.

5.1 Binding Energies

We study the binding energies of Os on the armchair graphene nanoflakes introduced in Section 2.6: C18, C36 and C90 (the structures are shown in Figure 2.4). We do not fix the adatom over the exact middle of the carbon ring and allow the ionic relaxation of the flake. For each adsorption site the whole flake is energetically optimized utilizing VASP [104–107] DFT code with PBE [75, 99, 100, 108] exchange-correlation (XC) functional and DFT-D2 [88] dispersion correction. The resulting structures are used in the subsequent DFT calculations using TURBOMOLE code.

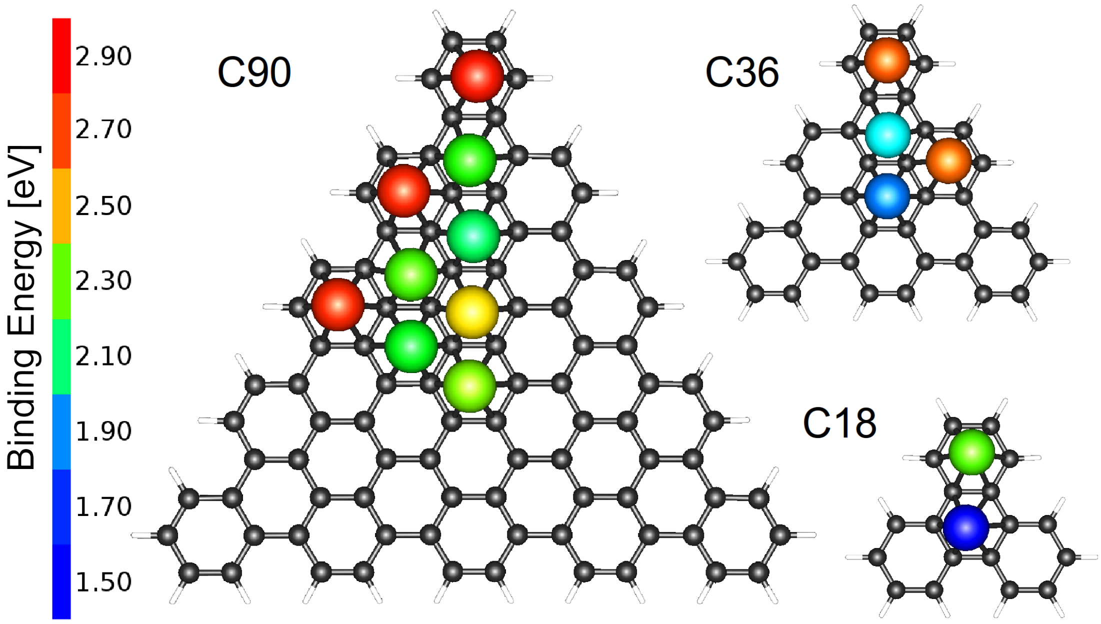

Figure 5.1: *Binding energy of a single Os atom as a function of the adsorption site on graphene armchair nanoflakes C18, C36 and C90. The total energy of Os at* 99 Å *distance from the corresponding nanoflake was used as the reference. Calculations were done using the BP86 exchange-correlation functional with the def2-TZVP-2c basis set.* ***Apex*** *is the most binding site for all flakes, regardless the size. The binding energies vary between* 1.5 *and* 2.9 eV.

As in the Ru study, the binding energy E_b is defined as

$$E_b = E(99\ \text{Å}) - min(E(z)) \tag{5.1}$$

and is positive for the binding case. The BP86 [76, 77, 81, 99, 100] XC functional with dhf-TZVP-2c [109] basis set is used to calculate E_b. Calculated E_b values for Os adatom are shown in Figure 5.1. The trends of the binding energy as function of the flake size and of the position of the adsorption site relative to the flake edge are similar to Ru:

- E_b grows with the flake size;
- E_b is significantly higher at the edge;
- the most preferable adsorption site is **Apex**.

Similar to Ru, the highest E_b among the off-edge sites on C90 is at the site **8** (as defined in Figure 2.4).

The calculations of the binding energy of other 5d TMs (see Table 5.1) show that the most energetically preferable adsorption site is **Apex** as well. The total energies of other 5d TM atoms were only compared between the sites, but not with $E(99\ \text{Å})$. For this reason no absolute binding energies are listed for the rest of 5d TM series. Calculations of the adsorption energy profiles show that 5d TM atoms exhibit a similar structural bistability as we reported in Section 4.2 for Ru. We carefully investigate the details of the bistability in Section 5.3, but first we analyze the magnetic anisotropy of 5d TM atoms and its applicability for single molecule magnets to

Element	Hf	Ta	W	Re	Os	Ir
Site	E_{tot}[eV]					
C36						
1(**Apex**)	0.00	0.00	0.00	0.00	0.00	0.00
2(**Center**)	-1.03	-1.13	-0.95	-0.62	-0.80	-0.53
3(**Edge**)	-0.26	-0.26	-0.26	-0.23	-0.05	-0.07
4	-0.77	-1.02	-0.98	-0.65	-0.64	-0.45
C90						
1(**Apex**)	0.00	0.00	0.00	0.00	0.00	0.00
2(**Center**)	-0.72	-0.80	-1.04	-1.05	-0.52	-0.26
3(**Edge**)	-0.19	-0.27	-0.25	-0.23	-0.08	0.00

Table 5.1: *Relative binding energies of 5d transition metal atoms onto symmetry non-equivalent sites of C36 and C90 graphene flakes. The given number is the total energy difference between the most stable site (which is* ***Apex*** *for all cases) of the corresponding flake for the corresponding element and the current site. Negative values indicate weaker binding. The off-edge sites provide significantly weaker binding compared to* ***Apex*** *and* ***Edge****.*

motivate further investigations of the bistability.

5.2 Magnetic Anisotropy

5.2.1 Osmium

The magnetic anisotropy of osmium on armchair nanoflakes is calculated using BP86 XC functional with the two-component basis set dhf-TZVP-2c. Similar to Ru, the magnetic moment of Os decreases upon the adsorption on the non-magnetic armchair flakes. From $4\,\mu_B$ in the atomic state it is reduced to $2\,\mu_B$ (total magnetization of the decorated flake) in the adsorbed state, but is not quenched completely. The anisotropy values E_{IOP} and E_{IP} are shown in Figure 5.2 and Figure 5.3 respectively.

A trend of the in- vs. out-of-plane anisotropy E_{IOP} as a function of the distance of the adsorption site from the flake edge is not visible. On C90 high E_{IOP} values are calculated both at **Apex** (22.7 meV) and at the off-edge sites **8** (23.1 meV) and **9** (22.8 meV). The lowest values are provided by **Edge** (15.0 meV) and by the off-edge site **4** (13.8 meV). On C36, E_{IOP} reaches its highest values of 31.4 meV and 31.2 meV at **Apex** and **Center** respectively, while the values of **Edge** and the site **4** are significantly lower: 17.4 meV and 19.4 meV respectively. On the C18 flake the E_{IOP} values are 24.4 meV and 8.4 meV for **Apex** and **Center** respectively. Os on C6 shows an extraordinary high value of $E_{IOP} = 75.1$ meV (not shown in Figure 5.2 to keep the color scale appropriate for all flakes).

Regarding the influence of the flake size, the highest E_{IOP} among the three flakes is provided by the C36 flake (31.2 meV at **Apex**). The E_{IOP} on C18 reaches the second-best value among the flake at **Apex** (24.4 meV). The lowest E_{IOP} among the three flakes is also found on C18 (8.4 meV, **Center**).

We observe that **Apex** provides generally high anisotropy values. At the same time, E_{IOP}

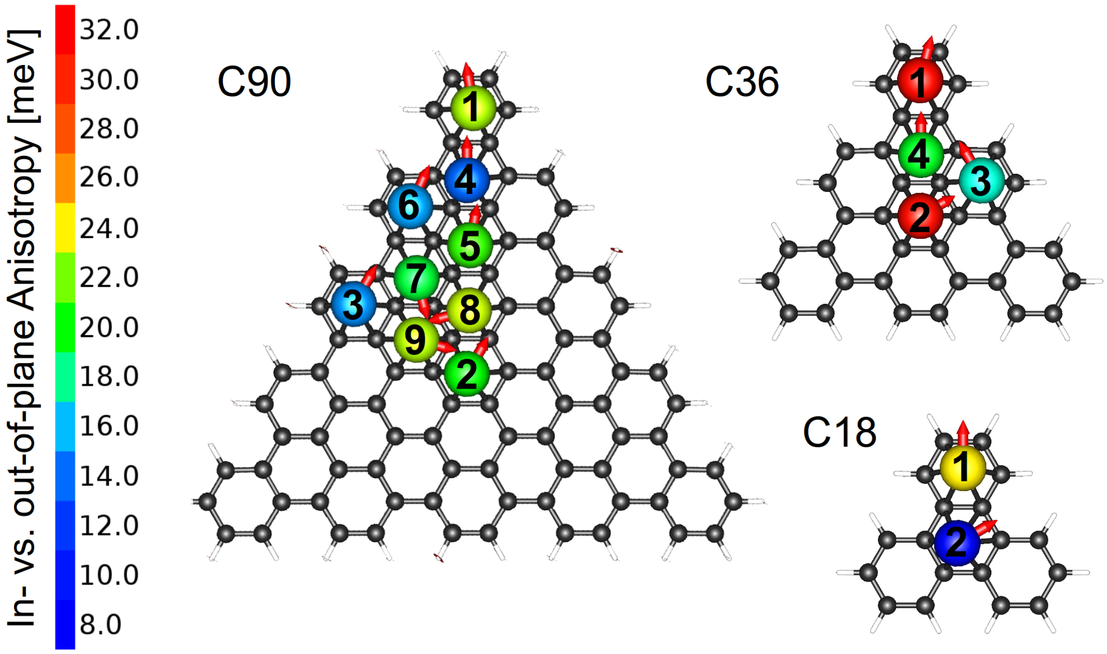

Figure 5.2: *In- vs. out-of-plane anisotropy energy E_{IOP} of a single Os atom on different adsorption sites of armchair graphene nanoflakes C18, C36 and C90. The highest E_{IOP} values are provided by the C36 flake. For the sake of clarity, the site labels introduced in Figure 2.4 are shown here again.*

on the sites closest to the apex is one of the lowest on the whole flake, regardless the flake size. To make further statements about the dependence of E_{IOP} on the position relative to the edge, investigations on other flake sizes have to be done, which are not within the scope of this work.

The E_{IOP} is positive on all adsorption sites and therefore indicates that the preferred magnetization direction is parallel to the flake plane. Due to lower symmetry of the flake compared to infinite graphene, the magnetization directions in plane are not degenerate, and may exhibit an easy axis. Figure 5.3 shows the calculated in-plane directions and the in-plane anisotropy E_{IP} for Os on C18, C36 and C90.

We see that regardless the choice of the flake, **Apex** provides the highest E_{IP}. At the same time E_{IP} varies with the flake size, but no trend is visible within the set of flakes investigated here: the highest value of 11.1 meV is achieved on the C18 flake (**Apex**), followed by 8.2 meV on the C90 flake (**Apex**), while the lowest **Apex** value is found on the C36 flake (6.3 meV). On the non-apex sites the pinning of the easy axis is significantly lower compared to **Apex**, except for the site **4** on the C36 flake (6.1 meV) and the site **9** on the C90 flake (3.0 meV). We note that in contrast to Ru, the preferred anisotropy direction for edge sites is parallel to the triangle edge, which is possibly the consequence of the ionic relaxation of the system. The in-plane anisotropy of 1.6 meV at **Center** of C18 indicates that the magnetic moment of Os atom preferably points towards the C-C bridge. This is different for C6, where the total energy is 0.2 meV lower when the magnetic moment of the Os atom points towards a C atom, compared to the energy when the magnetic moment points towards a C-C bridge.

In general, the in-plane magnetic anisotropy of Os is about two orders of magnitude higher than of Ru. The significantly higher E_{IOP} and E_{IP} values compared to the values calculated for Ru

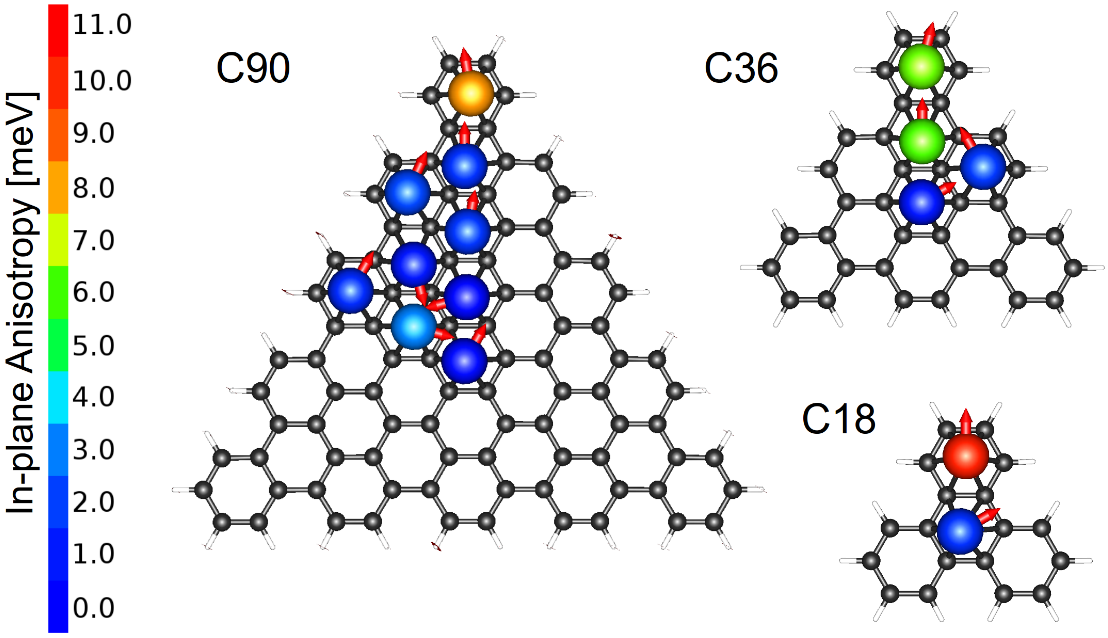

Figure 5.3: *In-plane anisotropy energy E_{IP} of a single Os atom on different adsorption sites of armchair graphene nanoflakes C18, C36 and C90. The red arrows indicate the calculated preferred magnetization axis at each site. The strongest pinning of the magnetic moment is achieved on the Apex of the C18 flake.*

magnetic center confirm our expectations about the 5d TM elements, and motivate for further investigations of the whole 5d TM series.

5.2.2 Other 5d Transition Metals

The anisotropy values are calculated for the series of 5d transition metal atoms from Hf to Ir on the three sites of high symmetry on the C90 armchair flake: **Apex**, **Center** and **Edge**. Calculations of Pt show zero magnetic moment, and any further investigations of Pt are stopped at this point. The Table 5.2 shows the calculated magnetic anisotropies. The angle α_{apex} is the angle between the preferred magnetization axis on **Apex** and the bisecting line of the corresponding angle of the triangle. Zero α_{apex} means that preferred magnetization axis points away (or, equally, towards) the center, i.e. along the bisector. Our findings show that α_{apex} varies from element to element.

Hf provides the lowest anisotropy values for both E_{IOP} (between 2.0 meV and 2.9 meV) and E_{IP} (up to 1.4 meV). The anisotropy values and trends of Ta are similar to Os: E_{IOP} ranges from 12.5 to 17.6 meV and E_{IP} is up to 5.2 meV. The anisotropy energies is even lower for W: E_{IOP} ranges between 1.6 meV on the **Center** site and 11.4 meV and 11.5 meV on **Apex** and **Edge** respectively, while E_{IP} goes up to only 2.7 meV. The E_{IOP} of Re is strongly negative (-33.7 meV) on **Center** indicating preferable out-of-plane magnetization, weakly negative (-0.6 meV) on **Apex**, and weakly positive (1.9 meV) on **Edge**, where the in-plane anisotropy is 4.0 meV.

Ir also provides negative E_{IOP} on **Center** (-7.0 meV), but the positive value on **Apex** is much stronger (17.3 meV) than for Re. The E_{IP} reaches for Ir the highest values among the investigated 5d TMs with 16.4 meV on **Apex** and 11.3 meV on **Edge**. Comparable E_{IOP} and E_{IP} values on **Apex** indicate that the preferred magnetization direction (which is in-plane and perpendicular to the triangle bisector) is comparably stable with respect to the least preferable in-plane direction (along the triangle bisector) and with respect to the out-of-plane direction. The two latter directions span a hard plane perpendicular to the preferable magnetization direction, which is the easy axis. The hard plane is perpendicular to the flake plane and cuts the flake through the center.

Element	Hf	Ta	W	Re	Os	Ir
E_{IOP}						
$E_{IOP,Apex}$[meV]	2.1	16.7	11.4	-0.6	22.9	17.3
$E_{IOP,Center}$[meV]	2.9	17.6	1.6	-33.7	20.0	-7.0
$E_{IOP,Edge}$[meV]	2.0	12.5	11.5	1.9	15.0	4.9
E_{IP}						
$E_{IP,Apex}$[meV]	0.1	5.2	2.0	5.4*	9.6	16.4
$E_{IP,Center}$[meV]	1.4	5.2	1.0	2.0*	0.4	0.3*
$E_{IP,Edge}$[meV]	0.4	3.8	2.7	4.0	1.5	11.3
α_{apex}[°]	0	90	90	0*	0	90

Table 5.2: *Magnetic anisotropy energies E_{IOP} and E_{IP} for 5d transition metal atoms from Hf to Ir adsorbed onto three high-symmetry sites (**Apex**, **Center** and **Edge**) of C90 nanoflake. The last row contains the angle α_{apex} between the preferred magnetization direction on **Apex** and the triangle bisector. The highest E_{IOP} with preferred in-plane magnetization is provided by Os, Ir and Ta sitting on **Apex**. Re on **Center** shows the strongest anisotropy with preferred out-of-plane magnetization. The strongest in-plane pinning of the magnetization axis is observed for Ir on **Apex**.*
* *value is irrelevant due to negative E_{IOP}, i.e. preferred magnetization direction out of plane.*

Concluding, Os and other 5d TM element atoms used as magnetic centers on the graphene nanoflake substrate show strong magnetic anisotropy, which varies depending on the position of the adsorption site on the flake and on the flake size. In- vs. out-of-plane magnetic anisotropy values of 31.4 meV of Os adatom on the C36 flake and 75.1 meV on benzene molecule, which exceed the thermal energy of the room temperature (25 meV) make it a good candidate for single molecule magnetic switches. As we describe in the Chapter 2, a molecular switch requires a spin crossover effect, i.e. multiple and decoupled magnetic states. The alternation of the spin state upon adsorption, as we report in the Section 5.2.1, from $4\,\mu_B$ to $2\,\mu_B$ is the result of energy level crossing, which may be an indication of the SCO effect. In the next section we investigate this effect carefully.

5.3 Structural Bistability

The magnetic moment of Os atom diminishes upon adsorption onto graphene nanoflakes from $4\,\mu_B$ to $2\,\mu_B$. Considering this transition as an indicator for possible spin-crossover, we carry out a gradual annealing of the adatom towards the flake. For each annealing step we calculate the following electronic and magnetic properties of the system: the total energy, the magnetic moment of the adatom, the charge of the adatom, occupations of the valence atomic orbitals, as well as magnetic anisotropies. This is done on **Center** of C36 flake, since the adatom stays above the middle of the carbon ring on this site due to the C_{3v} symmetry. The flake is assumed as rigid upon the annealing. C36 is preferred to C90 to reduce the computational effort. Furthermore, C36 provides the highest magnetic anisotropy among the investigated nanoflakes, and the effect described below is more pronounced on C36. Smaller structures on the other hand, such as C18, experience a stronger structural change upon annealing (as we show later in Section 5.4.2) and the assumption of flake rigidity would not be as valid as for C36.

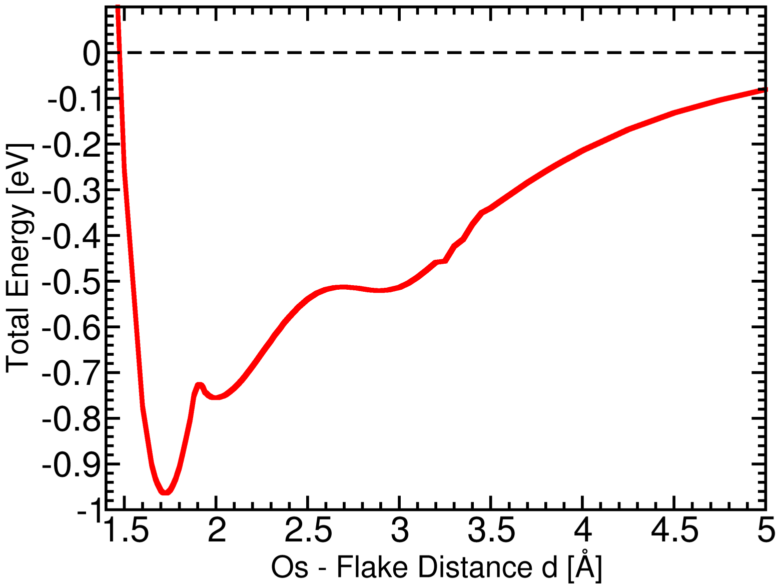

Figure 5.4: *The total energy (relative to the free state) of Os adatom upon vertical annealing to the center site of C36 graphene nanoflake lying in the horizontal plane. The x-axis is the adatom elevation above the flake plane. The DFT calculations are done using the PBE GGA exchange-correlation functional with def2-TZVP basis set and the DFT-D2 dispersion correction. Three metastable positions are clearly distinguishable in the plot.*

The energy profile (Figure 5.4) of the annealing exhibits multiple minima at three different elevations of the Os atom above the flake. Apart from the *first* minimum at 1.72 Å, which is primary, there is also a *second* minimum and 2.0 Å and a *third* minimum at 2.9 Å Os-flake distance. The barrier between the third and the second minimum is 7.9 meV. The barrier between the second and the first minimum is 29.8 meV. Since, to our best knowledge, no such bistability of 5d transition metal adatoms on graphene has been reported before and the height of the barrier is of the order of $k_B T$ of room temperature (29.8 meV = $k_B T$ of T=346K), which makes it interesting beyond only fundamental research, we are encouraged to investigate the three minima more carefully.

5.3.1 Spin-Crossover Effect

The magnetization of the Os adatom is calculated as a function of the distance between Os and the flake plane. Between 1.86 Å and 1.96 Å, the magnetization changes from 2 to 4 unpaired electrons, indicating a spin crossover. The anisotropy calculations show that the preferred magnetization direction also switches upon this transition: the anisotropy E_{IOP} of 33.3 meV at 1.72 Å elevation changes its sign to -36.1 meV at 2.0 Å, and grows to -42.4 meV at 2.9 Å.

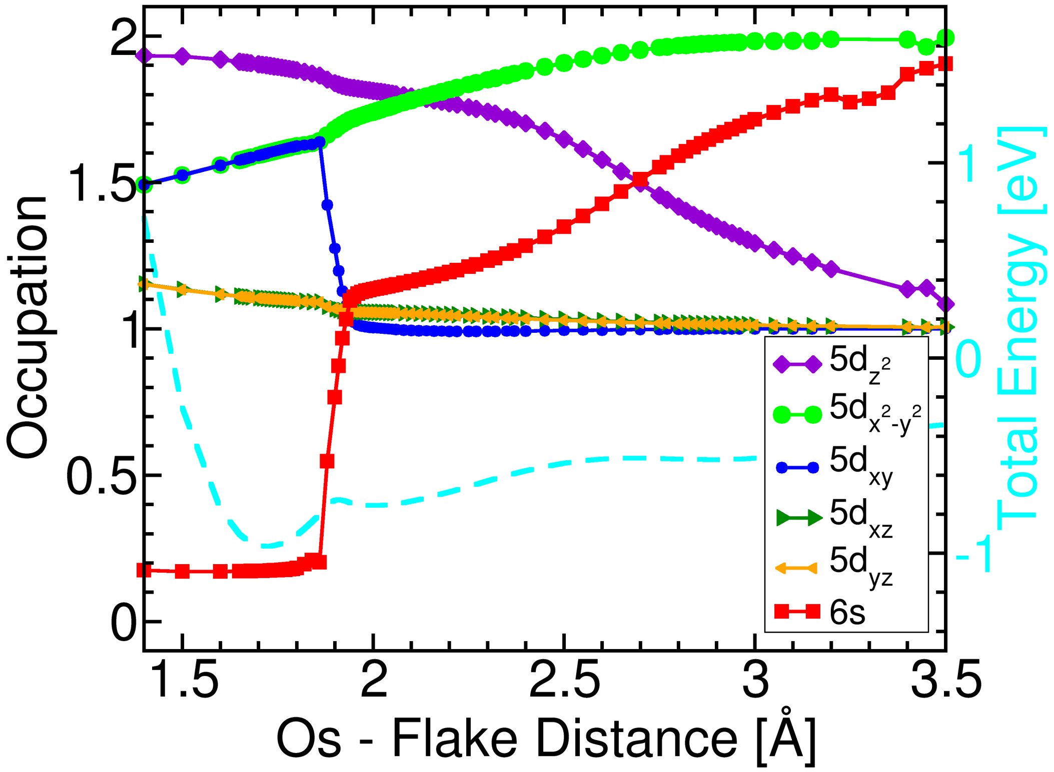

Figure 5.5: *The occupation of the atomic orbitals (AOs) of Os atom as a function of its elevation above* ***Center*** *of the C36 nanoflake. The occupation is calculated by the projection of the Kohn-Sham molecular orbitals on the Os atomic orbitals. The cyan dashed line is the energy profile, indicating the metastable positions as local energetic minima. At* 1.9 Å *one electron is transferred from the almost (due to the hybridization with the flake orbitals) full* $5d_{xy}$ *AO to the empty* $6s$ *AO, resulting in an increase of the total magnetic moment by* $2\,\mu_\mathrm{B}$*. The figure was previously published in [3].*

Orbital Occupation Analysis

To investigate the change of the magnetic properties upon the 1→2 transition, the Kohn-Sham molecular orbitals (MOs) are projected on the atomic orbitals (AOs) of Os atom and the occupation analysis is done for the valence atomic orbitals of Os. The Figure 5.5 shows the occupation of the atomic orbitals as a function of the adatom-flake distance. The dashed line is the corresponding energy profile and indicates the position of the energetic minima.

At the first energetic minimum the $6s$ orbital is almost empty, the orbitals $5d_{xz}$ and $5d_{yz}$ are half-filled (two unpaired electrons), and the orbitals $5d_{z^2}$, $5d_{xy}$ and $5d_{x^2-y^2}$ are fully occupied. Note that the occupation of $5d_{xy}$ and $5d_{x^2-y^2}$ is reduced due to the hybridization and charge transfer between the adatom and the flake. The two unpaired electrons from $5d_{xz}$ and $5d_{yz}$ result in total magnetic moment of $2\,\mu_\mathrm{B}$.

Upon the transition 1→2 the $6s$ orbital gains one electron, which comes mostly from the $5d_{xy}$ orbital. Since the increase in $6s$ occupation is noticeably higher than the decrease in the $5d_{xy}$ occupation, part of the charge must be withdrawn from the flake. This is substantiated by the calculation of the charge transfer between the Os and the flake: the local charge of the adatom changes from $0.495\,\mathrm{e}^+$ at the first minimum to $0.149\,\mathrm{e}^+$ at the second minimum.

The resulting occupation is then: two filled orbitals ($5d_{z^2}$ and $5d_{x^2-y^2}$) and four half-filled orbitals ($6s$ and the rest of $5d$ orbitals). The total magnetic moment of the system at the second minimum is therefore $4\,\mu_\mathrm{B}$. Upon the $2 \rightarrow 3$ transition, the $5d_{z^2}$ and the $6s$ orbital switch places in this formation, but the total magnetic moment remains unchanged.

In the following we call the first minimum the *'d'* minimum, because the only occupied valence orbitals are the $5d$ orbitals there. The second minimum will be referenced as the *'s'* minimum, because here one $6s$ orbital becomes occupied, and the third minimum as the *'vdW'* minimum, because of the weakness of the chemical bonding, indicating that van der Waals interaction is responsible for the binding at this distance.

Molecular Orbital Analysis

To understand the reason for the abrupt occupation change of the $6s$ orbital of Os, we analyze the molecular orbitals close to the HOMO (highest occupied molecular orbital) by extracting their energies and the contributions from the atomic-type functions (s-, p-, d-, f-functions) located at the Os atom and at the flake.

Figure 5.6 shows the energies (y-axis) of the molecular orbitals (MO), the contribution of the corresponding atomic orbital (AO) type (dot thickness) and the type (in case of d orbitals: the most pronounced type) of the atomic orbital (dot color) as a function of distance (x-axis). The distances, at which the energetic minima are found, are indicated by the dashed line. Spin-up, or majority (α), and spin-down, or minority(β), orbitals are depicted separately. The unoccupied orbitals are those at and above the LUMO (lowest unoccupied molecular orbital) line.

Both majority (α) and minority (β) $6s$-orbitals are empty at the 'd' minimum (Figure 5.6c), but upon the 'd'→'s' transition $6s\alpha$ crosses the $5d_{xy}\beta$ (Figure 5.6b) orbital, so that $5d_{xy}\beta$ is unoccupied at the 's' minimum, while $6s\alpha$ is occupied. Since one electron jumps from the minority to the majority channel, the total magnetic moment of the system increases: A spin transition takes place.

Further towards the 'vdW' minimum, one of the occupied MOs loses its $5d_{z^2}\beta$ character (the dots become smaller), while an unoccupied one gains it (both are visible in Figure 5.6b). These two MOs are also recognizable in Figure 5.6c, where the unoccupied orbital looses the $6s\beta$ character upon 's'→'vdW' transition, while the occupied one gains it. In such a manner one electron changes from the $5d_{z^2}\beta$ to the $6s\beta$ orbital, restoring the atomic orbital occupation of Os: $5d^6 6s^2$. Since the electron stays in the minority channel, the total magnetic moment of the system is maintained upon the 's'→'vdW' transition: no spin transition takes place.

The possible reason for the destabilization of the $6s$ orbitals, and therefore increase in energy close to the flake, is that the s orbitals are not hybridizing well with the π-cloud of the flake. This leads to a strong Coulomb repulsion between them, making the $6s$ orbitals less favorable at close distances than the $5d$ orbitals, which hybridize well with the flake orbitals.

The hybridization can be seen in Figure 5.6. Large (small) dots in (a) and (b) indicate that the particular atomic orbital contributes significantly (insignificantly) to the particular molecular orbital. Medium-sized dots indicate a hybridization, meaning that some other AO (s orbital of Os, or p orbitals from C) also contributes to this MO to the similar extent. In this case there will be a dot at the same coordinates in one of the other plots: in (c), if the second contribution comes from $6s$ AO, or in (d), if the second contribution comes from the p AO located on the flake. At the 'd' minimum the $6s\alpha$ and $6s\beta$ orbitals are not hybridized at all, as well as the both $5d_{z^2}$ orbitals (large dots), while the other MOs with $5d$ character are strongly hybridized with the flake orbitals (medium dots in Figure 5.6a/b and d). Upon 's'→'vdW' transition the $6s\beta$ orbital mixes with the $5d_{z^2}\beta$ (medium dots at the same energy in (c) and (b)), but is clearly absent in the d) plot, meaning that it still does not hybridize with the flake orbitals. Farther from the flake, the Coulomb repulsion between the electrons in the Os $6s$ orbital and the flake π-cloud decreases, restoring the natural orbital order of atomic Os and the flake.

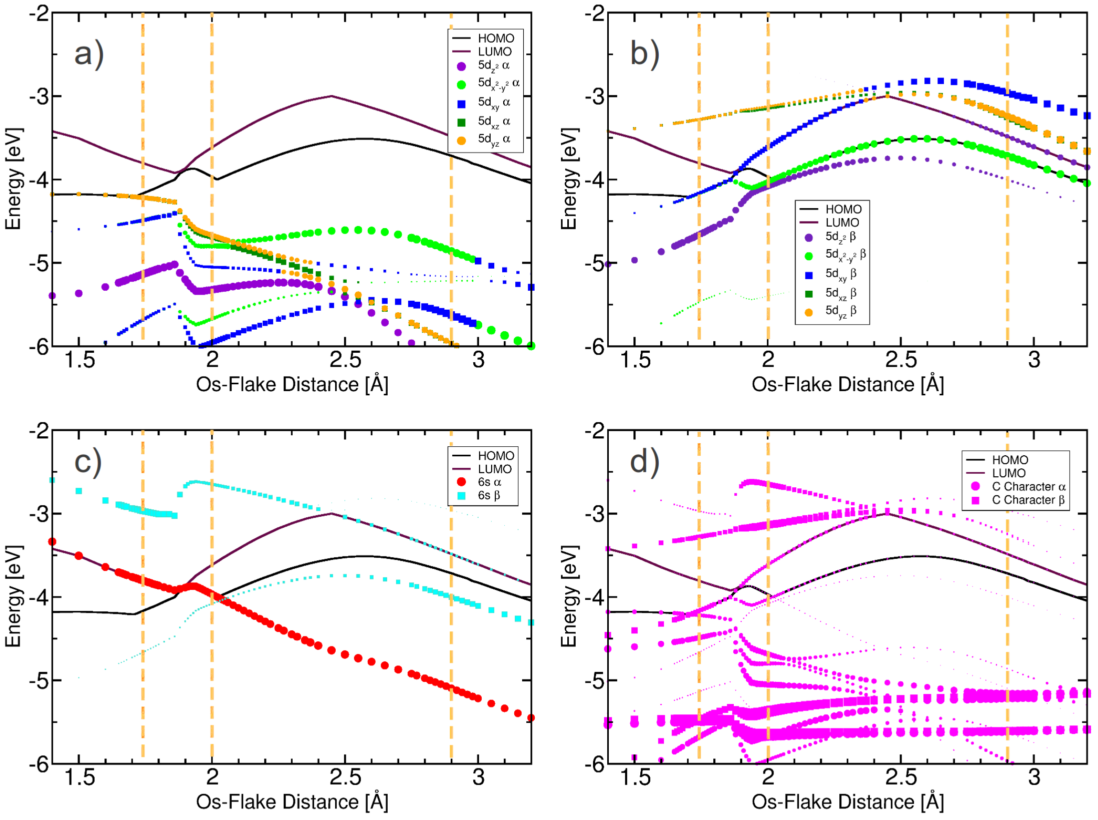

Figure 5.6: *The energies of the Kohn-Sham molecular orbitals (MOs) of Os over the center site of C36 nanoflake as a function of the vertical Os - flake distance. The dot thickness indicates the contribution of the following atomic orbitals (AOs) to the corresponding MO: d type AOs located at the Os atom (a and b), s type AOs located at the Os atom (c), and AOs located not at Os (d). For the purpose of clarity, the d contributions are plotted separately for the majority (α) MOs (a) and for the minority (β) MOs(b). Note: each plot shows all the MOs within the energy range, but they may be not visible if the corresponding contribution is near zero. The color coding in the (a) and (b) plots represents the $5d$ AOs, which are closest in shape to the corresponding MO, evaluated visually from the 3D plots of the MOs. The dashed vertical lines indicate the position of the three metastable distances of Os above the flake. The level-crossing between the $6s\alpha$ MO and the $5d_{xy}\beta$ MO is clearly visible around 1.9 Å. The figure was previously published in [3].*

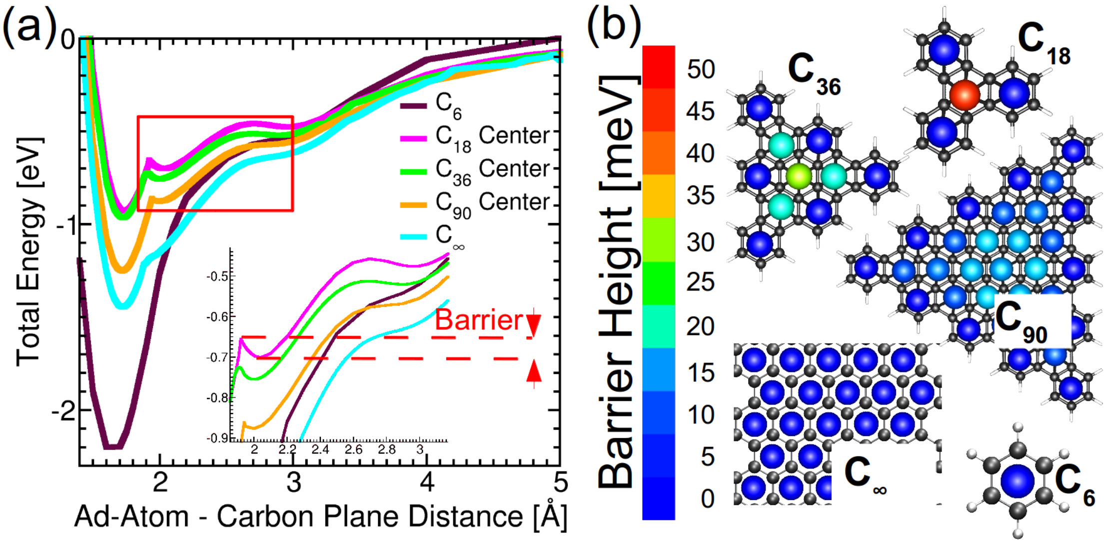

Figure 5.7: *(a) The energy profiles of Os annealing to the Center site of graphene nanoflakes C18, C36 and C90, as well as to a benzene molecule (C6) and a carbon ring in an infinite graphene sheet (C∞). The inset shows a zoomed in region marked with a red box in the main figure, emphasizing multiple energy minima upon annealing. In the inset a barrier between the minima at ≈2.0 Å ('s' minimum) and at ≈1.7 Å ('d' minimum) is defined as the difference between the energy of the 's' minimum and the energy at the peak between the 's' and 'd' minima. The barrier defined in (a) for Os at all sites of the considered nanoflakes is shown in (b). The barrier vanishes at the flake edge, as well as on C6 and C∞.*

5.3.2 Flake Size Impact

Since our findings do not include anything that is specific for the C36 flake, it is reasonable to assume similar behavior for other flakes, and on graphene in general. To test this, we calculate the energy profiles on C6, C18, C90, and, using VASP DFT code [104–107], which utilizes periodic boundary conditions, also on infinite graphene sheet C∞. Figure 5.7a shows the profiles on **Center** of the corresponding flakes, as well as on C6 and C∞. The bistability was clearly visible on the flakes, while on C6 and C∞ the profiles show only shoulders at the positions of otherwise secondary minima and do not feature a barrier. The anisotropy measurement of Os at 3 Å elevation above C6 show that a massive anisotropy switching takes place here also, but the bistability profile is missing. The global minimum 'd' is so deep and wide, that it absorbs the 's' minimum and flattens the 'vdW' minimum.

To characterize the bistability quantitatively, the barrier for the transition 's'→'d' is evaluated, as shown in the inset of Figure 5.7a. Figure 5.7b shows the barrier heights for adsorption on all sites (annealing above the middle of the corresponding carbon ring) of carbon structures C6 - C∞. Apart from C6 and C∞ the barrier also vanishes at the edge sites of the graphene flakes, which are, as showed before, more energetically preferable, i.e. have a deeper 'd' minimum. At the off-edge sites the barrier decreases with the increasing size of the flake, accompanied by a stronger binding energy, as was mentioned in Section 5.1. The highest barrier among the investigated structures is found to be 45 meV on **Center** of the C18 flake and is higher than the thermal energy at the room temperature (25.6 meV).

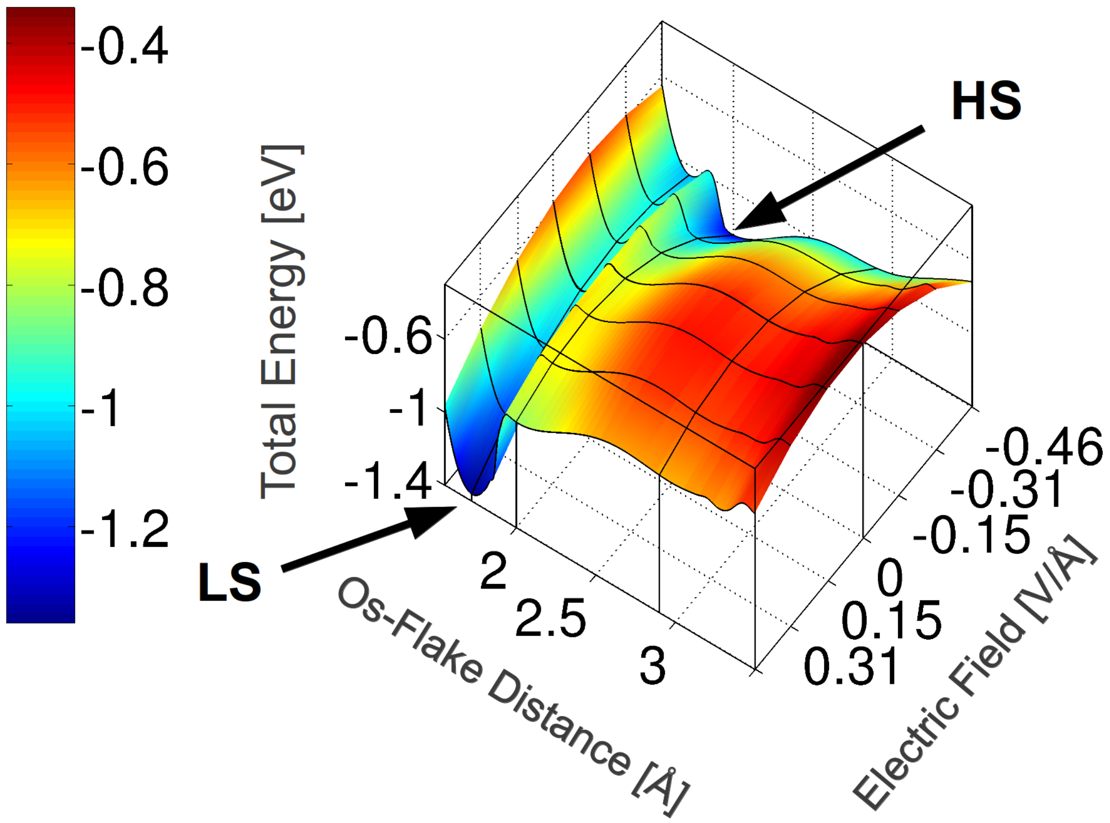

Figure 5.8: *The total energy profiles of an Os adatom upon annealing to the center site of C36 nanoflake, as a function of the Os - flake distance and the external electric field applied perpendicular to the flake plane. At high negative electric field, the 'd' energetic minimum (indicated as low spin, LS valley) becomes less energetically preferably than the 's' minimum (high spin, HS valley). The barrier between the valleys restrict the switching in absence of the external field. The figure was previously published in [3].*

5.3.3 Control by Mean of an External Electric Field

The bistability of Os adatom on graphene nanoflake accompanied by a strong anisotropy change mentioned in Section 5.3.1 makes this structure an attractive candidate for a single molecule switch, presuming that there is a way to switch between the metastable states. Since the first two energetic minima come from the interplay of two electronic states – the atomic $5d^6 6s^2$ state of Os and the adsorbed state $5d^8 6s^0$ with $5d$ orbitals strongly hybridized with the flake – the way to switch between the two states would be to stabilize or destabilize one of them. An external electric field applied perpendicular to the flake plane can for instance reduce the hybridization by moving the electron cloud from the flake towards the Os atom. Figure 5.8 shows this behavior for sufficiently high negative electric field applied perpendicular to the flake plane. The 'd' minimum becomes higher in energy than the 's' minimum, so that the latter becomes the global minimum. In order to reach this minimum the system has to overcome a barrier of about 44.5 meV (at the field of -0.46 V/Å), e.g. by external light impulse, or thermal phonons. Switching the electric field off would keep the system in the state 2, as long as the barrier 2→1 is not overcome. Switching back to 1 can occur by interaction with phonons at room temperature, or by positive electric field, which would reduce the 2→1 barrier. Figure 5.9

shows that the positive charge of Os is actually reduced by a negative electric field, making the S=2 state more preferable. Since the influence of the electric field is independent on the flake parameters, we expect a similar behavior on all graphene structures mentioned in this study. The dependence of the barrier height on the flake size, shape and site allows to tune the parameters of the molecular switch.

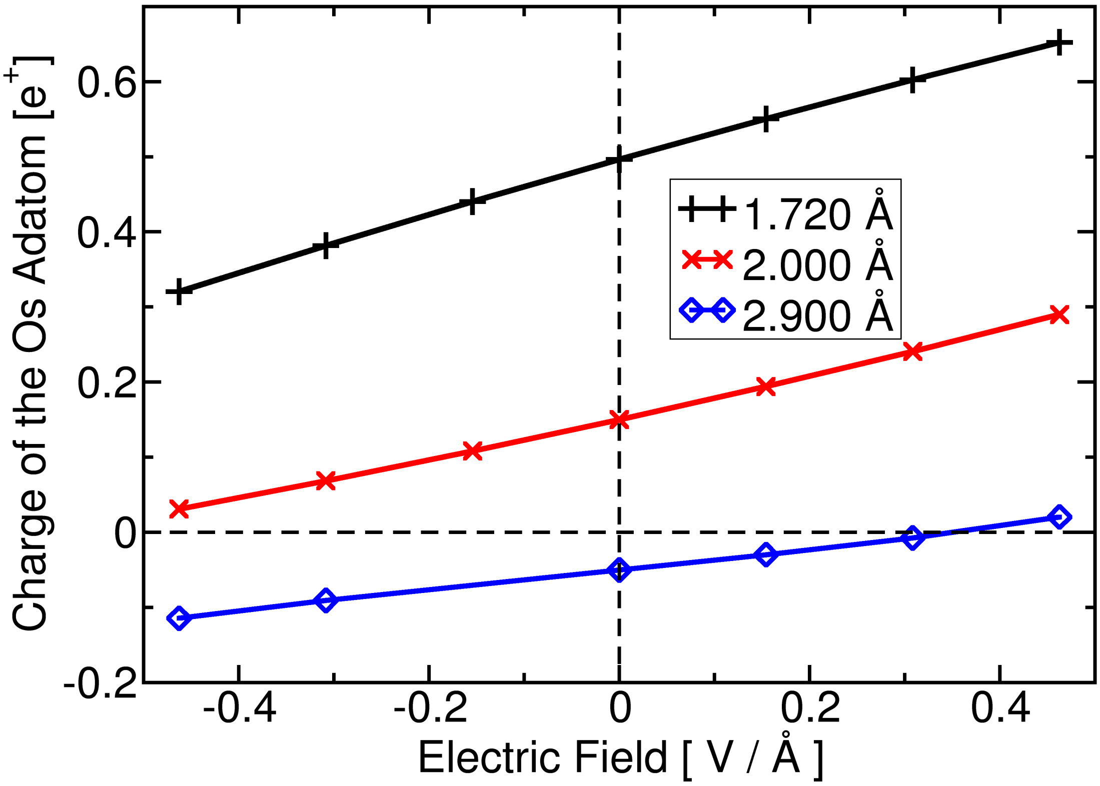

Figure 5.9: *The charge transfer between the Os adatom and the C36 nanoflake at three different metastable adatom-flake-distances above the center site of the flake as a function of an external electric field applied perpendicular to the flake plane. Negative electric field pushes the negative charge from the flake to the adatom, decreasing the charge transfer at the 'd' (black) and 's' (red) positions. The calculations were done using PBE exchange-correlation functional with def2-TZVP basis set. The figure was previously published in [3].*

5.3.4 Other 5d Transition Metals

The energy profiles of Os shown in the previous subsection are only bistable if Os is not placed on the flake edge. However, the **Apex** was found as the most stable site. For that reason we also calculate the energy profiles on **Apex**, while investigating the bistability on the rest of the 5d TM series.

Using the BP86 functional and the def2-SVP basis set to reduce the computational effort, we calculated the adsorption profiles for other 5d transition metals (Hf to Ir) on the C36 flake. Figure 5.10 demonstrates the energy profiles and the absolute values of the magnetic moment of the corresponding adatom as a function of adatom-flake distance while annealing to the sites **Center** (a) and **Apex** (b). The calculations show that each of the investigated adatoms undergo a spin transition upon annealing to the flake: the magnetic moment is reduced close to the

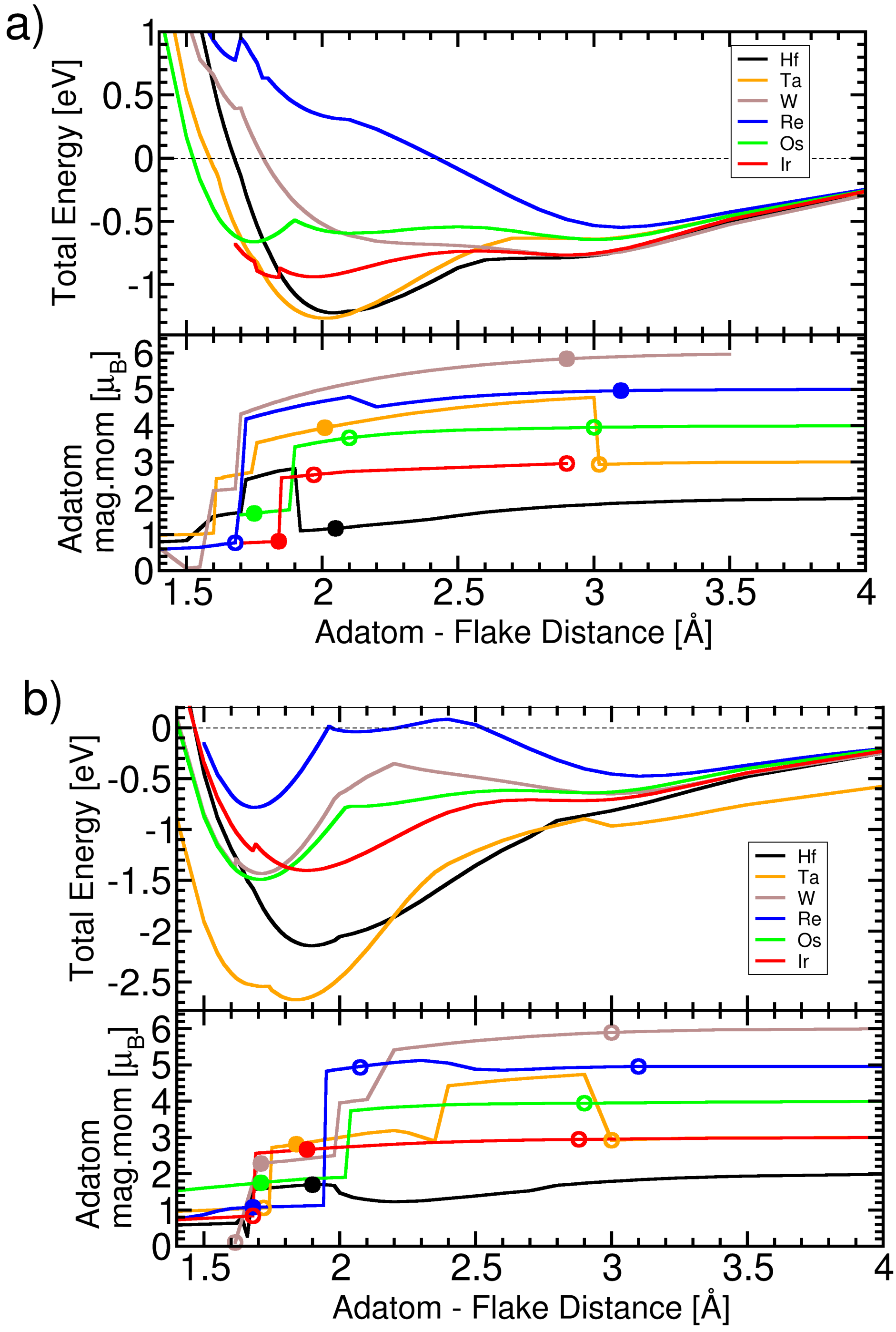

Figure 5.10: *The total energy (upper half of a) and b) respectively) and the magnetic moment (lower half) of 5d transition metal (TM) adatoms as a function of the adatom z-position, while annealing to* ***Center*** *(a) and* ***Apex*** *(b) of the C36 nanoflake lying in the x-y plane. The circles in the lower part indicate the position of the local energy minima shown in the upper part. The filled circles indicate the global energy minimum of the particular energy profile. Most of the energy profiles show a structural bistability, demonstrating the generality of the spin crossover effect for the 5d TMs on graphene nanoflakes. For all 5d TMs, the magnetic moment decreases closer to the flake.*

flake.

We first analyze the annealing to the center site (Figure 5.10a). The low spin (LS) state is only stable for Os and Hf (which demonstrates only one energy minimum). For Ir, the first

(LS) and the second (high spin, HS) minima are almost equal in energy and very close to each other in space (0.12 Å). The barrier between them is only 7 meV. The LS state as a metastable minimum is only present for Re, but is non-binding. Remarkably, below certain distance to the flake, Ta (natural state S=1.5, $5d^36s^2$) switches to HS state (S=2.5, $5d^46s^1$), and keeps it in the global minimum of its energy profile, while the magnetic moment is reduced again closer to the flake.

The 'vdW' minimum is present for all elements except for Hf and is the global minimum for Re and W. Since the def2-SVP basis underestimates the binding energy of the 's' and 'd' minimum (see Figure 5.11), we expect a secondary, 's', minimum for W with the same magnetic state as the 'v' minimum. As this bistability does not contain a spin transition, we leave this question open for future investigations and focus on Os.

At **Apex** (Figure 5.10b), the energy profiles of the investigated 5d elements also exhibit a bistability, while the 'vdW' minimum is less pronounced. The LS state is stable for W, Re and Os, while the HS state is stable for Hf, Ta and Ir. Such variation of the magnetic properties combined with the bistability allows to tune the properties of the single molecule magnetic switch in a wide range.

5.4 Robustness of the Results Against the Intrinsic Calculation Parameters

5.4.1 Bistability

In order to prove the existence of structural, accompanied by magnetic, bistability of Os on graphene nanoflakes, we calculate the energy profiles using different methods and test them with respect to the calculation parameters: the size of the basis set, the exchange-correlation functional, the method (Hartree-Fock with Møller-Plesset correction of the second order, MP2), and the van der Waals interaction correction.

Size of the Basis Set

In the DFT calculations the charge density is expressed by sets of basis functions. The precision of the density representation directly depends on the size of basis set, i.e. on the number of basis functions. Too small basis sets may cause imprecise results of the whole calculation. Large basis sets, on the other hand, lead to increased simulation times, so that at certain basis set size handling of even small systems requires substantial calculation times.

To estimate the influence of the basis set on the energy profiles and the binding energies, we calculate the energy profiles using three basis sets: def2-SVP [110, 111] (the smallest), def2-TZVP [111, 112], and def2-QZVP [113] (the largest). Since we are only interested in the difference between the basis sets, we choose the smallest flake (C18) to perform the test. The energy profiles are shown in Figure 5.11. To take the van der Waals interaction into account, the basis set-independent DFT-D2 [88] correction is added to the total energies. The energy profiles exhibit three minima, regardless the choice of the basis set. The binding energies of the 'd' and the 's' minima provided by the def2-SVP are $0.25\,\mathrm{eV}$ and $0.20\,\mathrm{eV}$ lower (i.e. weaker binding) than those provided by the def2-TZVP and def2-QZVP basis sets.

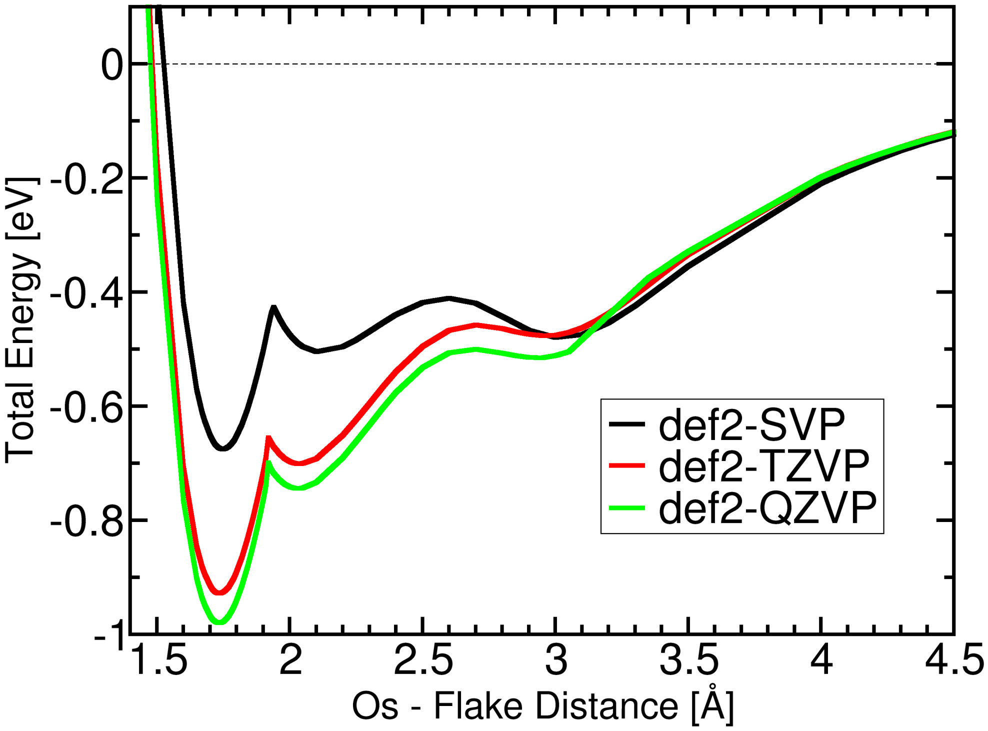

Figure 5.11: *The total energy profiles of Os annealing onto the C18 graphene nanoflake calculated using three different basis sets and the PBE exchange-correlation functional. Additionally, dispersion correction DFT-D2 [88] was applied. The basis sets are labeled as implemented in TURBOMOLE [82]. The smallest basis set def2-SVP provides a different binding energy closer to the flake, while the overall trends, such as bistability and barrier height, remain unchanged by the choice of the basis set.*

Transition	1→2	2→1	2→3	3→2
Basis set	Barrier height [eV]			
def2-SVP	0.249	0.079	0.094	0.069
def2-TZVP	0.273	0.046	0.243	0.019
def2-QZVP	0.281	0.045	0.244	0.015

Table 5.3: *Energetic barriers for the transitions between the metastable Os-flake-distances on the* ***Center*** *site of C18, calculated using the PBE exchange-correlation functional, DFT-D2 dispersion correction and three different basis sets. The def2-TZVP and def2-QZVP basis sets produce similar values, while def2-SVP underestimates the 2→3 barrier, as a consequence of the underestimated binding energy.*

For qualitative comparison, the energetic barrier height for the three basis sets is shown in Table 5.3. The barriers calculated with def2-TZVP and def2-QZVP are almost the same. The barriers provided by the def2-SVP differ from the others by a factor of up to 3, depending on the position and the direction of the transition. Therefore we conclude that for our calculations the def2-TZVP basis set provides enough precision to be used throughout the study, instead of the time-costly def2-QZVP basis set, or the imprecise def2-SVP basis set.

Compared to the def2-TZVP, the def2-SVP basis set provides a weaker binding for the first and

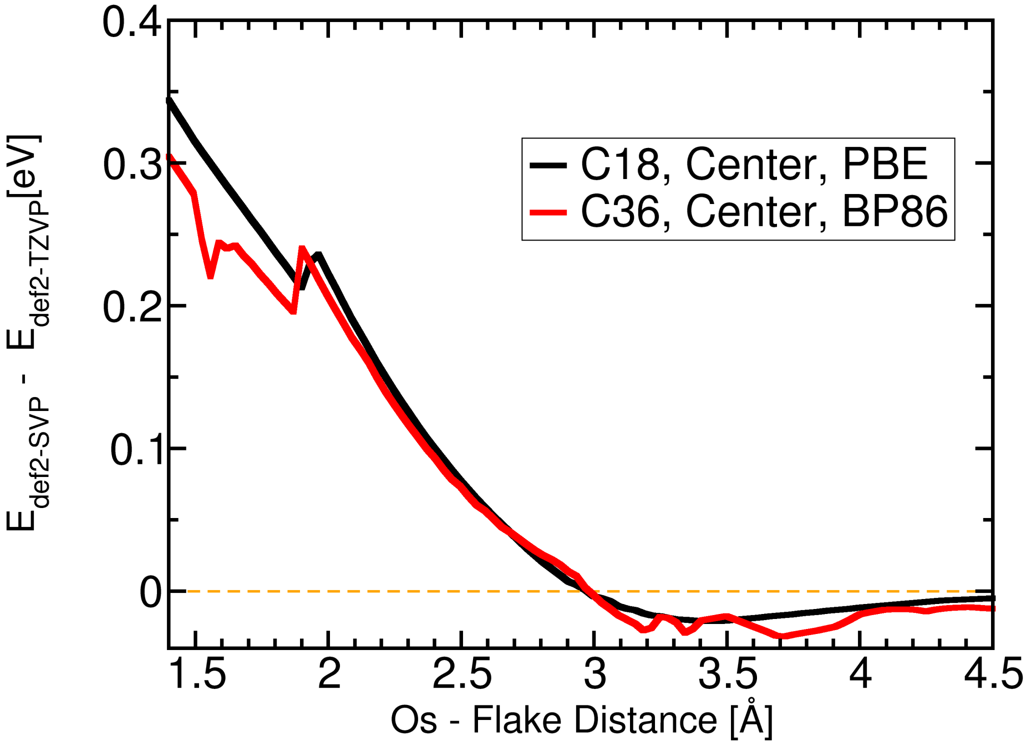

Figure 5.12: *The difference between the total energies calculated with def2-SVP and def2-TZVP basis sets as a function of distance between the Os adatom and the center site of the graphene nanoflake. The difference appears to be independent from the nanoflake (C18 or C36), and from the exchange-correlation functional (PBE and BP86), and therefore can be used to estimate the error (assuming that def2-TZVP produces the more realistic energies) in the energy profiles calculated with the def2-SVP basis set.*

the second energetic minima: by 0.25 and 0.20 eV respectively on the C18 flake, and by 0.23 and 0.19 eV respectively on the C36 flake, as additional tests show (def2-QZVP is not tested on C36). The binding energies at the 'vdW' minimum change insignificantly with the size of the set. We calculate the difference between the def2-SVP and def2-TZVP energy profiles as a function of Os-flake distance (see Figure 5.12). Since this difference is similar for both flake sizes and both XC functionals, it allows us to estimate the "true" (e.g. calculated with def2-TZVP basis set) binding energies based on the preliminary def2-SVP results.

Dispersion Correction

The van der Waals (vdW) interaction is a problematic issue in the density functional theory, because the local exchange-correlation (LDA and GGA), being the most popular exchange-correlation functionals type, do not include this long range dynamic correlation. Since in our case the vdW interaction is responsible for the third energetic minimum, it is essential to find a way to take it into account. One of the popular methods is the semi-empirical DFT-D [86] correction, which was improved by Stephan Grimme to DFT-D2 [88] and later to DFT-D3 [114]. For that reason we call the DFT-D corrections the Grimme corrections.

To investigate the influence of the semiempirical approach, we calculate the energy profiles using 1) no vdW correction, 2) DFT-D2 method and 3) DFT-D3 method, with two GGA functionals

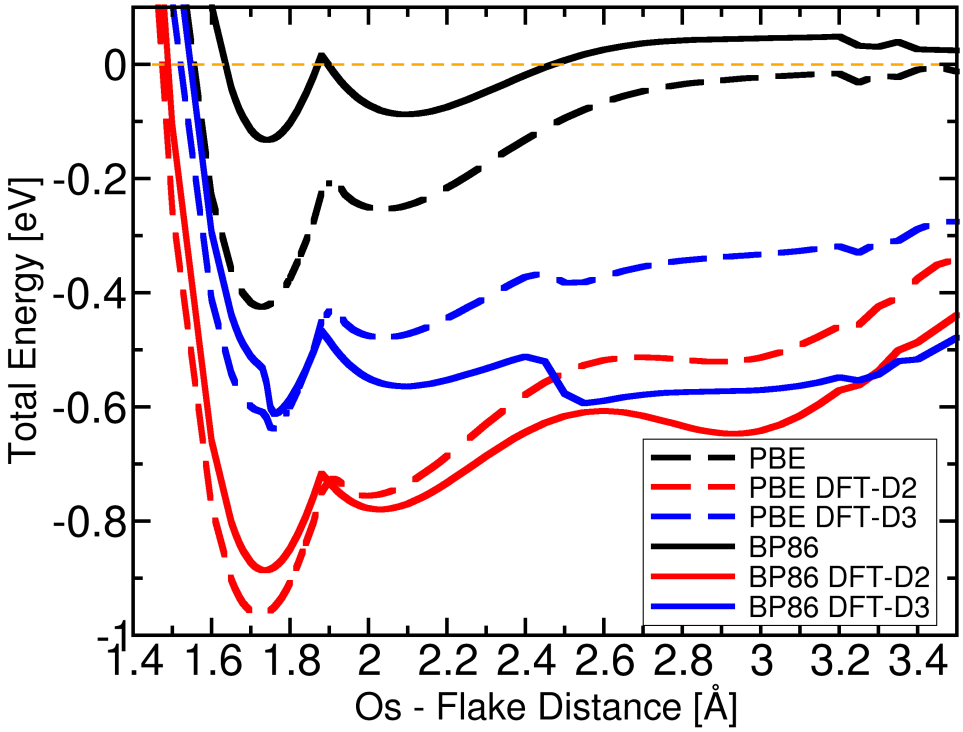

Figure 5.13: *Energy profiles for Os annealing to the C36 flake (center site), calculated with two different GGA functionals – PBE (dashed lines) and BP86 (full lines), without correction to take the van der Waals interaction into account (black curves), as well as using two types of semi-empirical vdW corrections: DFT-D2 (red) and DFT-D3 (blue). The total energy of the system with a large (9 Å) Os-flake separation was subtracted from the total energy at each point, so that the resulting plots show negative binding energies. See the text for the detailed analysis.*

PBE and BP86, as presented in the Figure 5.13. Without the Grimme correction (black curves), the binding energies are much weaker, and differ by $\approx$ 0.3 eV between the two functionals. At the same time, as expected, the profiles exhibit no vdW energetic minimum, confirming its nature.

Including of the Grimme corrections reduces the difference in binding energies at 1.72 Å between two XC functionals efficiently to maximum 0.03 eV (DFT-D3, blue curves) and 0.08 eV (DFT-D2, red curves). At the same time the difference between the binding energies produced with DFT-D2 and DFT-D3 Grimme corrections is 0.2 eV to 0.3 eV (depending on the functional). The positions of the vdW minimum is also different for DFT-D2 and DFT-D3: 2.9 Å and 2.5 Å respectively.

Despite of the major differences in the binding energies and the vdW minimum position between the tested vdW corrections, in general, the bistability, the position of the two closest to the flake energetic minima and the energetic barriers between them are similar and confirm the SCO effect, chemisorbed nature of the binding and the switching behavior.

Density Functional and Hartree-Fock Method

In order to compare different computational methods, we calculate the energy profiles using DFT with different exchange-correlation functionals, as well as using the Hartree-Fock method with Møller-Plesset correction of the second order (MP2) [115] (see Figure 5.14).

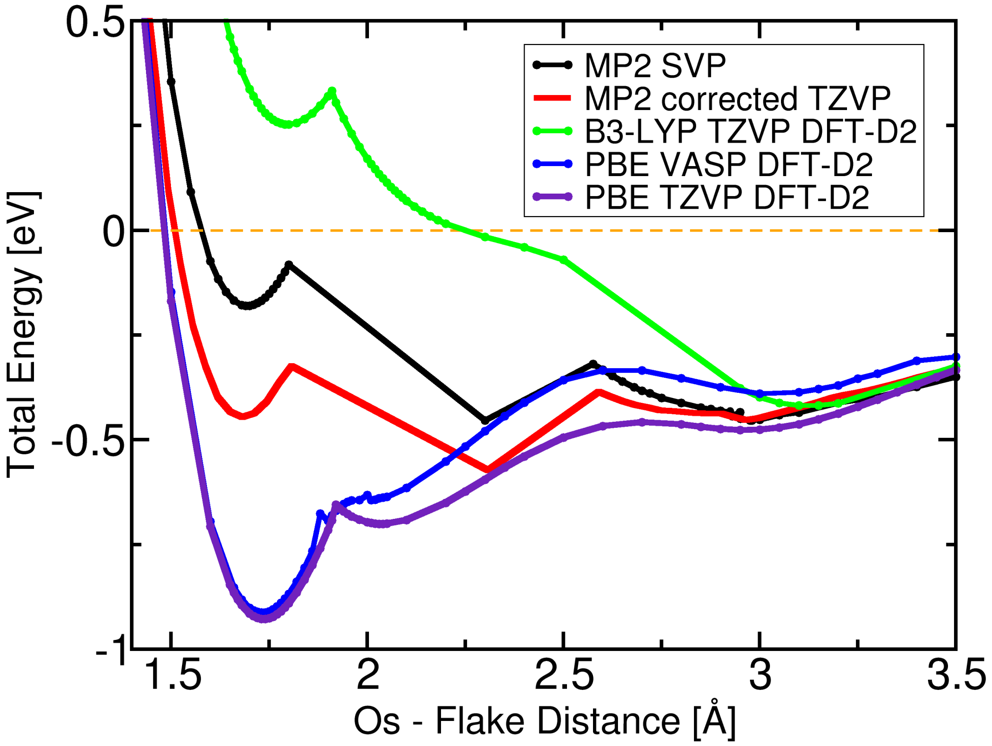

Figure 5.14: *Total energy profiles of Os annealing to the center site of the C18 graphene nanoflake as a function of Os - flake distance. The profiles are calculated using the code TURBOMOLE, utilizing the HF-MP2 method with def2-SVP basis set, the DFT method with the hybrid B3-LYP exchange-correlation functional, the DFT with GGA PBE XC functional, as well as the code VASP with PBE XC functional. Except for the HF-MP2 method, the DFT-D2 correction was included into the DFT calculation to take the van der Waals interaction into account. For better comparison, we introduce the curve for HF-MP2 with def2-TZVP basis set (red) estimated using the correction introduced in Figure 5.12.*

The XC functionals we test here are the GGA-type PBE functional and the hybrid-type B3-LYP functional. The basis set def2-TZVP is used, except for the computationally expensive HF-MP2 method, where we have to use def2-SVP basis set. We utilize the def2-SVP vs. def2-TZVP correction presented in Figure 5.12 to estimate the HF-MP2 energy profile with def2-TZVP basis set. The van der Waals interaction is included in the DFT calculation by the DFT-D2 dispersion correction. The PBE XC functional with DFT-D2 is also used to compare the energy profiles calculated on different codes: TURBOMOLE, which utilizes atomic orbitals as basis set, and VASP, where plane wave functions are used as basis set.

The energy profile calculated with the hybrid B3-LYP functional shows a non-binding ’d’ and ’s’ minima, but a binding ’vdW’ minimum. Shifting of the low-spin state up in energy by the B3-LYP exchange-correlation functional is known from earlier studies [63]. The PBE energy profiles calculated with VASP and TURBOMOLE show similar trends, with the ’d’ minimum as the global minimum. The barrier between the ’d’ and the ’s’ minima vanishes in the VASP

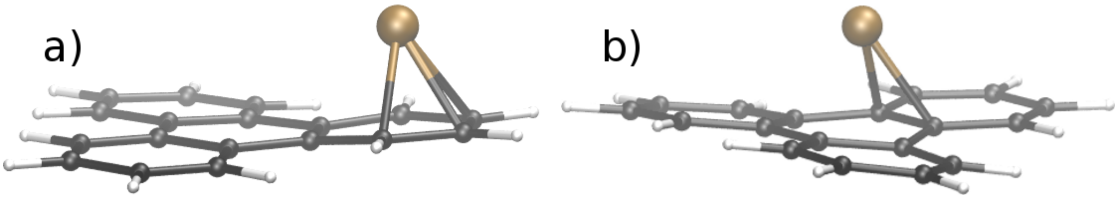

Figure 5.15: *Structure of Os adsorbed on the apex (a) and the center (b) site of the C18 nanoflake after geometry optimization. The optimization of the adsorption energy results in visible distortions of the flake.*

profile, turning the 's' minimum into a shoulder. The corrected HF-MP2 calculations, which we use as a benchmark, show that the most preferable energetic minimum is the 's' minimum, while the 'd' and 'vdW' minima are similar in energy. While the energies at the 'd' and 's' minima strongly depend on the method, all energy profiles show similarities, which are the presence of the 'd' and 'vdW' minima, at least a shoulder at the 's' minimum and significant barriers between the minima.

We conclude that, despite the differences in the results provided by different computational methods, the bistability of Os on graphene nanoflakes is either present and can be reproduced in experiment directly, or can be created by a number of control parameters: the flake size, the adsorption site, the magnetic core material, or the applied external electric field.

5.4.2 Magnetic Anisotropy

Geometry Optimization

During the geometry optimizations of Os on C18 we noticed that the flake was visibly deformed (Figure 5.15). If the flake was positioned on a substrate, such distortion could be restricted by the interaction with the layer underneath. This raises the question of the stability of the anisotropy values against such distortions.

The Table 5.4 shows the calculated magnetic anisotropies for two cases: 1) all atoms are involved in the geometrical relaxation ("Flake free"), and 2) carbon atoms are fixed at their positions during the relaxation, while H and Os are free to move ("Flake fixed"). For the second case the positions of the carbon atoms are determined by geometry relaxation of the flake without an adatom. The calculations were done for Os adsorbed on **Apex** and **Center**. The E_{IOP} turned out to be less sensitive to the geometry variation (less than 3% change in E_{IOP}), while E_{IP} increases by the factor of 10 upon free flake relaxation. This sets a wide error bar on the E_{IP} values presented in this chapter, but on the other hand discovers a way to detect geometry distortions by the magnetic anisotropy measurements. In the next section we consider the influence of the choice of the XC functional on the anisotropy values.

Position	E_{IOP} [meV]	E_{IP} [meV]	Mag. mom [μ_B]
Apex, Flake fixed	24.1	1.45	1.83
Apex, Flake free	23.5	10.21	1.79
Center, Flake fixed	8.6	0.17	1.76
Center, Flake free	8.4	1.62	1.80

Table 5.4: *Magnetic anisotropy energies and the magnetic moment after geometry optimization of Os atom adsorbed to C18 nanoflake. In one case the carbon atoms were allowed to move (Flake free), while in the other only Os and the hydrogen atoms were allowed to change their positions (Flake fixed). The influence of the flake optimization on E_{IOP} is insignificant, while E_{IP} alters by an order of magnitude, allowing an easy detection of geometry distortions by measuring of in-plane anisotropy.*

Density Functional and Hartree-Fock Method

After we showed a high sensitivity of the in-plane anisotropy E_{IP} against the geometry modifications, we consider its dependence on the choice of the XC functional. The magnetic anisotropy for Os on **Apex** of C36 is calculated using the following XC functionals:

- LDA-functional S-VWN [81, 99, 100];
- GGA-functionals BP86 [76, 77, 81, 99, 100] and PBE [75, 99, 100, 108];
- Meta-GGA-functional TPSS [75, 99, 100, 116];
- hybrid functional B3-LYP [76, 78, 81, 99, 100, 117]

and shown in Table 5.5. The hybrid and the metaGGA functionals show high magnetic moments, but reduced anisotropy values. The LDA functional shows an opposite trend: low magnetic moments together with high E_{IOP}. The E_{IOP} and the magnetic moment values calculated with both GGA functionals lie close to each other and between the LDA and metaGGA values. The highest E_{IP} values are provided by the GGA functionals.

In summary, the E_{IOP} values lie between 20.0 and 55.1 meV (factor 2.8), and the E_{IP} vary between 1.2 and 6.5 meV (factor 5.4), depending on the functional. Although such variation sets a high error bar to the anisotropy energies, the general trend (for all functionals the preferred anisotropy direction is in-plane), and the magnitude still indicate a high magnetic anisotropy for Os on graphene flakes.

Functional	E_{IOP}[meV]	E_{IP}[meV]	Mag. mom [μ_B]
B-P (GGA)	31.5	6.5	1.77
PBE (GGA)	32.2	5.5	1.77
B3-LYP (Hybrid)	20.0	1.2	1.84
S-VWN (LDA)	55.1	3.7	1.67
TPSS (metaGGA)	23.7	3.2	1.82

Table 5.5: *Magnetic anisotropy energies and the magnetic moment of Os atom adsorbed at the apex site of the C36 nanoflake calculated with five different exchange-correlation functionals: two GGA functionals, BP86 [76, 77, 81, 99, 100] and PBE [75, 99, 100, 108], one hybrid functional, B3-LYP [76, 78, 81, 99, 100, 117], one LDA functional, S-VWN [81, 99, 100], and one metaGGA functional, TPSS [75, 99, 100, 116]. Both GGA functionals produce similar results. The anisotropy calculated with the hybrid functional is about 50% of the GGA E_{IOP}.*

5.5 Conclusions

Using density functional theory methods we calculated the adsorption energies of 5d transition metal atoms on armchair-edge graphene nanoflakes of various sizes. The most preferable site on all flakes is the apex site. On armchair flakes the adsorption energy decreases with the flake size.

We discovered spin-crossover effect upon adsorption of 5d transition metal atoms onto graphene nanoflakes, which manifests itself in a structural bistability and is accompanied by a massive switching of the magnetic anisotropy. For Os, which was in the focus of our study, the bistability becomes less pronounced with increasing flake size and for positions closer from the edge. We performed a detailed study of the level-crossing on Os adsorbed on the center site of the C36 nanoflake, including the occupation, the energetic and the atomic orbital character of near-HOMO molecular orbitals. An interplay between the adatom atomic orbitals which hybridize and do not hybridize with the carbon π-cloud was identified as the reason for the multiple energetic minima upon adsorption. An additional metastable distance is introduced by the van der Waals interaction.

To justify our findings we tested the calculated energy profiles using different basis sets, dispersion corrections, XC functionals, and quantum chemistry methods, i.e. DFT and Hartree-Fock with Møller-Plesset correction of the second order. The spin crossover effect was found to be present regardless the calculation details, while the exact binding energies turned out to be strongly sensitive on the used method.

We demonstrated how the spin-crossover properties can be tuned by the flake size, the adsorption position, and the choice of the adsorbate. We showed that the switching between the bistable states can be controlled by an external electric field along the Os-flake binding axis.

In- vs. out-of-plane magnetic anisotropy E_{IOP} shows a high robustness with respect to geometry variations, which can be induced by introducing a substrate underneath the flake, and to the choice of the XC functional. The in-plane anisotropy E_{IP} is more sensitive towards the flake modifications, changing by an order of magnitude when the flake is allowed to relax without constrains. Usage of different exchange-correlation functionals for the E_{IP} determination can alter its value by a factor of up to 5.4.

6 Electronic Properties of Ultrasmall Gold Nanoparticles

As of late, ultrasmall gold nanoparticles (usAuNP) are gaining increased attention in research and industry as potentially powerful tools in medicine [34], biomedical imaging [35–38], catalysis [39–43], cancer therapy and diagnosis [36, 44, 45], sensors [46], photonic devices [47], and printed electronics [118]. Thus, unsurprisingly much research is currently being performed, aiming at the synthesis and characterization of gold nanoparticles. Utilizing density functional theory (DFT) in our work, we calculate electronic properties of several examples of gold nanoparticles, aiming at better understanding and characterization of them. Gold nanoparticles consist of a core, containing a variable number of gold atoms, and an organic ligand hull, not unlike the adatom-decorated nanoflakes, as shown in Figure 6.1.

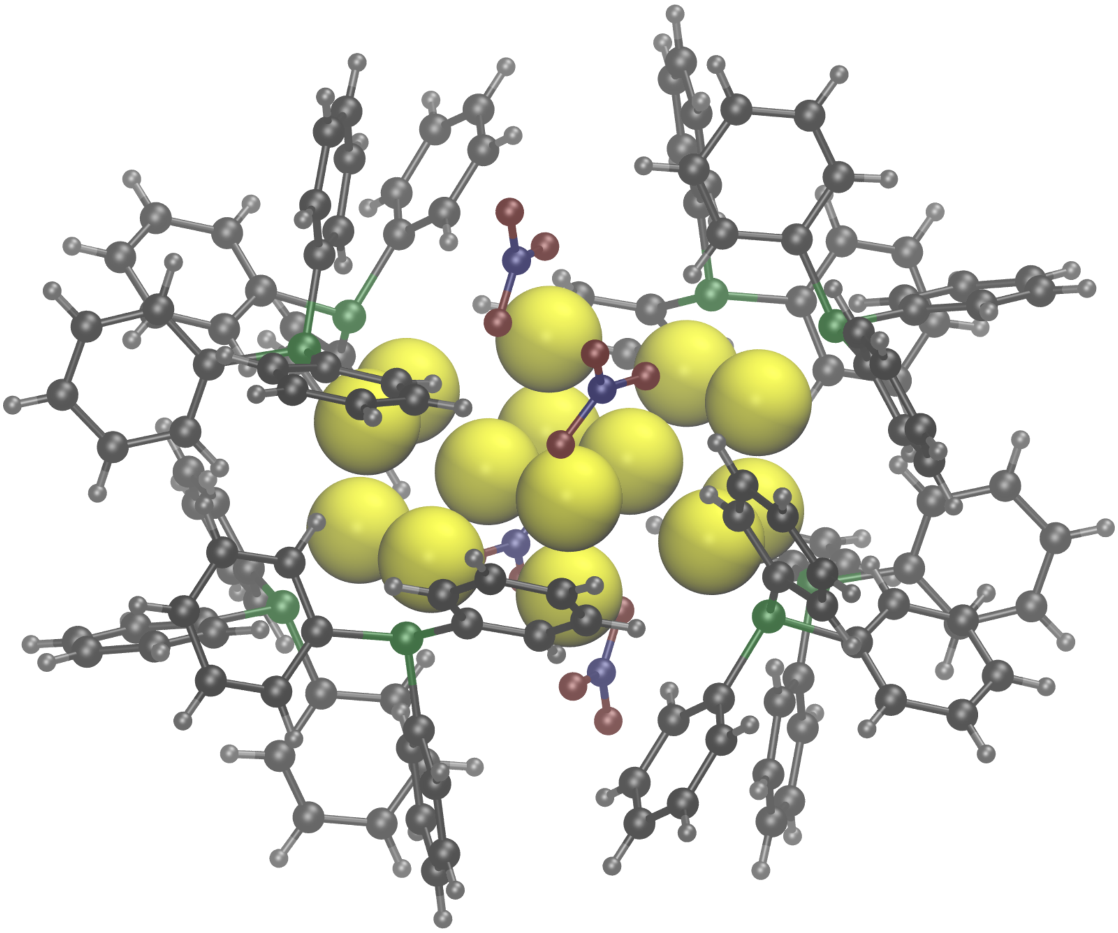

Figure 6.1: *The atomic structure of the* $[Au_{14}(PPh_3)_8](NO_3)_4$ *nanoparticle. The cluster of 14 gold atoms in the middle is surrounded by 8* $P(C_6H_5)_3$ *(i.e.* PPh_3*) and 4* (NO_3) *ligands. The elements are colored as follows: H - grey, C - black, N - blue, O - red, P - green, Au - yellow.*

6.1 Stability of the Au14 Nanocluster

The number of gold atoms in AuNP is variable, but it was shown that certain combinations of gold atoms and ligands can form nanoparticles which exhibit an outstanding stability. One model explaining this observations considers the golden core as a part of the fcc bulk [48, 49], so that the central atom is packed in the shells containing $(10n^2 + 2)$ gold atoms, where n is the shell number. The outstanding stability is then predicted for the clusters with full shells, i.e. with 13, 55, 147, 309, ... atoms.

According to another model [50, 51], the nanoparticles are to be considered as superatom complexes which are most stable when they have full electron shells, similar to the atomic electron shells. The shell-closing number of electrons n^* is

$$n^* = 2, 6, 12, 20, 30, \ldots \tag{6.1}$$

for flat (2D) clusters [119], and

$$n^* = 2, 8, 18, 34, 58, \ldots \tag{6.2}$$

for the 3D clusters (similar to the atomic electron shells of the inert gases). The number n^* of electrons contributing to the superatom shells is equal to the number v_m of the valence electrons of N metal atoms minus the number l_{ew} of electron-withdrawing ligands. If the charge of the nanoparticle is z, then n^* is

$$n^* = Nv_m - l_{ew} - z \tag{6.3}$$

Recently, B. Gutrath experimentally synthesized the gold nanoparticle $[Au_{14}\ (PPh_3)_8\ (NO_3)_4] \cdot (MeOH)_6$ (further called Au14, shown in Figure 6.1) and demonstrated its high stability [2]. The number n^* of the superatom-shell electrons is 10 for this compound, which fulfills the stability criteria neither for the 2D nor for the 3D clusters.

We suggest that an unexpectedly high stability of Au14 can be explained considering the fact, that four of the total 14 gold atoms are located very close to the NO_3 ligands (Au-O distance of about 2.1 Å, which is untypical for AuNP [2]), which allows them to be counted as parts of the electron-withdrawing ligands $Au(NO_3)$, resulting in the shell-closing electron number of $n^* = 6$. This number fulfills the stability criterion for the two-dimensional nanoparticles, while the Au14 cluster has a three-dimensional structure, as it has been shown by means of the X-ray diffraction [2]. It was suggested, that the HOMO (highest occupied molecular orbital) and the LUMO (lowest unoccupied molecular orbital), also called the frontier orbitals, might be planar in this nanocluster. It is known that the frontier orbitals are decisive for binding properties of the molecule [120], because electrons in HOMO and vacancies in LUMO are most available for a reaction. The shape of HOMO and LUMO has an impact on the electronic coupling between the molecule and a reaction partner and therefore determines whether the molecule acts as a two-dimensional or three-dimensional object.

We perform density functional theory calculations on Au14 and visualize the HOMO and the

LUMO. For the calculation, we use both the BP86 and the B3-LYP exchange-correlation (XC) functionals with def2-SVP and def2-TZVP basis sets. The Au14 structure with isosurfaces indicating the HOMO and the LUMO is shown in the Figure 6.2. Visually no difference between the frontier orbital shapes calculated using different methods can be recognized. A strongly two-dimensional character of the frontier orbitals supports the hypothesis that, despite the three-dimensional Au atom arrangement in Au14, its electronic structure possesses a two-dimensional character, which justifies its stability according to the superatom model.

As an additional analysis, which might justify the consideration of four gold atoms as parts of electron-withdrawing ligands, we calculate the nuclei partial charges using the electrostatic potential fit, as implemented in TURBOMOLE [82]. It shows that a $Au(NO_3)$ moiety has a negative charge of approximately 0.5 e$^-$.

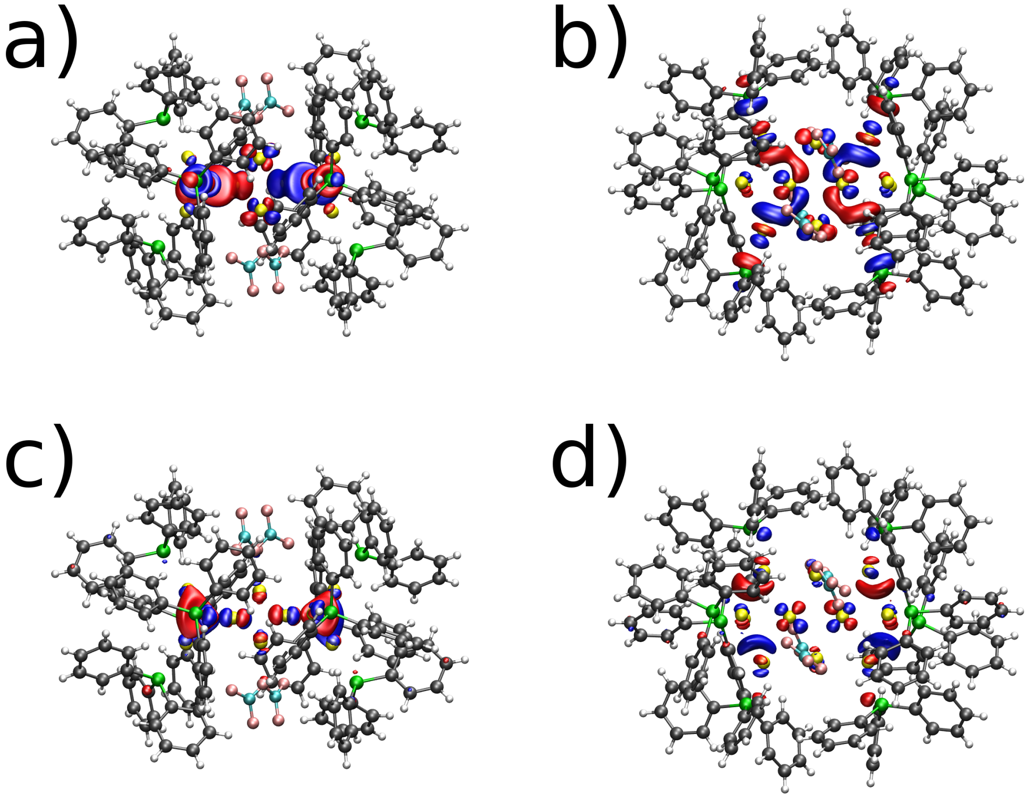

Figure 6.2: *The structure of the Au14 nanocluster with the HOMO (a and b) and the LUMO (c and d) orbitals from the side view (a and c) and the top view (b and d). The orbitals are represented by the equipotential surface of the corresponding charge distribution with the charge density of* $0.03\,\mathrm{e}/\mathrm{a}_0^3$. *The atoms are colored as following: white (H), gray (C), green (P), cyan (N), pink (O) and yellow (Au). The two phases of the molecular orbitals are represented by red and blue. Both HOMO and LUMO show a strongly planar distribution. The figure is previously published in [2].*

6.2 HOMO-LUMO Gap of Au8 and Au9 Nanoparticles

The ultrasmall gold nanoparticles owe a large part of the technological and academic interest to their nonmetallic properties, i.e. a nonzero HOMO-LUMO energy gap $\Delta_{HOMO-LUMO}$. A controllable tuning of $\Delta_{HOMO-LUMO}$ allows the adjustment of properties of such structures to suit a particular purpose. Therefore, finding a way to determine and ultimately design the $\Delta_{HOMO-LUMO}$ is crucial for research and engineering of usAuNP.

Using different XC functionals and utilizing the time-dependent DFT (TDDFT) method we calculate the HOMO-LUMO gap for three usAuNP: $[Au_{14}(PPh_3)_8](NO_3)_4$ (the introduced Au14), $[Au_8(PPh_3)_8](NO_3)_2$ (further: Au8) and $[Au_9(PPh_3)_8](NO_3)_3$ (further: Au9). To validate our methods, we compare the results with the experimental values obtained by our collaborators. This calculations are to be published soon as "Crystal Structure and Electronic Properties of $[Au_8(PPh_3)_8](NO_3)_2$" by Benjamin S. Gutrath, Frank Schiefer, Ulli Englert, Mihaela-Diana Şerb, Wolfgang Bettray, Igor Beljakov, Bernd Speiser, Velimir Meded, Wolfgang Wenzel and Ulrich Simon [5]. The details of the experimental methods are to be found therein.

Cluster	HOMO-LUMO Gap (eV)						
	DFT		TDDFT		Experiment		
	PBE	B3-LYP	PBE	B3-LYP	ΔE_{OES}	ΔE_{pl}	ΔE_p
Au8	2.08	3.06	2.12	2.43	1.97	1.69	1.60
Au9	1.59	2.51	1.65	1.87	2.07	1.77	1.77
Au14	0.35	1.05	0.41	-	-	-	

Table 6.1: *The simulated and the experimentally determined values of the HOMO-LUMO gap for three ultrasmall gold nanoparticles Au8, Au9 and Au14. The calculation was performed using DFT and TDDFT methods with two different types of exchange-correlation functionals: GGA and Hybrid (PBE and B3-LYP respectively). The basis set is def2-TZVP, except for the TDDFT with B3-LYP functional, where a smaller basis set, def2-SVP, is used due to excessive computational time requirement. The TDDFT calculation with B3-LYP did not converge for Au14. The experimental methods are optical extinction spectroscopy (E_{OES}), photoluminescence (E_{pl}) and voltametry (E_p). The details of the experimental methods are to be found in the upcoming paper by B. Gutrath et al. [5].*

The Table 6.1 contains the calculated as well as the experimentally obtained HOMO-LUMO gaps. As stated in [5], the energy obtained by the photoluminescence ΔE_{pl} represents the $\Delta_{HOMO-LUMO}$ most precisely: upon optical excitation, the electron jumps from the HOMO to the level above the former LUMO (ΔE_{OES}). "After intersystem crossing, the excited electron relaxes to the former LUMO without radiation and falls back into the former HOMO by emitting light with ΔE_{pl}" [5].

The theoretically obtained $\Delta_{HOMO-LUMO}$ in Table 6.1 is always overestimating the gap for Au8, compared to ΔE_{pl}. The DFT+PBE calculation overshoots less than the other methods, namely by 0.39 eV. For Au9 the B3-LYP XC functional overestimates the gap (by 0.74 and 0.10 eV with DFT and TDDFT respectively), while the PBE XC functional underestimates it slightly (by 0.18 and 0.12 eV with DFT and TDDFT respectively).

It is notable that the experimental value for $\Delta_{HOMO-LUMO}$ is smaller for Au8, while the computational values show an opposite trend: regardless the method, the gap is always smaller for Au9. Such inconsistence can be explained if we take into account that $\Delta_{HOMO-LUMO}$ was calculated for Au8 and Au9 without including the electron-withdrawing ligands (NO_3), i.e. as $[Au_8(PPh_3)_8]^{2+}$ and $[Au_9(PPh_3)_8]^{3+}$. The spatial distribution analysis of HOMO and LUMO (Figure 6.3) indicates that for Au8 they mostly coincide, while for Au9 they hardly overlap. Hence, the electrostatic response to the ligand field might be different for HOMO and for LUMO of Au9 and lead to a different $\Delta_{HOMO-LUMO}$ value for Au9 when ligands are included into the calculation, while this is unlikely for Au8.

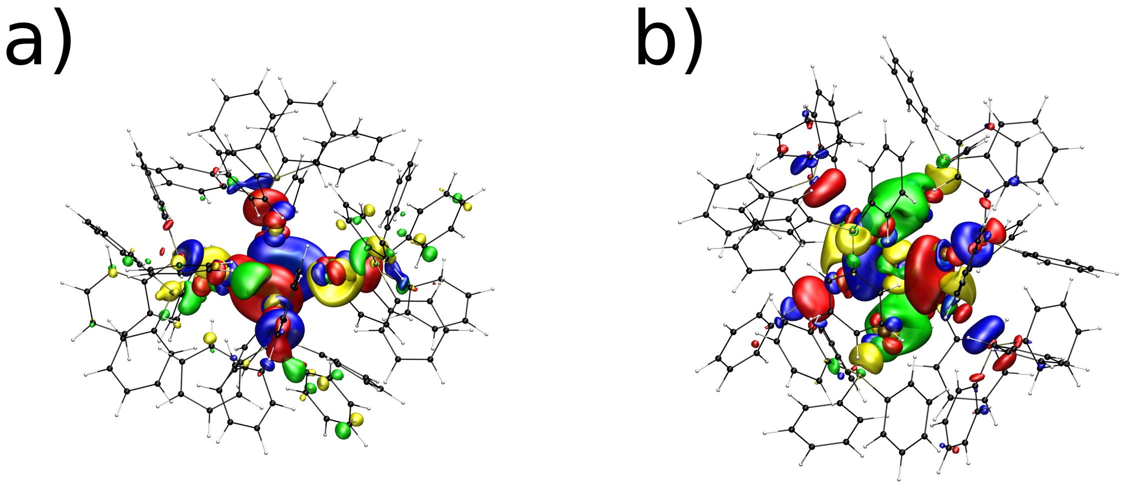

Figure 6.3: *The structures of Au8 (a) and Au9 (b) nanoparticles with the HOMO (red and blue) and the LUMO (yellow and green) orbitals. The orbitals are represented by the equipotential surface of the corresponding charge distribution with the charge density of* ± 0.03 *e/*$a_0{}^3$*. The spatial distribution of HOMO and LUMO of Au8 mostly coincide, while for Au9 HOMO and LUMO barely overlap. The electrostatic responses of HOMO and of LUMO may therefore differ for Au9 upon including ligands in the system and alter the HOMO-LUMO gap.*

We conclude that for an effective application of DFT for the HOMO-LUMO gap determination on nanoparticles, the position of HOMO and LUMO as well as the ligand position might play an important role. Regarding the choice of the method, the HOMO-LUMO gap calculated with the time-dependent DFT (TDDFT) with the PBE exchange-correlation functional is on average closer to the experimental results than the DFT values and the TDDFT result with B3-LYP XC functional.

7 Self-Consistent Ensemble Monte Carlo Simulation of Electronic Transport in Graphene

Electronic devices are increasingly becoming more a commonplace in our everyday lives. Simultaneously with the increased importance increases even the device functionality and complexity, which means that conceptual and technological breakthroughs are constantly being sought for. Graphene is an obvious example of both conceptual and technological breakthrough. Initially, it was theoretically studied more than 50 years ago [121], but the synthesis was achieved only relatively recently [67]. As being the very first literally one-atom-thick material it lead to an activity explosion in the scientific community. Suddenly, two dimensional systems were not just an obscure academic invention, but something that might have an impact on our daily existence, as stability and charge carrier mobility of graphene were found to be superior compared to conventional materials used in electronics. It was predicted that graphene-based transistors could work at THz frequencies. All these properties, partly confirmed and partly predicted, triggered a vast number of research projects on graphene [33, 66, 70, 122]. Graphene-based transistors were produced experimentally by research groups all over the world. However, mobilities measured in experiments were way below theoretical expectations. Mobility in real devices is suppressed by intrinsic defects and scattering mechanisms, partly specific for graphene.

Theoretical models and computer simulations are being developed to understand the details of electronic transport in graphene, but most of the approaches can handle structures of few nanometers in size. To support the development of graphene-based devices substantially simulations of real-size devices on micrometer scale are required. In my work I develop a code which performs a self-consistent ensemble Monte Carlo (EMC) simulation to solve the Boltzmann transport equation (BTE) and the Poisson equation (PE) for mesoscopic devices up to micrometer scale. I have been implementing a framework which allows for including scattering mechanisms relevant for graphene, thus making the method suitable for graphene. Since this method has a notably high efficiency, it should allow simulations of realistic devices.

As a foundation for simulation framework the software code Elmer developed at CSC (Espoo, Finland) has been selected. Elmer is a finite-element software package, which is used to simulate various physical problems by solving differential equations implemented in separate modules of Elmer. Before we started implementing a module to solve BTE, Elmer already provided a complete and functional Poisson Solver and Particle Tracker module, where massive particles can move in a force field and reflect at the walls. Based on the Particle Tracker, I implemented a module to solve the Boltzmann transport equation.

7.1 Boltzmann Transport Equation

The main purpose of the Boltzmann transport equation (BTE) is the determination of the probability density function $f = f(\mathbf{x}, \mathbf{k}, t)$ of particles as a function of position vector $\mathbf{x}$, wavevector $\mathbf{k}$ and time t. The number of particles dN within the space d^3x and the wavevector d^3k at time t is given by

$$dN(\mathbf{x}, \mathbf{k}, t) = f(\mathbf{x}, \mathbf{k}, t) d^3\mathbf{x}\, d^3\mathbf{k} \tag{7.1}$$

Since the wavevector $\mathbf{k}$ is proportional to the particle momentum $\mathbf{p}$ via the de Broglie relation $\mathbf{p} = \hbar\mathbf{k}$, we further use the term *momentum* for $\mathbf{k}$ throughout the chapter. Knowledge of the probability density function f allows to calculate system properties, e.g. particle density

$$n(\mathbf{x}, t) = \int_{-\infty}^{\infty} f(\mathbf{x}, \mathbf{k}, t) d^3k, \tag{7.2}$$

or particle current

$$\mathbf{u}(\mathbf{x}, t) = \int_{-\infty}^{\infty} f(\mathbf{x}, \mathbf{k}, t) \frac{\hbar\mathbf{k}}{m} d^3k \tag{7.3}$$

where m is the particle mass. Note, that in the case of electrons moving in crystals, the limits of integration can be reduced to the first Brillouin zone.

In absence of a force, particle scattering or collisions, i.e. with constant $\mathbf{k}$ for each particle, the distribution function f of particles with constant velocities $\mathbf{v}$ propagates as follows:

$$f(\mathbf{x} + \mathbf{v}\Delta t, \mathbf{k}, t + \Delta t) d^3\mathbf{x}\, d^3\mathbf{k} = f(\mathbf{x}, \mathbf{k}, t) d^3\mathbf{x}\, d^3\mathbf{k} \tag{7.4}$$

The velocity $\mathbf{v}$ depends on $\mathbf{k}$ and on the corresponding dispersion relation $\varepsilon(\mathbf{k})$:

$$\mathbf{v}(\mathbf{k}) = \hbar^{-1} \nabla_{\mathbf{k}} \varepsilon(\mathbf{k}) \tag{7.5}$$

For a parabolic dispersion relation $\varepsilon(\mathbf{k}) = \frac{\hbar^2\mathbf{k}^2}{2m}$, which is valid for electrons close to the conduction band minimum in most materials, the velocity has the classical expression $\mathbf{v}(\mathbf{k}) = \frac{\hbar\mathbf{k}}{m}$. For a linear dispersion relation, e.g. $\varepsilon(\mathbf{k}) = v_F \hbar \sqrt{|\mathbf{k}|^2}$ in graphene, the absolute value of the velocity is independent of $|\mathbf{k}|$, and for graphene equals to the Fermi velocity $v_F \approx 10^6$ m/s, while its direction depends on the wavevector: $\mathbf{v}(\mathbf{k}) = \frac{\mathbf{k}}{|\mathbf{k}|} v_F$. For the sake of clarity, we will further omit $\mathbf{k}$ in $\mathbf{v}(\mathbf{k})$ and use simpler $\mathbf{v}$ instead.

To derive the following equation, let us assume a one-dimensional case, where x, v and k are one-dimensional. Within the time dt the change of the local distribution function $f(x_0, k_x)$ in a box with the sides dx and dk, i.e. in a phase-space box, around x_0 and k_0 is equal to the difference between the numbers of incoming and the outgoing particles, which are $n_{in} = f(x_0 - v_0 dt, k_0) dk dx$ and $n_{out} = f(x_0, k_0) dk dx$ (the velocity v_0 is $v(k_0)$) The local change of $f(x_0, k_0)$ per unit time dt is then

$$\begin{aligned} \frac{\partial f(x_0, k_0)}{\partial t} &= \frac{n_{in} - n_{out}}{dt\, dx\, dk} = \\ &= \frac{f(x_0 - v_x dt, k_0) - f(x_0, k_0)}{dt} \end{aligned} \tag{7.6}$$

with the substitution

$$\begin{aligned}\frac{\partial f(x,k)}{\partial x} &= \frac{f(x+dx,k)-f(x,k)}{dx} \\ \Rightarrow f(x_0 - v_0 dt, k_0) &= \frac{\partial f(x_0,k_0)}{\partial x}(-v_0 dt) + f(x_0,k_0)\end{aligned} \tag{7.7}$$

it can be written:

$$\begin{aligned}\frac{\partial f(x_0,k_0)}{\partial t} &= \frac{(\partial f(x_0,k_0)/\partial x)(-v_0 dt) + f(x_0,k_0) - f(x_0,k_0)}{dt} = \\ &= -v_0 \frac{\partial f(x_0,k_0)}{\partial x}\end{aligned} \tag{7.8}$$

which leads to

$$\frac{\partial f(x_0,k_0,t)}{\partial t} + v_0 \frac{\partial f(x_0,k_0,t)}{\partial x} = 0 \tag{7.9}$$

Introduction of a force $\mathbf{F}$ acting on particles and changing their momentum as $\hbar(\Delta\mathbf{k}) = \mathbf{F}\Delta t$ results in the following evolution of f:

$$f(\mathbf{x} + \mathbf{v}\Delta t, \mathbf{k} + \hbar^{-1}\mathbf{F}\Delta t, t + \Delta t) d^3\mathbf{x} d^3\mathbf{k} = f(\mathbf{x},\mathbf{k},t) d^3\mathbf{x} d^3\mathbf{k} \tag{7.10}$$

With similar argumentation as before, in the three-dimensional case this leads to

$$\frac{\partial f(\mathbf{x},\mathbf{k},t)}{\partial t} + \mathbf{v}\nabla_{\mathbf{x}} f(\mathbf{x},\mathbf{k},t) + \hbar^{-1}\mathbf{F}\nabla_{\mathbf{k}} f(\mathbf{x},\mathbf{k},t) = 0 \tag{7.11}$$

Introduction of particle-particle collisions and other scattering sources (e.g. scattering of electrons on phonons) leads to an additional variation of f with time and adds another term to the Equation 7.11: $\left(\frac{\partial f}{\partial t}\right)_{Scat}$. In the case of particles with charge q moving in an electric field $\mathbf{E}$ and experiencing a force $\mathbf{F} = q\mathbf{E}$, Equation 7.11 becomes:

$$\frac{\partial f}{\partial t} + \mathbf{v}\nabla_{\mathbf{x}} f + \frac{q}{\hbar}\mathbf{E}\nabla_{\mathbf{k}} f = \left(\frac{\partial f}{\partial t}\right)_{Scat} \tag{7.12}$$

which is the most common form of the Boltzmann transport equation.

In the case of charged particles, i.e. in simulations on e.g. electrons or plasma, they have a contribution $\mathbf{E}_{int}$ to the electric field $\mathbf{E} \equiv \mathbf{E}_{tot} = \mathbf{E}_{int} + \mathbf{E}_{\mathbf{ext}}$. Their contribution can be calculated using the Poisson equation:

$$\begin{aligned}\mathbf{E}_{int}(\mathbf{x},t) &= -\nabla_{\mathbf{x}}\phi(\mathbf{x},t) \\ \nabla_{\mathbf{x}}[\epsilon\nabla_{\mathbf{x}}\phi(\mathbf{x},t)] &= qn(\mathbf{x},t)\end{aligned} \tag{7.13}$$

where n is the particle density, calculated from f (see Equation 7.2), ϕ is the electric potential, and ϵ is the permittivity of the material.

Since f is required to calculate $\mathbf{E}$ in Equation 7.13, and $\mathbf{E}$ is required to calculate f in Equation 7.12, these coupled equations need to be solved self-consistently.

The key component of the BTE is the scattering term $\left(\frac{\partial f}{\partial t}\right)_{Scat}$. In absence of particle-particle collisions, particles interact with scattering centers of other types (in the case of electrons these can be phonons, impurities, edges, etc.), which are not included in the BTE per construction, but are taken into account in the scattering term $Q \equiv \left(\frac{\partial f}{\partial t}\right)_{Scat}$, which can be written as

$$Q = \int_{-\infty}^{\infty} [S(\mathbf{k}', \mathbf{k}) f(\mathbf{x}, \mathbf{k}', t) - S(\mathbf{k}, \mathbf{k}') f(\mathbf{x}, \mathbf{k}, t)] d^3k' \tag{7.14}$$

where $S(\mathbf{k}, \mathbf{k}', t)$ is the transition probability from the initial state with momentum $\mathbf{k}$ to the final state with momentum $\mathbf{k}'$ provided that the $\mathbf{k}$-state is occupied, and the $\mathbf{k}'$-state can be occupied. The function $f(\mathbf{x}, \mathbf{k}, t)$ defines the probability that the $\mathbf{k}$-state is occupied. The factor $S(\mathbf{k}, \mathbf{k}')$ depends on the scattering type.

At low electron densities in the momentum space, which is the case of semiconductors at room temperatures, the Pauli exclusion principle (PEP) has an insignificant impact on the scattering procedure and therefore can be neglected in Equation 7.14, which is done in many models solving BTE. For systems with high electron densities in the momentum space, e.g. in metals or graphene at low temperatures, when the momentum space is densely populated with electrons (*highly degenerate electron gas*), the Pauli exclusion principle has to be taken into account. It manifests itself in the factor $(1 - f(\mathbf{x}, \mathbf{k}', t))$ in the scattering term Q, which is the probability that the final state $\mathbf{k}'$ is empty. The resulting scattering term becomes:

$$Q = \int_{-\infty}^{\infty} [S(\mathbf{k}', \mathbf{k}) f(\mathbf{x}, \mathbf{k}', t)(1 - f(\mathbf{x}, \mathbf{k}, t)) - S(\mathbf{k}, \mathbf{k}') f(\mathbf{x}, \mathbf{k}, t)(1 - f(\mathbf{x}, \mathbf{k}', t))] d^3k' \tag{7.15}$$

Since in the 3D case, the BTE is an integro-differential equation in 6 dimensions + time, solving it in this form is a formidable task. A simpler way to find a solution is to use ensemble Monte Carlo methods to simulate the movement of particles, which move according to Newton's law, and scatter according to the scattering term Q. Each *particle* has a well-defined position and velocity. Since the ensemble Monte Carlo can be used to solve BTE on different problems, one *particle* can either stand for a single molecule, atom, electron, etc., or represent multiple atoms, molecules, etc. In the latter case, the particles are called *representative particles*. As our aim is simulation of *graphene* devices, we restricted our simulation to two dimensions both in real and in momentum space (or 2+2+1 dimensions).

7.2 Implementation Details

7.2.1 Data Structure

To express the probability function $f(\mathbf{x}, \mathbf{k}, t)$, which plays a central role in the BTE, in the ensemble Monte Carlo sets of particle properties are used: the position $\mathbf{x}_P$ of the particle P and its momentum $\mathbf{k}_P$. The probability density function at time t is defined as

$$f(\mathbf{x}, \mathbf{k}, t)\ d^2x\ d^2k = \sum_P \left(\prod_i \delta(x_i - x_{P,i}) \delta(k_i - k_{P,i}) \right) d^2x\ d^2k \tag{7.16}$$

with i denoting the two directions of x and k. Using this equation, the essential properties of the system can be extracted in the same way as defined before, see Equations 7.2 and 7.3.

7.2.2 Quantization of Momentum and Position

The finite elements model implies subdividing of the simulated object into a mesh grid in order to solve differential equations at the nodes of the grid, and consequently project the calculated values into the grid cells to get a solution at any position. The subdivision is utilized in the Poisson solver, used to solve Poisson equation and to determine the electric field acting on the particles at their positions.

We also subdivide the momentum space into *momentum cells* in order to take the Pauli exclusion principle (PEP) into account. We determine the size of a momentum cell by considering the electrons as particles in a box. For a sample with the size a_i along the direction i the momentum quantization Δk_i is

$$\Delta k_i = \frac{2\pi}{a_i} \tag{7.17}$$

PEP is used in the scattering term Q in the Boltzmann transport model, where it forbids the scattering into a momentum cell, which is already occupied. In a homogeneous sample, the probability to scatter from $\mathbf{k}$ to $\mathbf{k}'$ is independent from the position, which makes it reasonable to use a single momentum space throughout the sample. With an applied voltage, or for an inhomogeneous sample, the momentum distribution varies, which requires a subdivision of the real space into parts with a separate momentum space for each part. For first tests we use a single momentum space for the whole sample. To save the computational resources we do not take the electron spin into account, allowing only single occupation of a momentum cell. In our simulation we enforce the fulfilling of the Pauli exclusion principle for strongly degenerate cases at any stage of the simulation to avoid collapse of the Fermi sphere.

7.2.3 Initial Setup

At the calculation start, the particles are distributed randomly in real space, while the moments are assigned randomly according to the fermion thermal distribution, i.e. the Fermi-Dirac distribution:

$$f_f(\varepsilon) = \frac{1}{1 + e^{\frac{\varepsilon - \varepsilon_F}{k_B T}}} \tag{7.18}$$

where $f(\varepsilon)$ is the ratio of the number of occupied states with energy ε to the number of available states $D(\varepsilon)$ at this energy.

Determination of the Thermal Distribution Using Inverse Transform Sampling Method

To determine a random energy ε from a Fermi distribution (Equation 7.18) using a random number r from a uniform distribution, we apply *inverse transform sampling* (ITS) method [123].

With parabolic dispersion relation in two-dimensional momentum space the density of states $D(\varepsilon)$ is energy-independent so that the number of electrons at the energy ε is proportional to the Fermi-Dirac distribution $f_f(\varepsilon)$. First, we define a continuous distribution function F:

$$F = \int f_f(\varepsilon) d\varepsilon = -k_B T \ln\left(1 + e^{-\frac{\varepsilon-\varepsilon_F}{k_B T}}\right) + C \tag{7.19}$$

Then we introduce a random number r and set

$$r = F(\varepsilon) \tag{7.20}$$

The energy ε is extracted from the inverse function:

$$\varepsilon = F^{-1}(r) \tag{7.21}$$

which satisfies the Fermi distribution.

Since $r \in [0, 1]$, the function $F(\varepsilon)$ should be normalized to the same range. If we assume a general case, where the density of states does not start at zero, but at the energy ε_C, which is the minimum of the conduction band, the normalization function N_F would be

$$\begin{aligned} N_F &= \int_{\varepsilon_C}^{\infty} f_f(\varepsilon) d\varepsilon = \left[-k_B T \ln\left(1 + e^{-\frac{\varepsilon-\varepsilon_F}{k_B T}}\right)\right]_{\varepsilon_C}^{\infty} = \\ &= k_B T \ln(1 + e^{\frac{\varepsilon_F-\varepsilon_C}{k_B T}}) \end{aligned} \tag{7.22}$$

Therefore, the function $F(\varepsilon)$ equals:

$$\begin{aligned} F(\varepsilon) &= \frac{1}{N_F} \int_{\varepsilon_C}^{\varepsilon} f_f d\varepsilon = \\ &= \frac{1}{N_F}\left(-k_B T \ln(1 + e^{\frac{\varepsilon_F-\varepsilon}{k_B T}}) + k_B T \ln(1 + e^{\frac{\varepsilon_F-\varepsilon_C}{k_B T}})\right) = \\ &= \frac{1}{N_F}\left(-k_B T \ln(1 + e^{\frac{\varepsilon_F-\varepsilon}{k_B T}}) + N_F\right) \overset{!}{=} r \end{aligned} \tag{7.23}$$

Solving this equation for ε yields:

$$\varepsilon = \varepsilon_F - k_B T \ln(e^{\frac{N_F(1-r)}{k_B T}} - 1) \tag{7.24}$$

with

$$e^{\frac{N_F(1-r)}{k_B T}} = e^{(\ln(1+e^{\frac{\varepsilon_F-\varepsilon_C}{k_B T}}))(1-r)} = (1 + e^{\frac{\varepsilon_F-\varepsilon_C}{k_B T}})^{1-r} \tag{7.25}$$

Since r is pulled from a uniform distribution, the expression $(1 - r)$ gives the same distribution as r, which results in the final expression for the energy:

$$\varepsilon(r) = \varepsilon_F - k_B T \ln\left[\left(1 + e^{\frac{\varepsilon_F-\varepsilon_C}{k_B T}}\right)^r - 1\right] \tag{7.26}$$

This method allows for a simple mapping of a random number to particle energy, and therefore to its momentum. Applying it on each particle in the initial stage of the program will produce the Fermi distribution in the momentum space. At the same time, it does not guarantee fulfilling of the Pauli principle, which can result in double occupied momentum cells (note, we do not take spin into account, and therefore do not allow double occupation of the momentum cells). To fulfill the Pauli exclusion principle, we do additionally test whether the momentum cell assigned to a particle is empty and, if not, apply this procedure to calculate a different momentum for the current particle.

In the case of graphene, inverse transform sampling can not be applied, because the density of states $D(\varepsilon)$ close to the Fermi level is linear with energy in graphene, and, therefore, has to be included in the integral in Equation 7.19. The resulting integral

$$F(\varepsilon) = \frac{1}{2}\left(\varepsilon(\varepsilon - 2k_BT\ln(1 + e^{\frac{\varepsilon-\varepsilon_F}{k_BT}})) + 2(k_BT)^2\mathrm{Li}_2(-e^{\frac{\varepsilon-\varepsilon_F}{k_BT}})\right) + C \tag{7.27}$$

with polylogarithm function Li can not be inverted with analytic methods. For this reason, apart from the inverse transform sampling method we implemented a different technique to define the initial state.

Thermal Distribution by Consequent Filling of the Momentum Space

The momentum space is subdivided into momentum cells, which can be enumerated by a sequence of integer numbers. During this initiation procedure we go through the momentum cells, starting from four momentum cells around $|k| = 0$, as shown in Figure 7.1. Once the iteration procedure went through all cells in one rectangular shell (shells are indicated with different colors in Figure 7.1), it starts with the next shell. The first cell in a shell is the most top-right cell (maximum x and maximum y).

For each cell we pull a random momentum $\mathbf{k}_r$ within the cell and calculate the corresponding energy $\varepsilon(\mathbf{k}_r) = \varepsilon_r$ and the corresponding value of the Fermi function $f_f(\varepsilon_r) = f_{f,r}$. An additional random number r_1 determines whether the cell is occupied ($r_1 < f_{f,r}$) or not ($r_1 > f_{f,r}$). The procedure stops when the maximum value of $f_{f,r}$ among the cells in one shell is less then 10^{-8}, i.e. when the probability for more cells to be occupied is vanishing.

Note that the procedure can also be terminated when the maximum number of particles is reached, but it may result in a distortion of the Fermi sphere and should be avoided by setting the allowed maximum number of particles to a reasonably high number. This procedure does not require an exact number of particles in the system to be known in the beginning, as it actually determines this number from the Fermi level, dispersion relation and the momentum quantization. In our code we implemented both types of thermal distribution determination: the inverse transform sampling is used for a weakly degenerate electron gas in systems with parabolic dispersion relation, while the consequent filling is used for a strongly degenerate electron gas. In the strongly degenerate case the occupation of the momentum cells is stored and updated in memory as an extensible list and is used for checking the momentum cell availability during the scattering procedure.

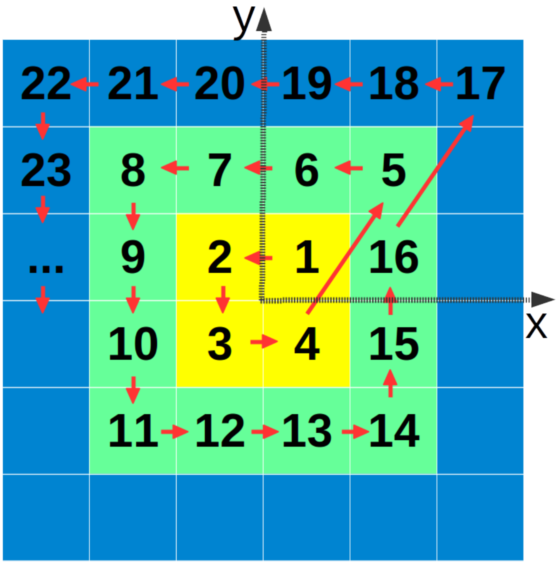

Figure 7.1: *Enumeration of two-dimensional cells, which allows an unambiguous assignment of an integer number to a two-dimensional cell and vice versa.*

7.2.4 Boundary Conditions

In our simulation we implemented two types of system boundaries: quasi-periodic and reflecting. The quasi-periodic walls represent the electrodes connected to the sample. When a particle crosses the quasi-periodic wall, it is reinjected at the opposite electrode with a different momentum $\mathbf{k}'$. The momentum $\mathbf{k}'$ is taken from the Fermi distribution and is determined either by the inverse transform sampling (weakly degenerate electron gas) or utilizing the stored list of occupation of momentum cell as follows: each empty momentum cell C is weighted with the value of the Fermi function $f_f(\mathbf{k}_\mathrm{C})$ for the momentum $\mathbf{k}_\mathrm{C}$, which points to the center of this momentum cell; the final momentum cell C is taken from this weighted distribution, and the corresponding $\mathbf{k}_\mathrm{C}$ is assigned to the particle, i.e. $\mathbf{k}' = \mathbf{k}_\mathrm{C}$. The cells in which $\mathbf{k}_\mathrm{C}$ points towards the boundary are excluded from the list of considered cells. This method is implemented in the function `DoThermalBackscattering`.

When a particle hits the reflecting boundary, its final momentum $\mathbf{k}'$ is also determined using the `DoThermalBackscattering` procedure. As $\mathbf{k}'$ is independent from the initial momentum $\mathbf{k}$, this approach introduces an additional scattering, which incorporates the limited size of the sample into the simulation.

7.2.5 Flow Chart

One self-consistent loop of the simulation consists of several steps, shown in Figure 7.2. In the first step, the internal electric field $\mathbf{E}_{int}$ at the nodes of the finite element grid is calculated from the particle positions utilizing the Poisson Solver implemented in Elmer. In the second step the internal E_{int} and the external E_{ext} electric field and the resulting force $\mathbf{F}$ are calculated for each particle from the field values at the grid nodes utilizing the Particle Tracker module of Elmer. In the third step the particles are accelerated as described in Section 7.2.6 and moved according to

$$\mathbf{x}' = \mathbf{x} + \mathbf{v}\Delta t = \mathbf{x} + \hbar^{-1}\nabla_{\mathbf{k}}\varepsilon(\mathbf{k})\Delta t \tag{7.28}$$

In the fourth step the particles are scattered according to the scattering probability defined in Equation 7.37, which will be explained in more detail in Section 7.2.7.

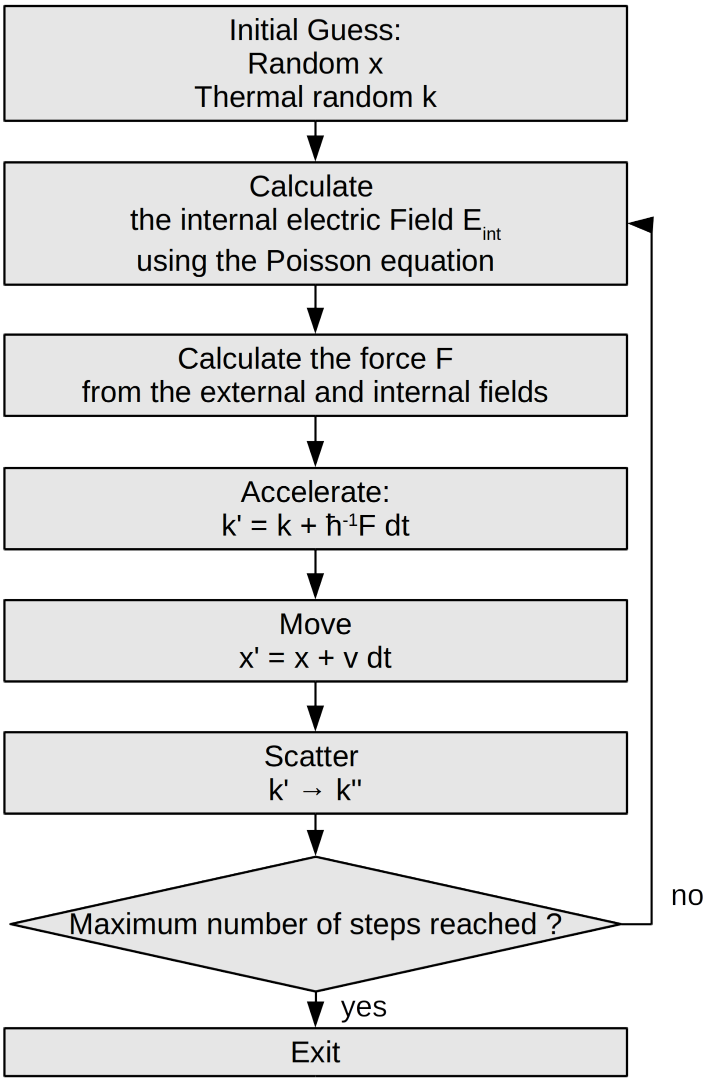

Figure 7.2: *Flow diagram of the general Ensemble Monte Carlo Boltzmann-Poisson solver. The detailed flow charts of the acceleration and the scattering step are shown in Figures 7.3 and 7.4 respectively.*

7.2.6 Acceleration Procedure

During the acceleration procedure the momentum $\mathbf{k}_P$ of a particle P changes to $\mathbf{k}'_P$ according to

$$\mathbf{k}'_P = \mathbf{k}_P + \hbar^{-1}\mathbf{F}_P\Delta t \tag{7.29}$$

for each particle P in the system. The velocity is calculated using the corresponding dispersion relation:

$$\mathbf{v}'_P = \mathbf{v}(\mathbf{k}'_P) = \hbar^{-1}\nabla_{\mathbf{k}}\varepsilon(\mathbf{k}'_P) \tag{7.30}$$

During the acceleration procedure in this form, a violation of the Pauli exclusion principle (PEP) may occur, for example when the final momentum $\mathbf{k}'_P$ is in a different momentum cell C' than $\mathbf{k}_P$ and C' is occupied by a particle R. To avoid the violation of PEP, we forbid acceleration of P into C' as long as C' is occupied. The acceleration procedure goes through the particles sequentially, i.e. if R is handled after P, then R can accelerate and open the vacancy in C' in the same time step. In order to allow P to accelerate within the same time step, the acceleration procedure repetitively goes through the list of particles, handling only particles which were blocked in previous attempts, until no particle can accelerate (either because they are blocked or already accelerated). The flow diagram is shown in Figure 7.3.

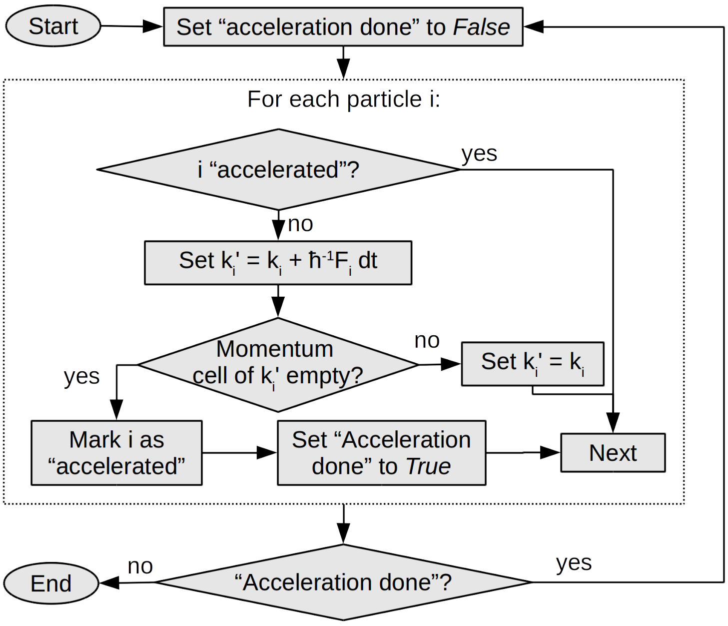

Figure 7.3: *Flow diagram of the acceleration procedure.*

7.2.7 Scattering Procedure

Total Scattering Probability

The scattering term $S(\mathbf{k}, \mathbf{k}')$ is the transition probability from the state $\mathbf{k}$ to $\mathbf{k}'$ per unit time. The total scattering rate for a particle with the momentum $\mathbf{k}$ is

$$\lambda(\mathbf{k}) = \int_\Omega S(\mathbf{k}, \mathbf{k}')d^3k' \tag{7.31}$$

Here for the time being we neglect the Pauli exclusion principle included later. Since the momentum $\mathbf{k}$ changes with time, $\mathbf{k} = \mathbf{k}(t)$, the total scattering rate is implicitly time-dependent: $\lambda(\mathbf{k}) = \lambda(\mathbf{k}(t))$. The scattering probability in the time δt is therefore $\lambda(\mathbf{k}(t))\delta t$. The probability for a particle to move during the time δt without scattering is therefore $1 - \lambda(\mathbf{k}(t))\delta t$. A finite time step Δt can be expressed as a sum of i time intervals δt:

$$\Delta t = \sum_i \delta t \tag{7.32}$$

The probability p_{noscat} to remain unscattered during the time Δt for the particle with an initial momentum $\mathbf{k}(t_0)$ is therefore

$$\begin{aligned}
p_{noscat}(\mathbf{k}(t), \Delta t) = & (1 - \lambda(\mathbf{k}(t_0))\delta t) \cdot \\
& \cdot (1 - \lambda(\mathbf{k}(t_0 + \delta t))\delta t) \cdot \\
& \cdot (1 - \lambda(\mathbf{k}(t_0 + 2\delta t))\delta t) \cdot \\
& \dots \\
& \cdot (1 - \lambda(\mathbf{k}(t_0 + \Delta t))\delta t) \\
& = \prod_i (1 - \lambda(\mathbf{k}(t_0 + i\delta t))\delta t)
\end{aligned} \tag{7.33}$$

Taking the logarithm yields

$$\begin{aligned}
\ln\left(p_{noscat}(\mathbf{k}(t), \Delta t)\right) &= \sum_i \ln(1 - \lambda(\mathbf{k}(t_0 + i\delta t))\delta t) \\
&\approx - \sum_i \lambda(\mathbf{k}(t_0 + i\delta t))\delta t
\end{aligned} \tag{7.34}$$

for $1 \gg \lambda(\mathbf{k}(t))\delta t$ (as $\ln(1-x) \approx -x$ for $x \ll 1$). Replacing the sum with an integral and taking both sides into exponent yields

$$p_{noscat}(\mathbf{k}(t), \Delta t) = \exp\left(- \int_{t_0}^{t_0 + \Delta t} \lambda(\mathbf{k}(t'))\delta t' \right) \tag{7.35}$$

Here we made an assumption that during the time step Δt the momentum change is small enough to keep the scattering rate almost constant: $\lambda(\mathbf{k}(t')) \approx \lambda(\mathbf{k}(t_0))$. The probability for no scattering event is then

$$p_{noscat}(\mathbf{k}(t), \Delta t) = \exp(-\lambda(\mathbf{k}(t_0))\Delta t) = p_{noscat}(\mathbf{k}, \Delta t) \tag{7.36}$$

and the resulting probability for a scattering event becomes:

$$p_{scat}(\mathbf{k}, \Delta t) = 1 - p_{noscat}(\mathbf{k}, \Delta t) = 1 - e^{-\lambda(\mathbf{k}(t_0))\Delta t} \tag{7.37}$$

Time of Flight

In the simulation we allow only one scattering per time step. Therefore, the time of flight Δt has to be chosen so that the probability to undergo a scattering is significantly lower than 1:

$$p_{scat}(\mathbf{k}, \Delta t) = 1 - p_{noscat}(\mathbf{k}, \Delta t) \ll 1 \tag{7.38}$$

If we set the highest allowed value for $p_{scat}(\mathbf{k}, \Delta t)$ to x, we get a formula for Δt:

$$\Delta t < \frac{-\ln(1-x)}{\lambda(\mathbf{k})} \approx \frac{x}{\lambda(\mathbf{k})} \tag{7.39}$$

for $x \ll 1$. In our simulation we use the constant time technique, requiring that the this formula is valid for all $\mathbf{k}$:

$$\Delta t < \min\left(\frac{x}{\lambda(\mathbf{k})}; \mathbf{k}\right) \tag{7.40}$$

Since the scattering rate λ is in most physical cases ever-expanding with growing $k \equiv |\mathbf{k}|$, one needs to estimate the highest possible $k = k_{max}$ and calculate $\lambda(k_{max})$, to get a proper value for Δt. k_{max} can be calculated from the invert dispersion relation $k_{max} = \varepsilon_{max}^{-1}(k)$, while ε_{max} can be estimated from the Fermi distribution if we set $f_f(\varepsilon_{max}) = 1/N$, where N is the number of particles in the system. Under these conditions, there will be one particle in the system of N particles with a high enough momentum $k >= k_{max}$ to have a non-vanishing probability to be scattered more than once during the flight time Δt.

Final Momentum

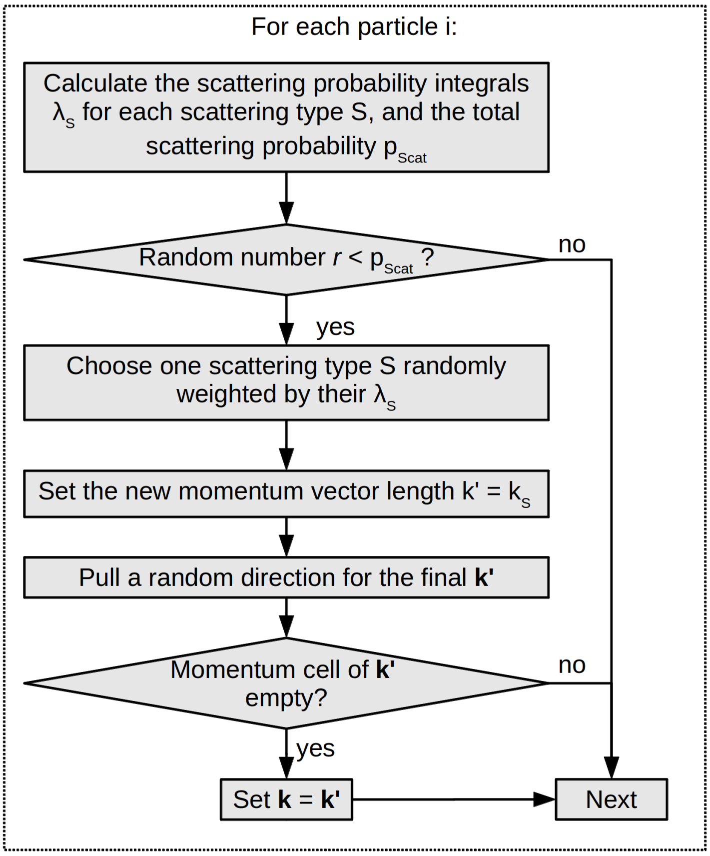

Figure 7.4: *Flow diagram of the scattering procedure of the Ensemble Monte Carlo Boltzmann-Poisson solver.*

In our model we consider multiple scattering mechanisms. Each scattering mechanism (indexed with s) changes the absolute value of the particle momentum $|\mathbf{k}|$ by $(\Delta k)_s$, while the scattering angle is considered to be independent from the direction of $\mathbf{k}$. For initial tests we take into account only the phonon scattering, which can be divided in two subcategories: scattering on acoustic phonons, and scattering on optical phonons. The change in energy due to the interaction with acoustic phonons is so insignificant that the final momentum k' is generally assumed to be equal k: $(\Delta k)_a = 0$. In the case of optical phonon scattering, only phonons with discrete energy values (see Section 7.3.3) are absorbed and emitted, so that the energy, and therefore, the possible momentum change has discrete values. The scattering term $S(\mathbf{k}, \mathbf{k}')$ used in Equation 7.31 can therefore be expressed as a sum of scattering terms $S_s(\mathbf{k}, \mathbf{k}')$:

$$S(\mathbf{k}, \mathbf{k}') = \sum_s S_s(\mathbf{k}, \mathbf{k}') \tag{7.41}$$

so that the total scattering rate $\lambda(\mathbf{k})$ can be expressed as

$$\lambda(\mathbf{k}) = \int_\Omega \sum_s S_s(\mathbf{k}, \mathbf{k}') d^3k' = \sum_s \int_\Omega S_s(\mathbf{k}, \mathbf{k}') d^3k' = \sum_s \lambda_s(\mathbf{k}) \tag{7.42}$$

with the scattering rate $\lambda_s(\mathbf{k})$ provided by the scattering type s. We subdivide the scattering rate of optical phonon scattering into separate parts λ_{s_o}, so that each λ_{s_o} corresponds to only one $(\Delta k)_s$ and that $\sum_{s_o} \lambda_{s_o}(\mathbf{k})$ is the scattering rate of optical phonon scattering. Once the scattering event occurs (with probability defined in according to Equation 7.37), an additional random number determines the type of the occurred scattering, with probability

$$p_{\mathbf{k}}(s) = \frac{\lambda_s(\mathbf{k})}{\lambda(\mathbf{k})} \tag{7.43}$$

for the scattering mechanism s. Since each s corresponds to a unique $(\Delta k)_s$, determination of s defines the absolute value of the final momentum $|\mathbf{k}'| = |\mathbf{k}| + (\Delta k)_s$. The direction of $\mathbf{k}'$ is taken from a uniform distribution. In order to fulfill Pauli exclusion principle into account, we check whether the momentum cell of $\mathbf{k}'$ is empty and, if not, block the scattering by setting $\mathbf{k}' = \mathbf{k}$. Figure 7.4 shows the flow chart of the scattering procedure.

7.3 Proof of Principle

We test our model on a silicon sample with previously tested parameters. For this purpose we take the simulation of $0.4\,\mu\mathrm{m}$ long silicon channel as described by C. L. R. Milazzo [124]. The device is simulated at the lattice temperature $T_L = 300\,\mathrm{K}$ with the applied voltage $U = 2\,\mathrm{V}$. In our simulation we define a sample width of $0.4\,\mu\mathrm{m}$. The momentum space quantization is $\Delta k = 1.571 \times 10^7\,\mathrm{m}^{-1}$. The dispersion relation is parabolic with an effective mass $m^* = 0.32 m_e$ and the electron rest mass m_e. The real space is subdivided into 10 cells, which are utilized for calculation of the electric field via Poisson solver. As proposed in [125], to avoid plasma oscillations, the time step is set to 76 fs. Calculations show that this time step provides a reasonable overall scattering rate of $\approx 20\%$ per time step.

7.3.1 Fermi Level and the Number of Particles

In her report, C. L. R. Milazzo uses n-doped silicon channel with doping density $N_D = 2 \times 10^{17}\,\mathrm{cm}^{-3}$. As the intrinsic carrier concentration of Si is $1.5 \times 10^{10}\,\mathrm{cm}^{-3}$ at 300 K, which is insignificantly small compared to the donor density N_D, the resulting carrier concentration is $n \approx N_D$. We rescale this 3D carrier density to two dimensions by taking $n_{2D} = n^{2/3}$, so that the mean electron-electron distance is conserved, and yield $n_{2D} = 3.42 \times 10^{15}\,\mathrm{m}^{-2}$. For a $0.16\,\mathrm{\mu m}^2$ sample the corresponding number of electrons is 547. Since we fill the momentum space neglecting the particle spin, so that one electron is allowed to occupy one momentum cell, we take only half of these numbers, i.e. assume that one particle represents two electrons (otherwise having the same mass and charge as a single electron). To achieve this electron number, the Fermi energy is set to -0.0588 eV relative to the bottom of conduction band.

7.3.2 Fermi Distribution

In order to validate our approach we analyze the distribution of particles in the momentum space and compare it to the Fermi function at given temperature and Fermi level. First, we consider the system filled using the inverse transform sampling method (see Page 67), with boundary conditions described in Section 7.2.4, i.e. after each wall collision, particle momentum is taken randomly from the Fermi distribution. As Figure 7.5 shows, the resulting energy distribution strongly deviates from the Fermi function. The reason for such discrepancy is violation of the detailed balance, which arises from the fact that fast particles hit the wall more often than slow particles and get on average a lower momentum upon interaction with a wall. This leads to a redistribution of particle momenta in favor of low momenta.

To preserve the occupation distribution according to Fermi-Dirac statistics, we simulate additional ghost-cells, which play a role of electron reservoirs, to determine the final momentum $\mathbf{k}'$ of the reflected/reinjected particle. Let us assume that the $\mathbf{k}'$ has to point away from the wall with a normal $\mathbf{n}_w$, i.e. the scalar product $\mathbf{n}_w \cdot \mathbf{k}'$ is positive. We simulate a spatial cell of infinite height (y_g coordinate; index g is used to indicate the *ghost* cell) and a finite length l_g (x_g coordinate), so that the $\mathbf{x}_g$ vector is parallel to $\mathbf{n}_w$. A number N_g of particles is created at random positions $x_{g,n}$ within $[0; l_g]$. Particle momenta $|\mathbf{k}_n|$ are taken from the Fermi distribution by applying inverse transform sampling, the angle α_{k_n} between $\mathbf{k}_n$ and $\mathbf{x}_g$ is taken from a uniform distribution, and only particles moving in positive x_g direction, i.e. towards the ghost-cell exit, are created, so that $\cos(\alpha_{k_n}) > 0$. The term $t_n = \frac{l_g - x_{g,n}}{|\mathbf{k}_n| \cos(\alpha_{k_n})}$ is used to characterize the time until the particle reaches the ghost-cell exit. Momentum $\mathbf{k}_n$ of the particle n with the lowest t_n is taken as the final momentum $\mathbf{k}'$. Once $\mathbf{k}'$ is determined, the ghost cell is eliminated.

In order to estimate a minimum N_g required to provide Fermi-Dirac occupation distribution in the system, we perform a series of simulations at $U = 0\,\mathrm{V}$, $T = 300\,\mathrm{K}$ and $\varepsilon_F = -0.0588$ eV for N_g varying between 1 and 1000. Figure 7.6 shows that already at $N_g = 6$ the occupation distribution mostly coincides with the $N_g = 1000$ curve, both being close to the Fermi distribution. Therefore we consider $N_g = 6$ to be an optimal number of particles per ghost cell.

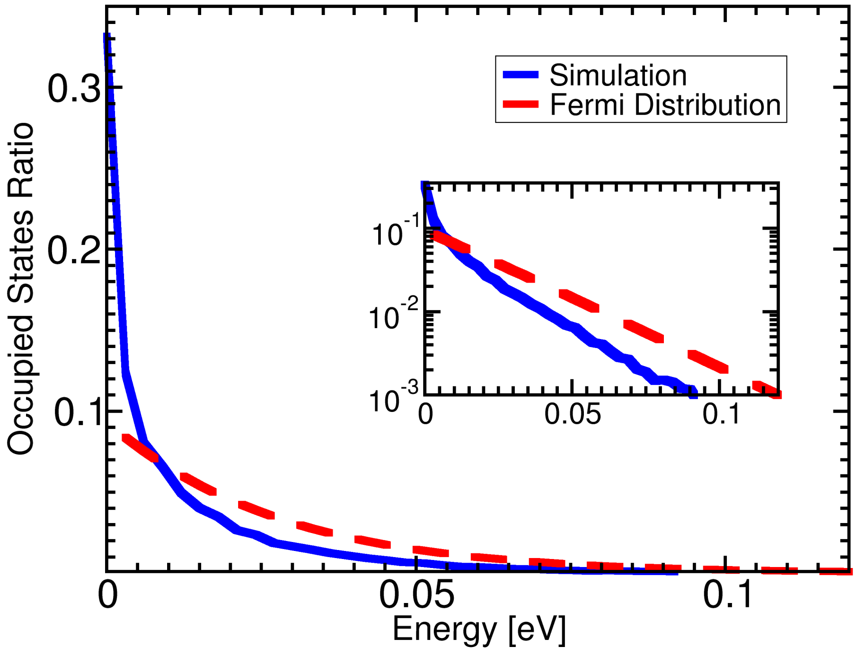

Figure 7.5: *Ratio of the occupied states to the available states as a function of energy. The inset shows the same data plotted with logarithmic y-axis. Simulation (blue) is compared to the Fermi distribution function (red). In both cases the parameters are: temperature $T = 300$ K and the Fermi energy $\varepsilon_F = -0.0588$ eV. In the simulation the only scattering mechanism is the scattering at the walls, with the final momentum taken from the Fermi distribution. In the simulation the occupation distribution is shifted towards the low-energy states.*

7.3.3 Scattering Rates

The scattering taken into account in [124] is the scattering at acoustic and optical phonons. The transition rates are

$$S_{acc}(\mathbf{k}, \mathbf{k}') = K_0 \delta(\varepsilon(\mathbf{k}') - \varepsilon(\mathbf{k})) \tag{7.44}$$

for the acoustic scattering, and

$$\begin{aligned} S_{opt,j}(\mathbf{k}, \mathbf{k}') = K_j[\delta(\varepsilon(\mathbf{k}') - \varepsilon(\mathbf{k}) + \hbar\omega_j)(n_{q_j} + 1) + \\ + \delta(\varepsilon(\mathbf{k}') - \varepsilon(\mathbf{k}) - \hbar\omega_j) n_{q_j}] \end{aligned} \tag{7.45}$$

for the inelastic scattering at the j-th optical phonon. As defined in [124, 125], the coefficients K_0 and K_j are

$$K_0 = \frac{k_B T_L \Xi_d^2}{4\pi^2 \hbar \rho v_s^2} \tag{7.46}$$

$$K_j = \frac{Z_f (D_t K_j)^2}{8\pi^2 \rho \omega_j} \tag{7.47}$$

where Ξ_d is the acoustic-phonon deformation potential, ρ is the mass density of silicon, v_s is the sound velocity of the longitudinal acoustic mode, Z_f is the number of final equivalent valleys for the inter-valley scattering, $(D_t K_j)$ is the deformation potential of the j-th optical phonon, $\hbar\omega_j$ is the phonon energy, and n_{q_j} is the phonon equilibrium distribution function, defined according

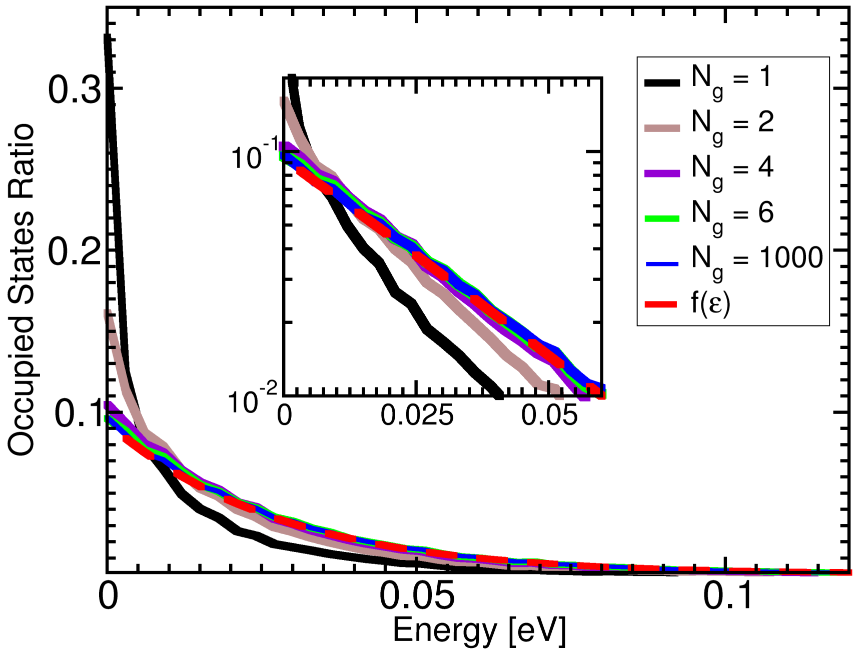

Figure 7.6: *Ratio of the occupied states to the available states as a function of energy. The inset shows the same data plotted with logarithmic y-axis. In the simulation the only scattering mechanism is the scattering at the walls, with the final momentum determined using the ghost-cell technique. Simulations for different number N_g of the particles in the ghost cell are compared to the Fermi distribution function (red). In both cases the parameters are: temperature $T = 300$ K and the Fermi energy $\varepsilon_F = -0.0588$ eV. Simulation with one particle per ghost cell is equivalent to the simulation in Figure 7.5. With increasing number of electrons, the occupation distribution approaches the Fermi distribution. The simulations converge at $N_g = 6$.*

to the Bose-Einstein statistics:

$$n_{q_j} = \frac{1}{e^{\frac{\hbar\omega_j}{k_B T_L}} - 1} \tag{7.48}$$

Tables 7.1 and 7.2 contain the values of the listed variables.

Ξ_d	acoustic-phonon deformation potential	9 eV
ρ	mass density of silicon	2330 kg/m^3
v_s	longitudinal sound speed	9180 m/s
$m*$	effective electron mass	0.32 m_e
m_e	electron rest mass	$9.1095{\cdot}10^{-31}$ kg

Table 7.1: *Scattering parameters for a silicon device. The data is taken from [124].*

As equations 7.44 and 7.45 show, the scattering rates S_{acc} and S_{opt} are independent from the scattering angle, and the only momentum-dependent component of the scattering rates are the Dirac delta-functions. Therefore, the calculation of the scattering rates $\lambda_s(\mathbf{k})$ are quite straightforward. First, we calculate the scattering rate $\lambda_{acc}(\mathbf{k})$ for the acoustic scattering. In order to utilize the spherical symmetry of S_{acc}, we switch to spherical coordinates $d^3k = k^2 \sin(\theta) d\theta d\phi dk$. Using the parabolic dispersion relation $\varepsilon(\mathbf{k}) = \frac{\hbar^2 k^2}{2m^*} \equiv \eta k^2$, we substitute $k' = \sqrt{\frac{\varepsilon'}{\eta}}$ and

j	$\hbar\omega_j$ (meV)	(D_tK_j) (10^8 eV/cm)	Z_f
1	12	0.5	1
2	18.5	0.8	1
3	19.0	0.3	4
4	47.4	2.0	4
5	61.2	11.0	1
6	59.0	2.0	4

Table 7.2: *Parameters used for inelastic scattering at the j-th optical phonon in the test silicon device: phonon energies, deformation potentials and number of equivalent valleys. The data is taken from [124].*

$dk' = \frac{1}{2\sqrt{\varepsilon'\eta}}d\varepsilon'$ and yield:

$$\begin{aligned} \lambda_{acc}(\mathbf{k}) &= \int S_{acc}(\mathbf{k},\mathbf{k}')d^3k' = 4\pi^2 K_0 \int \delta(\varepsilon(\mathbf{k}') - \varepsilon(\mathbf{k}))k'^2 dk' = \\ &= 4\pi^2 K_0 \int \delta(\varepsilon' - \varepsilon)\frac{\varepsilon'}{\eta}\frac{1}{2\sqrt{\varepsilon'\eta}}d\varepsilon' = \\ &= 2\pi^2 K_0 \eta^{-3/2}\sqrt{\varepsilon} = 4\pi^2 K_0 m^* \hbar^{-2} k \end{aligned} \tag{7.49}$$

With similar consideration we calculate the scattering rate at the j-th optical phonon:

$$\begin{aligned} \lambda_{opt,j}(\mathbf{k}) = \int & S_{opt}(\mathbf{k},\mathbf{k}')d^3k' = 4\pi^2 K_j \cdot \\ & \cdot \Bigg[(n_{q_j}+1)\int \delta(\varepsilon(\mathbf{k}') - \varepsilon(\mathbf{k}) + \hbar\omega + j)k'^2 dk' + \\ & + n_{q_j}\int \delta(\varepsilon(\mathbf{k}') - \varepsilon(\mathbf{k}) + \hbar\omega + j)k'^2 dk'\Bigg] = \\ & = 4\pi^2 K_j \frac{m^*}{\hbar^2}\left[(n_{q_j}+1)\sqrt{k^2 - \frac{2m^*\omega}{\hbar}} + n_{q_j}\sqrt{k^2 + \frac{2m^*\omega}{\hbar}}\right] \end{aligned} \tag{7.50}$$

The total scattering rate $\lambda(\mathbf{k})$ is the sum of these partial scattering rates:

$$\lambda(\mathbf{k}) = \lambda_{acc}(\mathbf{k}) + \sum_{j=1}^{6}\lambda_{opt,j}(\mathbf{k}) \tag{7.51}$$

Electron velocity

Figure 7.7 shows the simulated electron velocity and energy at different distances from the leads in a $0.4 \times 0.4\,\mu\mathrm{m}$ device at $T = 300\,\mathrm{K}$ and $U = 2\,\mathrm{V}$. The electric field accelerates the electrons towards the right electrode. The velocity values of up to 3.9×10^5 m/s are higher by a factor ≈ 40 than 1×10^4 m/s reported in [124]. To compare our simulation with [125], we also perform simulation at the source-drain voltage $U = 1$ V. Maximum particle velocities and energies produced in our simulation and reported in [124] and [125] are listed in Table 7.3. The resulting particle velocity of up to 2.8×10^5 m/s is higher than 1.2×10^5 m/s reported in [125] by a factor of ≈ 2.3. The energy calculated from particle momentum reaches the values of 0.1 eV ($U = 1$ V) and 0.19 eV ($U = 2$ V), which is comparable to 0.2 eV ($U = 1$ V) and 0.3 eV ($U = 2$ V) reported in [125] and [124] respectively.

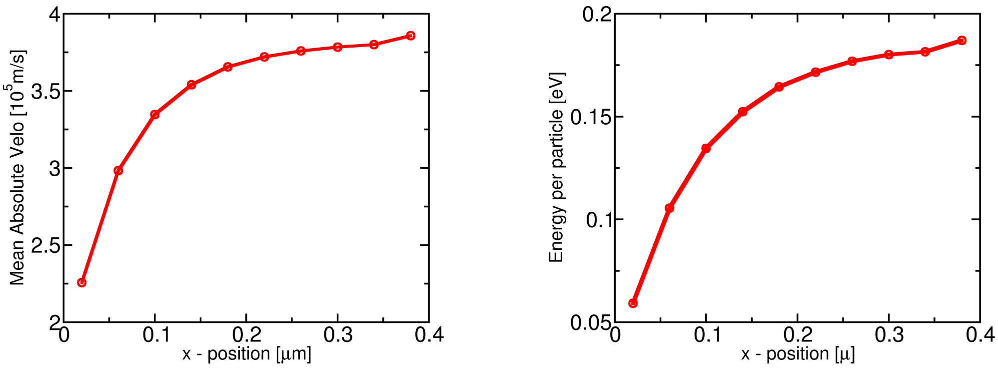

Figure 7.7: *Electron velocity and energy distribution along the sample at an applied voltage of 2 V. The electric field is applied along the x axis.*

Voltage	1V		2V	
Published in	This work	Di Stefano [125]	This work	Milazzo [124]
$\|\mathbf{v}\|$ [m/s]	2.8×10^5	1.2×10^5	3.9×10^5	1×10^4
ε [eV]	0.1	0.2	0.19	0.3

Table 7.3: *Comparison of the maximum values of the particle velocity $|\mathbf{v}|$ and energy ε per particle reached in comparable silicon samples in our model and in previously published reports.*

7.4 Outlook

Our ongoing work is to expand the created framework with numerous parameters in order to simulate specific devices. The scattering mechanisms specific for graphene (e.g. flexural scattering [126], or scattering at charged impurities [127]), the gate voltage and inhomogeneity of the device (separate k-spaces) are ongoing tasks of our research. The constant time technique will be compared with the self-scattering technique, to estimate the errors introduced by either methods, as described in [125]. Multi-valley dispersion relation is also a goal of this project.

8 Summary and Outlook

Prediction and analysis of structural, electronic and magnetic properties of materials using computational methods has emerged as a standard practice in modern theoretical physics. With the evermore decreasing size and increasing complexity of a large variety of nanodevices quantum mechanical calculations have become increasingly effective means of designing new materials, as experimental and analytic approaches are seldom able to scan the whole parameter space.

Among the most formidable challenges of materials science in the recent years is the improvement of the information processing devices. The winners of the competition of Future and Emerging Technologies Flagship initiative initiated in 2014 by the European commission illustrate the relevance of computing and information technologies to our society: one flagship project deals with graphene, a material theoretically capable to drive the microprocessor frequency up to 1 THz; and the other is the Human Brain Project, which utilizes high performance computing resources to simulate the human brain.

The graphene project targets one of the frontiers of the modern semiconductor technology: silicon-based semiconductors have reached the physical limit for the frequency, such that new materials have to be found/designed to accelerate modern CPUs beyond that limit. Another bottleneck for information processing and storage in the next 10 years will be the storage density of standard information storage devices, which has already increased by three orders of magnitude during the last decade. To keep up with this trend, fundamental breakthroughs in the basic sciences are necessary to make it possible to store one bit of information in a single molecule. Such devices require a mechanism for controlled switching (to write the information) between two or more metastable states, which have to be easily distinguishable (to read-out the information) and separated by a high energetic barrier (to store the information).

In this thesis I investigated a combination of two types of single-molecule magnetic storage devices: single molecule magnets (SMM) [7–13] and spin-crossover (SCO) molecules [22, 61, 94]. The basic molecular structure of present-day devices for both types of systems is similar: a core consisting of transition metal or rare earth atoms (magnetic centers) is stabilized by the surrounding organic hull (ligand). SMMs usually contain more than one magnetic center, while molecular magnets with a single magnetic center, so-called single ion magnets (SIM), were also reported recently [14–20]. A SCO molecule typically requires only one magnetic center.

In SMMs the information can be stored in the magnetization direction, similar to conventional data storage devices. The direction of the magnetic moment can be read out or written by an external magnetic field. Strong magnetic anisotropy, leading to a well-defined easy magnetization axis, establishes an energetic barrier between the two states and prevents SMM from thermally induced switching. In present-day systems, the lifetimes of SMM magnetic states are strongly limited by quantum tunneling, which allows transitions through the energy barrier. The function of present-day SMM is therefore limited to cryogenic temperatures.

In contrast to SMM spin crossover (SCO) systems change their total spin (between low and high spin multiplicity) under an external influence. Compared to SMM, instead of the direction, the length of the magnetic moment vector is used to store information in a SCO molecule. In many cases switching can be controlled by an external electric field. SCO is a magneto-mechanical effect, i.e. the magnetic center-ligand distance changes upon the transition by ≈ 0.3 Å. This feature of SCO decouples the two states in the SCO molecule, prevents quantum state mixing and hence allows long lifetimes. Reading-out the stored information is a challenging task, though, since the low-spin and high-spin states are difficult to distinguish experimentally. The two widely used methods to distinguish the spin states, namely X-ray spectroscopy and measurement of magnetic susceptibility as function of temperature, are less suitable for magnetic storage applications. The applicability of SCO is therefore limited by the read-out technique to very low temperatures.

To circumvent the limitations of SMM and SCO systems, we suggest to combine their properties to build a molecular switch, which would change the easy magnetization direction (easy read-out) upon a SCO (stable states). To achieve this, magnetic atoms with a strong magnetic anisotropy are required. Heavy elements, like 4d and 5d transition metals (TM), which possess a high spin-orbit coupling, required for magnetic anisotropy, fit this purpose very well. It is known, though, that conventional ligand cages quench the magnetic moment of these atoms. An unconventional kind of ligand is therefore needed to preserve the magnetization.

Recently, there has been an increasing number of investigations on adsorption of 4d and 5d TM on flat surfaces [24, 28–30, 70]. TM atoms adsorbed on graphene showed a high magnetic anisotropy [23, 24, 29]. For cobalt adatom on graphene even an energetic double well, accompanied by a rearrangement of atomic orbital occupation, was reported [31]. These reports made graphene an attractive candidate for our study.

Most of the theoretical investigations of graphene have not considered the influence of the edge, which is an inevitable feature of a real graphene sheet in experiment. To investigate the influence of the edge on the adsorption and magnetic properties of the magnetic center adsorbed on graphene, we focused our study on finite triangular flakes of graphene, where the variation of the adsorption sites allowed the analysis of the edge effect. Graphene edge can have two regular configurations depending on the cutting vector – armchair and zigzag. A triangular shape of the flakes was chosen as the simplest shape, where the same edge type can be found on all sides of the flake. From the device perspective it is also sensible to study finite systems to limit the possible diffusion of the adatoms on the graphene sheet in order to localize the stored information. To study the energetic, magnetic and electronic properties of graphene nanoflakes decorated with 4d and 5d transition metals we performed calculations utilizing the density functional theory (DFT), a well-established tool for computing of the quantum mechanical properties of molecules.

While both armchair and zigzag edges can serve as a "ligand" for the adatoms, the intrinsically magnetic zigzag edge nanoflakes quench the adatom magnetic moment substantially and make the adsorption process very complicated, e.g. (anti-)ferromagnetic coupling between the adatom and the flake, etc. At the same time, Ru (4d TM) adatoms on armchair flakes showed an in- vs. out-of-plane magnetic anisotropy of only 3.5 meV, a value fairly small when compared to the room temperature. Therefore we focused our study on heavier 5d transition metals on (non-magnetic) armchair nanoflakes.

Osmium showed much higher magnetic anisotropy energies of up to $31.4\,\mathrm{meV}$ when adsorbed on flakes consisting of 36 carbon atoms, and $75.1\,\mathrm{meV}$ on a single benzene ring. At the same time, adsorbed Os possesses a different spin state (S=1, low spin) than a free Os atom (S=2, high spin), which is an indication for a possible spin-crossover. Gradually annealing an Os atom onto nanoflakes, we calculated the binding energy profile as function of the distance. The energy profiles on the off-edge carbon rings of finite flakes exhibited a double-well with two metastable states at $1.7\,\text{Å}$ and $2.0\,\text{Å}$ distance from the flake. The magnetic anisotropy turned out to change its preferred direction between the states, i.e. the preferable magnetization direction was in-plane (out-of-plane) for the low (high) spin state. Realizing that for a true molecular switch we only need a way to control the spin transition, we applied an electric field perpendicular to the flake plane, and showed that it can reverse the energetic order of the metastable states, and thus control the magnetic moment of the atom.

We performed similar calculations with other 5d transition metal atoms as magnetic centers and showed that the spin-crossover, the bistability, or both are present on all of them and can be tuned by the choice of the flake size and the adsorption site. The findings were tested with a number of density functionals, quantum-mechanical methods (DFT and Hartree-Fock with Møller-Plesset correction of the second order), basis sets and dispersion corrections, and demonstrated that the bistability is present in the energy profiles regardless the chosen computational methods. Summarizing this investigation we find that 5d transition metal atoms absorbed on finite graphene flakes combine the attractive features of SMM and SCO systems and may provide the first room temperature molecular magnetic storage device with the potential to increase the storage density of magnetic storage devices by several orders of magnitude.

In the second study reported in this thesis I have investigated the electronic structure of ultrasmall gold nanoparticles (AuNP). Having a vast number of applications in medicine [34], biomedical imaging [35–38], catalysis [39–43], cancer therapy and diagnosis [36, 44, 45], sensors [46], and photonic devices [47], investigation of AuNP forms a major field of research. We used DFT to characterize the electronic state of $[Au_{14}(PPh_3)_8(NO_3)_4]$ nanoparticle, which is particularly interesting because its molecular formula matches neither the nanocrystal [48, 49], nor the superatom complex [50, 51] stability criterion, while exhibiting good stability at ambient conditions [2]. We found that four of its gold atoms located unusually close to the (NO_3) ligands can be considered to be part of the electron-withdrawing ligands $Au(NO_3)$. Our DFT calculations with subsequent electrostatic potential projections (ESP) showed a net charge of 0.5 e^- per $Au(NO_3)$ fragment, supporting this conclusion. In this scenario application of the superatom counting rules [50, 51] predicts a stability for flat (two-dimensional) gold clusters, while the X-ray analysis shows that the gold atoms are distributed in three dimensions in Au14.

Suspecting that its frontier orbitals may have a flat structure, leading to two-dimensional-cluster-like behavior, we calculated the electron density isosurfaces of HOMO and LUMO of Au14, and demonstrated their quasi-two-dimensional shape, confirming that Au14 can be considered as flat Au_{10} cluster with four $Au(NO_3)$ ligands, which explains its extraordinary stability.

In the last part of this thesis we investigated an ensemble Monte Carlo approach on a finite element grid to solve the Boltzmann transport equation for electrons in two-dimensional nanostructures, with the goal to simulate the transport properties of realistic electronic components. Our model allows an implementation of a range of scattering terms. To ensure the applicability of this model for strongly degenerate electron gas, which is relevant for instance in graphene, we include the Pauli exclusion principle in the scattering mechanism. To show the functionality of our code we simulated a $0.4 \times 0.4\,\mu\mathrm{m}$ device with the silicon material parameters.

Outlook

The development of a graphene-based single molecule magnetic switch (GSMMS) demonstrated in our work opens new possibilities in the field of molecular memory devices. The aim of our future work is the investigation of spin crossover effect on graphene flakes of different shapes, e.g. hexagonal or rhomboid, including flakes with both zigzag and armchair edge. Apart from this, more sophisticated computational methods, like complete active space self consistent field (CASSCF) or random phase approximation (RPA), will be used and compared to determine adsorption profiles and anisotropy more precisely. Considering a high spin orbit coupling of rare earth elements, they also will be investigated as potential candidates for GSMMS. It is also interesting to study the influence of substrate underneath the nanoflakes on the magnetic properties of the adatom, which can provide additional possibilities to tune the GSMMS properties.

Another prospect of our future work is the further development of the ensemble Monte Carlo model for electronic transport on the mesoscopic scale. The development of this method is still in progress, in particular with regard to the implementation of the time-dependent gate voltage, graphene charge puddles and graphene-specific scattering mechanisms. The long-term goal of this project is to simulate graphene-based electronic components at THz frequencies to be able to support the design of graphene-based electronic components.

List of Abbreviations

DFT Density functional theory

XC Exchange-correlation

TM Transition metal

E_{IOP} In- vs. Out-of-plane magnetic anisotropy energy

E_{IP} In-plane magnetic anisotropy energy

SMM Single molecule magnet

SIM Single ion magnet

SCO Spin-crossover

MAE Magnetic anisotropy energy

HF Hartree Fock method

MP2 Møller-Plesset correction of the second order

AuNP Gold nanoparticle

usAuNP Ultrasmall gold nanoparticle

BTE Boltzmann transport equation

au Atomic units

HOMO Highest occupied molecular orbital

LUMO Lowest unoccupied molecular orbital

Acknowledgments

PhD studentship at the AG Wenzel has been a very pleasant, interesting, and fruitful time for me, due to the people who were around me during this time. I would like to thank everybody who was supporting me in one or another way during my time at KIT.

First, I would like to thank Prof. Wolfgang Wenzel for accepting me as a PhD student into AG Wenzel and for being my supervisor and mentor. He showed me by example how a proper leader has to be: inspiring, helpful and effective at the same time. I was astonished by his trust in each student, and by the fact that I have never witnessed any other but constructive criticism coming from him. This is a very valuable experience for me. I also appreciate sending me to various conferences, so that I could see a bit of the world and make a number of very interesting acquaintances. I also thank Prof. Gerd Schön for reviewing my thesis and for constructive and fruitful discussion on my work.

I thank Dr. Velimir Meded for being Velimir Meded, a dedicated supervisor and a friendly colleague. The number of things he has taught me about physics and chemistry can only be beaten by the number of things not related to science he has taught me, and I am not able to judge which of them are more valuable for my future life. A lot of valuable thoughts and ideas were produced in our discussions. Working with Velimir was also a significant improvement for my spoken English, which I appreciate too.

I thank my roommates Franz Symalla and Pascal Friederich for sharing office with me, for being helpful when I needed advice, and for fruitful and enlightening discussions. I thank Dr. Timo Strunk, Dr. Ivan Kondov, and Stefan Bozic for being extraordinary helpful with any technical and non-technical issue I ever asked them. I thank Dr. Julia Setzler for being the good soul of the AG Wenzel, and Nana Heilmann for taking this post after Julia was no longer at INT. I thank Dr. Priya Anand, Dr. Angela Poschlad, Dr. Denis Danilov, Dr. Martin Brieg, Tobias Neumann, Paul Kleine, Dr. Moritz Wolf, Dr. Konstantin Klenin, Dr. Alex Schug and Claude Sinner for interesting conversations and good time I had in their company. I thank Peter Råback and Maged Morsi for a warm reception during the two weeks I spent in Helsinki working on my project.

I thank my friends Elshad Shirinov, Michael Matveev and Erik Dmitriy Palatnik for not forgetting me and still visiting me now, when we are quite far apart. I want to thank my parents for all the love and support they gave me during my life. I thank my daughter Adelina for keeping me in a good mood regardless the tiredness or stress. Finally, I want to thank my beloved Alvina for the patience, support and love through all the years and for making me a most invaluable present I can imagine.

List of Figures

List of Tables

Bibliography

[1] Igor Beljakov et al. "Magnetic anisotropy of graphene quantum dots decorated with a ruthenium adatom". In: *Beilstein Journal of Nanotechnology* 4 (2013), pp. 441–445. ISSN: 2190-4286. DOI: `10.3762/bjnano.4.51`.

[2] Benjamin S. Gutrath et al. "[Au14(PPh3)8(NO3)4]: An Example of a New Class of Au(NO3)-Ligated Superatom Complexes". In: *Angewandte Chemie International Edition* 52.12 (2013), pp. 3529–3532. ISSN: 1521-3773. DOI: `10.1002/anie.201208681`. URL: `http://dx.doi.org/10.1002/anie.201208681`.

[3] Igor Beljakov et al. "Spin-Crossover and Massive Anisotropy Switching of 5d Transition Metal Atoms on Graphene Nanoflakes". In: *Nano Letters* 14.6 (2014). PMID: 24762041, pp. 3364–3368. DOI: `10.1021/nl500872c`. eprint: `http://dx.doi.org/10.1021/nl500872c`. URL: `http://dx.doi.org/10.1021/nl500872c`.

[4] Franz Symalla et al. "Band Gap Engineering with a Twist: Formation of Intercalant Super-lattices in Twisted Graphene Bilayers". Submitted to *Phys. Rev. Lett.*

[5] Benjamin S. Gutrath et al. "Crystal Structure and Electronic Properties of [Au8(PPh3)8] (NO3)2". Preprint for J Phys Chem C.

[6] R. Sessoli et al. "Magnetic bistability in a metal-ion cluster". In: *Nature* 365.6442 (1993), pp. 141–143. DOI: `10.1038/365141a0`. URL: `http://dx.doi.org/10.1038/365141a0`.

[7] Lapo Bogani and Wolfgang Wernsdorfer. "Molecular spintronics using single-molecule magnets". In: *Nat Mater* 7 (3 2008), pp. 179–186. DOI: `10.1038/nmat2133`. URL: `http://dx.doi.org/10.1038/nmat2133`.

[8] Constantinos J. Milios et al. "A Record Anisotropy Barrier for a Single-Molecule Magnet". In: *Journal of the American Chemical Society* 129.10 (2007). PMID: 17309264, pp. 2754–2755. DOI: `10.1021/ja068961m`. eprint: `http://dx.doi.org/10.1021/ja068961m`. URL: `http://dx.doi.org/10.1021/ja068961m`.

[9] David P. Mills et al. "A delocalized arene-bridged diuranium single-molecule magnet". In: *Nat Chem* 3 (6 June 2011), pp. 454 –460. DOI: `10.1038/nchem.1028`. URL: `http://dx.doi.org/10.1038/nchem.1028`.

[10] Robin J. Blagg et al. "Magnetic relaxation pathways in lanthanide single-molecule magnets". In: *Nat Chem* 5 (8 Aug. 2013), pp. 673 –678. DOI: `10.1038/nchem.1707`. URL: `http://dx.doi.org/10.1038/nchem.1707`.

[11] Victor Mougel et al. "Uranium and manganese assembled in a wheel-shaped nanoscale single-molecule magnet with high spin-reversal barrier". In: *Nat Chem* 4 (12 Dec. 2012), pp. 1011 –1017. DOI: `10.1038/nchem.1494`. URL: `http://dx.doi.org/10.1038/nchem.1494`.

[12] Yuan-Yuan Zhu et al. "Zero-field slow magnetic relaxation from single Co(ii) ion: a transition metal single-molecule magnet with high anisotropy barrier". In: *Chem. Sci.* 4 (4 2013), pp. 1802–1806. DOI: `10.1039/C3SC21893G`. URL: `http://dx.doi.org/10.1039/C3SC21893G`.

[13] Matteo Mannini et al. "Magnetic memory of a single-molecule quantum magnet wired to a gold surface". In: *Nat Mater* 8 (3 Mar. 2009), pp. 194 –197. DOI: `10.1038/nmat2374`. URL: `http://dx.doi.org/10.1038/nmat2374`.

[14] Shang-Da Jiang et al. “An Organometallic Single-Ion Magnet”. In: *Journal of the American Chemical Society* 133.13 (2011). PMID: 21401130, pp. 4730–4733. DOI: `10.1021/ja200198v`. eprint: `http://dx.doi.org/10.1021/ja200198v`. URL: `http://dx.doi.org/10.1021/ja200198v`.

[15] Matthew Jeletic et al. “An Organometallic Sandwich Lanthanide Single-Ion Magnet with an Unusual Multiple Relaxation Mechanism”. In: *Journal of the American Chemical Society* 133.48 (2011). PMID: 22032273, pp. 19286–19289. DOI: `10.1021/ja207891y`. eprint: `http://dx.doi.org/10.1021/ja207891y`. URL: `http://dx.doi.org/10.1021/ja207891y`.

[16] Jun-Liang Liu et al. “A Six-Coordinate Ytterbium Complex Exhibiting Easy-Plane Anisotropy and Field-Induced Single-Ion Magnet Behavior”. In: *Inorganic Chemistry* 51.15 (2012). PMID: 22799446, pp. 8538–8544. DOI: `10.1021/ic301115b`. eprint: `http://dx.doi.org/10.1021/ic301115b`. URL: `http://dx.doi.org/10.1021/ic301115b`.

[17] Dong-Ping Li et al. “Single-ion magnets based on mononuclear lanthanide complexes with chiral Schiff base ligands [Ln(FTA)3L] (Ln = Sm, Eu, Gd, Tb and Dy)”. In: *Chem. Commun.* 46 (17 2010), pp. 2929–2931. DOI: `10.1039/B924547B`. URL: `http://dx.doi.org/10.1039/B924547B`.

[18] Jeffrey D. Rinehart and Jeffrey R. Long. “Exploiting single-ion anisotropy in the design of f-element single-molecule magnets”. In: *Chem. Sci.* 2 (11 2011), pp. 2078–2085. DOI: `10.1039/C1SC00513H`. URL: `http://dx.doi.org/10.1039/C1SC00513H`.

[19] Jun-Liang Liu et al. “Switching the anisotropy barrier of a single-ion magnet by symmetry change from quasi-D5h to quasi-Oh”. In: *Chem. Sci.* 4 (8 2013), pp. 3310–3316. DOI: `10.1039/C3SC50843A`. URL: `http://dx.doi.org/10.1039/C3SC50843A`.

[20] Toshio Miyamachi et al. “Stabilizing the magnetic moment of single holmium atoms by symmetry”. In: *Nature* 503 (7475 Nov. 2013), pp. 242 –246. DOI: `10.1038/nature12759`. URL: `http://dx.doi.org/10.1038/nature12759`.

[21] Bing-Wu Wang et al. “Evolvement of molecular nanomagnets in China”. In: *Philosophical Transactions of the Royal Society A: Mathematical, Physical and Engineering Sciences* 371.2000 (2013). DOI: `10.1098/rsta.2012.0316`. eprint: `http://rsta.royalsocietypublishing.org/content/371/2000/20120316.full.pdf+html`. URL: `http://rsta.royalsocietypublishing.org/content/371/2000/20120316.abstract`.

[22] Philipp Gütlich, Andreas Hauser, and Hartmut Spiering. “Thermal and Optical Switching of Iron(II) Complexes”. In: *Angewandte Chemie International Edition in English* 33.20 (1994), pp. 2024–2054. ISSN: 1521-3773. DOI: `10.1002/anie.199420241`. URL: `http://dx.doi.org/10.1002/anie.199420241`.

[23] Ruijuan Xiao et al. “Co Dimers on Hexagonal Carbon Rings Proposed as Subnanometer Magnetic Storage Bits”. In: *Phys. Rev. Lett.* 103 (18 2009), p. 187201. DOI: `10.1103/PhysRevLett.103.187201`. URL: `http://link.aps.org/doi/10.1103/PhysRevLett.103.187201`.

[24] Ruijuan Xiao et al. “Prediction of huge magnetic anisotropies of transition-metal dimer-benzene complexes from density functional theory calculations”. In: *Phys. Rev. B* 82 (20 2010), p. 205125. DOI: `10.1103/PhysRevB.82.205125`. URL: `http://link.aps.org/doi/10.1103/PhysRevB.82.205125`.

[25] Yuliang Mao Zhong, Jianmei Yuan, and Jianxin. "Density functional calculation of transition metal adatom adsorption on graphene". In: *Journal of Physics: Condensed Matter* 20.11 (2008), p. 115209. ISSN: 0953-8984. URL: `http://stacks.iop.org/0953-8984/20/i=11/a=115209`.

[26] Chao Cao et al. "Transition metal adatom and dimer adsorbed on graphene: Induced magnetization and electronic structures". In: *Phys. Rev. B* 81 (20 2010), p. 205424. DOI: `10.1103/PhysRevB.81.205424`. URL: `http://link.aps.org/doi/10.1103/PhysRevB.81.205424`.

[27] Mahdi Sargolzaei and Farideh Gudarzi. "Magnetic properties of single 3d transition metals adsorbed on graphene and benzene: A density functional theory study". In: *Journal of Applied Physics* 110.6 (2011). DOI: `http://dx.doi.org/10.1063/1.3636112`. URL: `http://scitation.aip.org/content/aip/journal/jap/110/6/10.1063/1.3636112`.

[28] V. Zólyomi et al. "First Principles Study of the Binding of 4d and 5d Transition Metals to Graphene". In: *The Journal of Physical Chemistry C* 114.43 (2010), pp. 18548–18552. DOI: `10.1021/jp107669b`. eprint: `http://pubs.acs.org/doi/pdf/10.1021/jp107669b`. URL: `http://pubs.acs.org/doi/abs/10.1021/jp107669b`.

[29] Hongbin Zhang et al. "Electrically Tunable Quantum Anomalous Hall Effect in Graphene Decorated by $5d$ Transition-Metal Adatoms". In: *Phys. Rev. Lett.* 108 (5 2012), p. 056802. DOI: `10.1103/PhysRevLett.108.056802`. URL: `http://link.aps.org/doi/10.1103/PhysRevLett.108.056802`.

[30] Piotr Błoński and Jürgen Hafner. "Pt on graphene monolayers supported on a Ni(111) substrate: Relativistic density-functional calculations". In: *The Journal of Chemical Physics* 136.7, 074701 (2012). DOI: `http://dx.doi.org/10.1063/1.3684891`. URL: `http://scitation.aip.org/content/aip/journal/jcp/136/7/10.1063/1.3684891`.

[31] Yudistira Virgus et al. "Ab initio many-body study of cobalt adatoms adsorbed on graphene". In: *Phys. Rev. B* 86 (24 Dec. 2012), p. 241406. DOI: `10.1103/PhysRevB.86.241406`. URL: `http://link.aps.org/doi/10.1103/PhysRevB.86.241406`.

[32] Richard M Martin. *Electronic Structure. Basic Theory and Practical Methods*. CAMBRIDGE UNIVERSITY PRESS, 2004. ISBN: 0-521-78285-6.

[33] Matthias Treier et al. "Surface-assisted cyclodehydrogenation provides a synthetic route towards easily processable and chemically tailored nanographenes". In: *Nat Chem* 3.1 (2011), pp. 61–67. ISSN: 1755-4330. DOI: `10.1038/nchem.891`. URL: `http://dx.doi.org/10.1038/nchem.891`.

[34] Annika Leifert et al. "Molecularly stabilised ultrasmall gold nanoparticles: synthesis, characterization and bioactivity". In: *Nanoscale* 5 (14 2013), pp. 6224–6242. DOI: `10.1039/C3NR00916E`. URL: `http://dx.doi.org/10.1039/C3NR00916E`.

[35] P. K. Jain et al. "Noble Metals on the Nanoscale: Optical and Photothermal Properties and Some Applications in Imaging, Sensing, Biology, And Medicine". In: *Acc. Chem. Res.* 41 (2008), p. 1578.

[36] X. Huang et al. "Plasmonic Photothermal Therapy (PPTT) Using Gold Nanoparticles". In: *Lasers Med. Sci* 23 (2008), p. 217.

[37] A. M. Gobin et al. "Near-Infrared Resonant Nanoshells for Combined Optical Imaging and Photothermal Cancer Therapy". In: *Nano Lett.* 7 (2007), p. 1929.

[38] L. Tong et al. “Gold Nanorods as Contrast Agents for Biological Imaging: Optical Properties, Surface Conjugation and Photothermal Effects”. In: *Photochem. Photobiol.* 85 (2009), p. 21.

[39] Sudipa Panigrahi et al. “Synthesis and Size-Selective Catalysis by Supported Gold Nanoparticles: Study on Heterogeneous and Homogeneous Catalytic Process”. In: *The Journal of Physical Chemistry C* 111.12 (2007), pp. 4596–4605. DOI: `10.1021/jp067554u`. eprint: `http://dx.doi.org/10.1021/jp067554u`. URL: `http://dx.doi.org/10.1021/jp067554u`.

[40] M. Valden, X. Lai, and D. W. Goodman. “Onset of Catalytic Activity of Gold Clusters on Titania with the Appearance of Nonmetallic Properties”. In: *Science* 281.5383 (1998), pp. 1647–1650. DOI: `10.1126/science.281.5383.1647`. eprint: `http://www.sciencemag.org/content/281/5383/1647.full.pdf`. URL: `http://www.sciencemag.org/content/281/5383/1647.abstract`.

[41] Debra R. Rolison. “Catalytic Nanoarchitectures–the Importance of Nothing and the Unimportance of Periodicity”. In: *Science* 299.5613 (2003), pp. 1698–1701. DOI: `10.1126/science.1082332`. eprint: `http://www.sciencemag.org/content/299/5613/1698.full.pdf`. URL: `http://www.sciencemag.org/content/299/5613/1698.abstract`.

[42] Kamat P. V. “Photophysical, Photochemical, and Photocatalytic Aspects of Metal Nanoparticles”. In: *J. Phys. Chem. B* 106 (2002), p. 7729.

[43] Gao Li and Rongchao Jin. “Atomically Precise Gold Nanoclusters as New Model Catalysts”. In: *Accounts of Chemical Research* 46.8 (2013). PMID 23534692, pp. 1749–1758. DOI: `10.1021/ar300213z`. URL: `http://dx.doi.org/10.1021/ar300213z`.

[44] L. R Hirsch et al. “Nanoshell-Mediated Near-Infrared Thermal Therapy of Tumors under Magnetic Resonance Guidance”. In: *Proc. Natl. Acad. Sci. U.S.A.* 100 (2003), p. 13549.

[45] Zhang J. Z. “Biomedical Applications of Shape-Controlled Plasmonic Nanostructures: A Case Study of Hollow Gold Nanospheres for Photothermal Ablation Therapy of Cancer”. In: *J. Phys. Chem. Lett.* 1 (2010), p. 686.

[46] J. Z. Zhang et al. “Comment on "Gold Nanoshells Improve Single Nanoparticle Molecular Sensors"”. In: *Nano Lett.* 5 (2005), p. 809.

[47] A. M. Schwartzberg and J. Z. Zhang. “Novel Optical Properties and Emerging Applications of Metal Nanostructures”. In: *J. Phys. Chem. C* 112 (2008), p. 10323.

[48] Günter Schmid et al. “Synthesis and electron microscopic investigation of controlled growth, ligand-stabilized gold colloids and theoretical considerations on the covering of surfaces by colloids”. In: *Zeitschrift für Naturforschung B* 45 (1990), pp. 989–994. ISSN: 0932-0776.

[49] Günter Schmid. *Nanoparticles: From Theory to Application*. Viley-VCH, 2004. ISBN: 3-527-30507-6.

[50] Michael Walter et al. “A unified view of ligand-protected gold clusters as superatom complexes”. In: *Proceedings of the National Academy of Sciences* 105.27 (2008), pp. 9157–9162. DOI: `10.1073/pnas.0801001105`. eprint: `http://www.pnas.org/content/105/27/9157.full.pdf+html`. URL: `http://www.pnas.org/content/105/27/9157.abstract`.

[51] Hannu Häkkinen. “Atomic and electronic structure of gold clusters: understanding flakes, cages and superatoms from simple concepts”. In: *Chem. Soc. Rev.* 37 (9 2008), pp. 1847–1859. DOI: `10.1039/B717686B`. URL: `http://dx.doi.org/10.1039/B717686B`.

[52] Abdallah F. Zedan et al. “Ultrasmall Gold Nanoparticles Anchored to Graphene and Enhanced Photothermal Effects by Laser Irradiation of Gold Nanostructures in Graphene Oxide Solutions”. In: *ACS Nano* 7.1 (2013). PMID: 23194145, pp. 627–636. DOI: `10.1021/nn304775h`. eprint: `http://dx.doi.org/10.1021/nn304775h`. URL: `http://dx.doi.org/10.1021/nn304775h`.

[53] Na Li, Pengxiang Zhao, and Didier Astruc. “Anisotropic Gold Nanoparticles: Synthesis, Properties, Applications, and Toxicity”. In: *Angewandte Chemie International Edition* 53.7 (2014), pp. 1756–1789. ISSN: 1521-3773. DOI: `10.1002/anie.201300441`. URL: `http://dx.doi.org/10.1002/anie.201300441`.

[54] Wei Kangliang et al. “Simulation of carrier transport in heterostructures using the 2D self-consistent full-band ensemble Monte Carlo method”. In: *Journal of Semiconductors* 31.8 (2010), p. 084004. URL: `http://stacks.iop.org/1674-4926/31/i=8/a=084004`.

[55] Laurence W. Nagel and D.O. Pederson. *SPICE (Simulation Program with Integrated Circuit Emphasis)*. Tech. rep. UCB/ERL M382. EECS Department, University of California, Berkeley, Apr. 1973. URL: `http://www.eecs.berkeley.edu/Pubs/TechRpts/1973/22871.html`.

[56] Leif Arkeryd. “On the Boltzmann equation”. English. In: *Archive for Rational Mechanics and Analysis* 45.1 (1972), pp. 1–16. ISSN: 0003-9527. DOI: `10.1007/BF00253392`. URL: `http://dx.doi.org/10.1007/BF00253392`.

[57] *Elmer software package*. URL: `http://research.csc.fi/web/elmer`.

[58] Osamu Sato. “Photoinduced magnetization in molecular compounds”. In: *Journal of Photochemistry and Photobiology C: Photochemistry Reviews* 5.3 (2004), pp. 203 –223. ISSN: 1389-5567. DOI: `http://dx.doi.org/10.1016/j.jphotochemrev.2004.10.001`. URL: `http://www.sciencedirect.com/science/article/pii/S1389556704000371`.

[59] N. Domingo et al. “Magnetism of isolated Mn_{12} single-molecule magnets detected by magnetic circular dichroism: Observation of spin tunneling with a magneto-optical technique”. In: *Phys. Rev. B* 69 (5 Feb. 2004), p. 052405. DOI: `10.1103/PhysRevB.69.052405`. URL: `http://link.aps.org/doi/10.1103/PhysRevB.69.052405`.

[60] Veacheslav Vieru, Liviu Ungur, and Liviu F. Chibotaru. “Key Role of Frustration in Suppression of Magnetization Blocking in Single-Molecule Magnets”. In: *The Journal of Physical Chemistry Letters* 4.21 (2013), pp. 3565–3569. DOI: `10.1021/jz4017206`. eprint: `http://dx.doi.org/10.1021/jz4017206`. URL: `http://dx.doi.org/10.1021/jz4017206`.

[61] Toshio Miyamachi et al. “Robust spin crossover and memristance across a single molecule”. In: *Nat Commun* 3 (July 2012), p. 938. DOI: `10.1038/ncomms1940`. URL: `http://dx.doi.org/10.1038/ncomms1940`.

[62] E. Freysz et al. “Single laser pulse induces spin state transition within the hysteresis loop of an Iron compound”. In: *Chemical Physics Letters* 394.4–6 (2004), pp. 318 –323. ISSN: 0009-2614. DOI: `http://dx.doi.org/10.1016/j.cplett.2004.07.017`. URL: `http://www.sciencedirect.com/science/article/pii/S0009261404010504`.

[63] V. Meded et al. “Electrical control over the Fe(II) spin crossover in a single molecule: Theory and experiment”. In: *Phys. Rev. B* 83 (24 June 2011), p. 245415. DOI: `10.1103/PhysRevB.83.245415`. URL: `http://link.aps.org/doi/10.1103/PhysRevB.83.245415`.

[64] Abhudaya Mishra et al. “The search for 3d-4f single-molecule magnets: synthesis, structure and magnetic properties of a [MnIII2DyIII2] cluster”. In: *Chem. Commun.* (16 2005), pp. 2086–2088. DOI: `10.1039/B501508A`. URL: `http://dx.doi.org/10.1039/B501508A`.

[65] Guillem Aromí and EuanK. Brechin. “Synthesis of 3d Metallic Single-Molecule Magnets”. English. In: *Single-Molecule Magnets and Related Phenomena*. Ed. by Richard Winpenny. Vol. 122. Structure and Bonding. Springer Berlin Heidelberg, 2006, pp. 1–67. ISBN: 978-3-540-33239-8. DOI: `10.1007/430_022`. URL: `http://dx.doi.org/10.1007/430_022`.

[66] A. K. Geim and K. S. Novoselov. “The Rise of Graphene”. In: *Nat Mater* 6.3 (2007), pp. 183–191. ISSN: 1476-1122. DOI: `10.1038/nmat1849`. URL: `http://dx.doi.org/10.1038/nmat1849`.

[67] K S Novoselov et al. “Electric Field Effect in Atomically Thin Carbon Films”. In: *Science* 306.5696 (2004), pp. 666–669. DOI: `10.1126/science.1102896`.

[68] Alberto Bianco et al. “All in the graphene family a recommended nomenclature for two-dimensional carbon materials”. In: *Carbon* 65.0 (2013), pp. 1 –6. ISSN: 0008-6223. DOI: `http://dx.doi.org/10.1016/j.carbon.2013.08.038`. URL: `http://www.sciencedirect.com/science/article/pii/S0008622313008002`.

[69] A. H. Castro Neto et al. “The electronic properties of graphene”. In: *Rev. Mod. Phys.* 81 (1 Jan. 2009), pp. 109–162. DOI: `10.1103/RevModPhys.81.109`. URL: `http://link.aps.org/doi/10.1103/RevModPhys.81.109`.

[70] Ovidiu Cretu et al. “Migration and Localization of Metal Atoms on Strained Graphene”. In: *Phys. Rev. Lett.* 105 (19 2010), p. 196102. DOI: `10.1103/PhysRevLett.105.196102`. URL: `http://link.aps.org/doi/10.1103/PhysRevLett.105.196102`.

[71] Attila Szabo. *Modern Quantum Chemistry*. Dover Publications Inc., 1996. ISBN: 0486691861.

[72] Wolfram Koch and Max C. Holthausen. *A Chemist’s Guide to Density Functional Theory*. Wiley-VCH, 2001. ISBN: 978-3-527-30372-4.

[73] W. Kohn and L. J. Sham. “Self-Consistent Equations Including Exchange and Correlation Effects”. In: *Phys. Rev.* 140 (4A 1965), A1133–A1138. DOI: `10.1103/PhysRev.140.A1133`. URL: `http://link.aps.org/doi/10.1103/PhysRev.140.A1133`.

[74] P. Hohenberg and W. Kohn. “Inhomogeneous Electron Gas”. In: *Phys. Rev.* 136 (3B 1964), B864–B871. DOI: `10.1103/PhysRev.136.B864`. URL: `http://link.aps.org/doi/10.1103/PhysRev.136.B864`.

[75] John P. Perdew and Yue Wang. “Accurate and simple analytic representation of the electron-gas correlation energy”. In: *Phys. Rev. B* 45 (23 1992), pp. 13244–13249. DOI: `10.1103/PhysRevB.45.13244`. URL: `http://link.aps.org/doi/10.1103/PhysRevB.45.13244`.

[76] A. D. Becke. “Density-functional exchange-energy approximation with correct asymptotic behavior”. In: *Phys. Rev. A* 38 (6 1988), pp. 3098–3100. DOI: `10.1103/PhysRevA.38.3098`. URL: `http://link.aps.org/doi/10.1103/PhysRevA.38.3098`.

[77] John P. Perdew. “Density-functional approximation for the correlation energy of the inhomogeneous electron gas”. In: *Phys. Rev. B* 33 (12 1986), pp. 8822–8824. DOI: `10.1103/PhysRevB.33.8822`. URL: `http://link.aps.org/doi/10.1103/PhysRevB.33.8822`.

[78] Chengteh Lee, Weitao Yang, and Robert G. Parr. “Development of the Colle-Salvetti correlation-energy formula into a functional of the electron density”. In: *Phys. Rev. B* 37 (2 1988), pp. 785–789. DOI: `10.1103/PhysRevB.37.785`. URL: `http://link.aps.org/doi/10.1103/PhysRevB.37.785`.

[79] O. Gunnarsson and B. I. Lundqvist. “Exchange and correlation in atoms, molecules, and solids by the spin-density-functional formalism”. In: *Phys. Rev. B* 13 (10 May 1976), pp. 4274–4298. DOI: `10.1103/PhysRevB.13.4274`. URL: `http://link.aps.org/doi/10.1103/PhysRevB.13.4274`.

[80] Chengteh Lee, Weitao Yang, and Robert G. Parr. “Development of the Colle-Salvetti correlation-energy formula into a functional of the electron density”. In: *Phys. Rev. B* 37 (2 1988), pp. 785–789. DOI: `10.1103/PhysRevB.37.785`. URL: `http://link.aps.org/doi/10.1103/PhysRevB.37.785`.

[81] S. H. Vosko, L. Wilk, and M. Nusair. “Accurate spin-dependent electron liquid correlation energies for local spin density calculations: a critical analysis”. In: *Canadian Journal of Physics* 58.8 (1980), pp. 1200–1211. DOI: `10.1139/p80-159`. eprint: `http://dx.doi.org/10.1139/p80-159`. URL: `http://dx.doi.org/10.1139/p80-159`.

[82] *TURBOMOLE V6.6 2014, a development of University of Karlsruhe and Forschungszentrum Karlsruhe GmbH, 1989-2007, TURBOMOLE GmbH, since 2007; available from* `http://www.turbomole.com`. Filipp Furche et al. “Turbomole”. In: *Wiley Interdisciplinary Reviews: Computational Molecular Science* 4.2 (2014), pp. 91–100. ISSN: 1759-0884. DOI: `10.1002/wcms.1162`. URL: `http://dx.doi.org/10.1002/wcms.1162`.

[83] *TURBOMOLE V6.6 2014, a development of University of Karlsruhe and Forschungszentrum Karlsruhe GmbH, 1989-2007, TURBOMOLE GmbH, since 2007; available from* `http://www.turbomole.com`.

[84] Filipp Furche et al. “Turbomole”. In: *Wiley Interdisciplinary Reviews: Computational Molecular Science* 4.2 (2014), pp. 91–100. ISSN: 1759-0884. DOI: `10.1002/wcms.1162`. URL: `http://dx.doi.org/10.1002/wcms.1162`.

[85] Roald Hoffmann. “An Extended Hückel Theory. I. Hydrocarbons”. In: *The Journal of Chemical Physics* 39.6 (1963), pp. 1397–1412. DOI: `http://dx.doi.org/10.1063/1.1734456`. URL: `http://scitation.aip.org/content/aip/journal/jcp/39/6/10.1063/1.1734456`.

[86] Stefan Grimme. “Accurate description of van der Waals complexes by density functional theory including empirical corrections”. In: *Journal of Computational Chemistry* 25.12 (2004), pp. 1463–1473. ISSN: 1096-987X. DOI: `10.1002/jcc.20078`. URL: `http://dx.doi.org/10.1002/jcc.20078`.

[87] Qin Wu and Weitao Yang. “Empirical correction to density functional theory for van der Waals interactions”. In: *The Journal of Chemical Physics* 116.2 (2002), pp. 515–524. DOI: `http://dx.doi.org/10.1063/1.1424928`. URL: `http://scitation.aip.org/content/aip/journal/jcp/116/2/10.1063/1.1424928`.

[88] Stefan Grimme. “Semiempirical GGA-type density functional constructed with a long-range dispersion correction”. In: *Journal of Computational Chemistry* 27.15 (2006), pp. 1787–1799. ISSN: 1096-987X. DOI: `10.1002/jcc.20495`. URL: `http://dx.doi.org/10.1002/jcc.20495`.

[89] A. L. Barra et al. “Single-Molecule Magnet Behavior of a Tetranuclear Iron(III) Complex. The Origin of Slow Magnetic Relaxation in Iron(III) Clusters”. In: *Journal of the American Chemical Society* 121.22 (1999), pp. 5302–5310. DOI: `10.1021/ja9818755`. eprint: `http://dx.doi.org/10.1021/ja9818755`. URL: `http://dx.doi.org/10.1021/ja9818755`.

[90] Mihail Atanasov et al. “A theoretical analysis of chemical bonding, vibronic coupling, and magnetic anisotropy in linear iron(ii) complexes with single-molecule magnet behavior”. In: *Chem. Sci.* 4 (1 2013), pp. 139–156. DOI: `10.1039/C2SC21394J`. URL: `http://dx.doi.org/10.1039/C2SC21394J`.

[91] Athanassios K. Boudalis et al. “A Nonanuclear Iron(II) Single-Molecule Magnet”. In: *Angewandte Chemie* 116.17 (2004), pp. 2316–2320. ISSN: 1521-3757. DOI: `10.1002/ange.200353147`. URL: `http://dx.doi.org/10.1002/ange.200353147`.

[92] Cristiano Benelli et al. “A Decanuclear Iron(III) Single Molecule Magnet: Use of Monte Carlo Methodology To Model the Magnetic Properties”. In: *Inorganic Chemistry* 40.2 (2001). PMID: 11170519, pp. 188–189. DOI: `10.1021/ic000840e`. eprint: `http://dx.doi.org/10.1021/ic000840e`. URL: `http://dx.doi.org/10.1021/ic000840e`.

[93] Dante Gatteschi, Roberta Sessoli, and Andrea Cornia. “Single-molecule magnets based on iron(iii) oxo clusters”. In: *Chem. Commun.* (9 2000), pp. 725–732. DOI: `10.1039/A908254I`. URL: `http://dx.doi.org/10.1039/A908254I`.

[94] W. A. Baker and H. M. Bobonich. “Magnetic Properties of Some High-Spin Complexes of Iron(II)”. In: *Inorganic Chemistry* 3.8 (1964), pp. 1184–1188. DOI: `10.1021/ic50018a027`. eprint: `http://dx.doi.org/10.1021/ic50018a027`. URL: `http://dx.doi.org/10.1021/ic50018a027`.

[95] Daniel Aravena and Eliseo Ruiz. “Coherent Transport through Spin-Crossover Single Molecules”. In: *Journal of the American Chemical Society* 134.2 (2012). PMID: 22206584, pp. 777–779. DOI: `10.1021/ja2090096`. eprint: `http://dx.doi.org/10.1021/ja2090096`. URL: `http://dx.doi.org/10.1021/ja2090096`.

[96] Thiruvancheril G. Gopakumar et al. “Electron-Induced Spin Crossover of Single Molecules in a Bilayer on Gold”. In: *Angewandte Chemie International Edition* 51.25 (2012), pp. 6262–6266. ISSN: 1521-3773. DOI: `10.1002/anie.201201203`. URL: `http://dx.doi.org/10.1002/anie.201201203`.

[97] Corine Mathonière et al. “Photoinduced Single-Molecule Magnet Properties in a Four-Coordinate Iron(II) Spin Crossover Complex”. In: *Journal of the American Chemical Society* 135.51 (2013). PMID: 24313622, pp. 19083–19086. DOI: `10.1021/ja410643s`. eprint: `http://dx.doi.org/10.1021/ja410643s`. URL: `http://dx.doi.org/10.1021/ja410643s`.

[98] Wei L. Wang, Sheng Meng, and Efthimios Kaxiras. “Graphene NanoFlakes with Large Spin”. In: *Nano Letters* 8.1 (2008). PMID: 18052302, pp. 241–245. DOI: `10.1021/nl072548a`. eprint: `http://dx.doi.org/10.1021/nl072548a`. URL: `http://dx.doi.org/10.1021/nl072548a`.

[99] P. A. M. Dirac. “Quantum Mechanics of Many-Electron Systems”. In: *Proceedings of the Royal Society of London. Series A* 123.792 (1929), pp. 714–733. DOI: `10.1098/rspa.1929.0094`. eprint: `http://rspa.royalsocietypublishing.org/content/123/792/714.full.pdf+html`. URL: `http://rspa.royalsocietypublishing.org/content/123/792/714.short`.

[100] J. C. Slater. “A Simplification of the Hartree-Fock Method”. In: *Phys. Rev.* 81 (3 1951), pp. 385–390. DOI: `10.1103/PhysRev.81.385`. URL: `http://link.aps.org/doi/10.1103/PhysRev.81.385`.

[101] Elliott H. Lieb. “Two theorems on the Hubbard model”. In: *Phys. Rev. Lett.* 62 (10 1989), pp. 1201–1204. DOI: `10.1103/PhysRevLett.62.1201`. URL: `http://link.aps.org/doi/10.1103/PhysRevLett.62.1201`.

[102] A. V. Krasheninnikov et al. “Embedding Transition-Metal Atoms in Graphene: Structure, Bonding, and Magnetism”. In: *Phys. Rev. Lett.* 102 (12 Mar. 2009), p. 126807. DOI: `10.1103/PhysRevLett.102.126807`. URL: `http://link.aps.org/doi/10.1103/PhysRevLett.102.126807`.

[103] A.V. Krasheninnikov and R.M. Nieminen. “Attractive interaction between transition-metal atom impurities and vacancies in graphene: a first-principles study”. English. In: *Theoretical Chemistry Accounts* 129.3-5 (2011), pp. 625–630. ISSN: 1432-881X. DOI: `10.1007/s00214-011-0910-3`. URL: `http://dx.doi.org/10.1007/s00214-011-0910-3`.

[104] G. Kresse and J. Hafner. “Ab initio”. In: *Phys. Rev. B* 47 (1 Jan. 1993), pp. 558–561. DOI: `10.1103/PhysRevB.47.558`. URL: `http://link.aps.org/doi/10.1103/PhysRevB.47.558`.

[105] G. Kresse and J. Hafner. “Ab initio”. In: *Phys. Rev. B* 49 (20 May 1994), pp. 14251–14269. DOI: `10.1103/PhysRevB.49.14251`. URL: `http://link.aps.org/doi/10.1103/PhysRevB.49.14251`.

[106] G. Kresse and J. Furthmüller. “Efficiency of ab-initio total energy calculations for metals and semiconductors using a plane-wave basis set”. In: *Computational Materials Science* 6.1 (1996), pp. 15 –50. ISSN: 0927-0256. DOI: `http://dx.doi.org/10.1016/0927-0256(96)00008-0`. URL: `http://www.sciencedirect.com/science/article/pii/0927025696000080`.

[107] G. Kresse and J. Furthmüller. “Efficient iterative schemes for ab initio total-energy calculations using a plane-wave basis set”. In: *Phys. Rev. B* 54 (16 Oct. 1996), pp. 11169–11186. DOI: `10.1103/PhysRevB.54.11169`. URL: `http://link.aps.org/doi/10.1103/PhysRevB.54.11169`.

[108] John P. Perdew, Kieron Burke, and Matthias Ernzerhof. “Generalized Gradient Approximation Made Simple”. In: *Phys. Rev. Lett.* 77 (18 1996), pp. 3865–3868. DOI: `10.1103/PhysRevLett.77.3865`. URL: `http://link.aps.org/doi/10.1103/PhysRevLett.77.3865`.

[109] Markus K. Armbruster, Wim Klopper, and Florian Weigend. “Basis-set extensions for two-component spin-orbit treatments of heavy elements”. In: *Phys. Chem. Chem. Phys.* 8 (42 2006), pp. 4862–4865. DOI: `10.1039/B610211E`. URL: `http://dx.doi.org/10.1039/B610211E`.

[110] Ansgar Schäfer, Hans Horn, and Reinhart Ahlrichs. “Fully optimized contracted Gaussian basis sets for atoms Li to Kr”. In: *The Journal of Chemical Physics* 97.4 (1992), pp. 2571–2577. DOI: `http://dx.doi.org/10.1063/1.463096`. URL: `http://scitation.aip.org/content/aip/journal/jcp/97/4/10.1063/1.463096`.

[111] Florian Weigend and Reinhart Ahlrichs. “Balanced basis sets of split valence, triple zeta valence and quadruple zeta valence quality for H to Rn: Design and assessment of accuracy”. In: *Phys. Chem. Chem. Phys.* 7 (18 2005), pp. 3297–3305. DOI: `10.1039/B508541A`. URL: `http://dx.doi.org/10.1039/B508541A`.

[112] Florian Weigend et al. “RI-MP2: optimized auxiliary basis sets and demonstration of efficiency”. In: *Chemical Physics Letters* 294.1–3 (1998), pp. 143 –152. ISSN: 0009-2614. DOI: `http://dx.doi.org/10.1016/S0009-2614(98)00862-8`. URL: `http://www.sciencedirect.com/science/article/pii/S0009261498008628`.

[113] Dmitrij Rappoport and Filipp Furche. “Property-optimized Gaussian basis sets for molecular response calculations”. In: *The Journal of Chemical Physics* 133.13, 134105 (2010), pp. –. DOI: `http://dx.doi.org/10.1063/1.3484283`. URL: `http://scitation.aip.org/content/aip/journal/jcp/133/13/10.1063/1.3484283`.

[114] Stefan Grimme et al. “A consistent and accurate ab initio parametrization of density functional dispersion correction (DFT-D) for the 94 elements H-Pu”. In: *The Journal of Chemical Physics* 132.15, 154104 (2010), pp. –. DOI: `http://dx.doi.org/10.1063/1.3382344`. URL: `http://scitation.aip.org/content/aip/journal/jcp/132/15/10.1063/1.3382344`.

[115] Chr. Møller and M. S. Plesset. “Note on an Approximation Treatment for Many-Electron Systems”. In: *Phys. Rev.* 46 (7 Oct. 1934), pp. 618–622. DOI: `10.1103/PhysRev.46.618`. URL: `http://link.aps.org/doi/10.1103/PhysRev.46.618`.

[116] Jianmin Tao et al. “Climbing the Density Functional Ladder: Nonempirical Meta-Generalized Gradient Approximation Designed for Molecules and Solids”. In: *Phys. Rev. Lett.* 91 (14 2003), p. 146401. DOI: `10.1103/PhysRevLett.91.146401`. URL: `http://link.aps.org/doi/10.1103/PhysRevLett.91.146401`.

[117] Axel D. Becke. “Density-functional thermochemistry. III. The role of exact exchange”. In: *The Journal of Chemical Physics* 98.7 (1993), pp. 5648–5652. DOI: `http://dx.doi.org/10.1063/1.464913`. URL: `http://scitation.aip.org/content/aip/journal/jcp/98/7/10.1063/1.464913`.

[118] Daniel Huang et al. “Plastic-Compatible Low Resistance Printable Gold Nanoparticle Conductors for Flexible Electronics”. In: *Journal of The Electrochemical Society* 150.7 (2003), G412–G417. DOI: `10.1149/1.1582466`. eprint: `http://jes.ecsdl.org/content/150/7/G412.full.pdf+html`. URL: `http://jes.ecsdl.org/content/150/7/G412.abstract`.

[119] Michael Walter et al. “Electronic Structure of MgO-Supported Au Clusters: Quantum Dots Probed by Scanning Tunneling Microscopy”. In: *Phys. Rev. Lett.* 99 (9 Aug. 2007), p. 096102. DOI: `10.1103/PhysRevLett.99.096102`. URL: `http://link.aps.org/doi/10.1103/PhysRevLett.99.096102`.

[120] Kenichi Fukui, Teijiro Yonezawa, and Haruo Shingu. “A Molecular Orbital Theory of Reactivity in Aromatic Hydrocarbons”. In: *The Journal of Chemical Physics* 20.4 (1952).

[121] J. C. Slonczewski and P. R. Weiss. “Band Structure of Graphite”. In: *Phys. Rev.* 109 (2 Jan. 1958), pp. 272–279. DOI: `10.1103/PhysRev.109.272`. URL: `http://link.aps.org/doi/10.1103/PhysRev.109.272`.

[122] D W Boukhvalov and M I Katsnelson. “Chemical functionalization of graphene”. In: *Journal of Physics: Condensed Matter* 21.34 (2009), p. 344205. URL: `http://stacks.iop.org/0953-8984/21/i=34/a=344205`.

[123] Luc Devroye. *Non-Uniform Random Variate Generation*. Springer-Verlag, 1986. ISBN: 3-540-96305-7.

[124] C. L. R. Milazzo. “Finite difference scheme for semiconductor Boltzmann equation with nonlinear collision operator”. In: *Appl. Math. Sci.* 7 (15), pp. 735–750.

[125] Vincenza Di Stefano. “Free-Flight Time Generation in Direct Simulation Monte Carlo for Carrier Transport in Semiconductors”. In: *Communications to SIMAI Congress* 3 (2009), p. 223. DOI: `10.1685/CSC09223`.

[126] Eduardo Castro et al. “Limits on Charge Carrier Mobility in Suspended Graphene due to Flexural Phonons”. In: *Phys. Rev. Lett.* 105 (26 Dec. 2010), p. 266601. DOI: `10.1103/PhysRevLett.105.266601`. URL: `http://link.aps.org/doi/10.1103/PhysRevLett.105.266601`.

[127] S. Das Sarma et al. “Electronic transport in two-dimensional graphene”. In: *Rev. Mod. Phys.* 83 (2 May 2011), pp. 407–470. DOI: `10.1103/RevModPhys.83.407`. URL: `http://link.aps.org/doi/10.1103/RevModPhys.83.407`.